Early age cycling in the grout connection of an offshore wind jacket structure

Lukas Boogaart

TU Delft NTNU Boskalis

Early age cycling in the grout connection of an offshore wind jacket structure

by

Lukas Boogaart

in partial fulfilment of the requirements for the degree of

Master of Science

in 'Offshore and Dredging Engineering' at the Delft University of Technology

and in 'Technology-Wind Energy' at the Norwegian University of Science and Technology

to be defended on Friday the 3th of July 2020 at 10:00 AM.

Student number:	4291476 (TU Delft) / 517529 (NTNU)	
University supervisors:	Prof. dr. A.V. Metrikine,	TU Delft (chairman)
	Prof. dr. Z. Gao,	NTNU
	Ir. P. van der Male,	TU Delft
	Ir. M. Vergassola,	TU Delft
Company supervisors:	Ir. W. Luites,	Boskalis
	Ir. M. van der Veen,	Boskalis

Preface

This report is part of my master thesis, which is the final deliverable in order to obtain a degree in Offshore and Dredging Engineering at the Delft University of Technology (TU Delft) and Technology-Wind Energy at the Norwegian University of Science and Technology (NTNU).

For this research, I would like to thank a number of people. First of all, the chair of my study Frank Sliggers. I really appreciate how you continued to supervise me even though your formal obligation to the TU Delft was finished. It was interesting and helpful to obtain good feedback from you as an experienced teacher in the field of offshore. Furthermore, I would like to thank Pim van der Male and Marco Vergassola for their help as daily supervisors. The bi-weekly meetings with one or both of you gave me the guidance I needed to steer this study in the right direction. I thank you for the time you put into this.

From Boskalis Offshore Energy, I would first of all like to thank Wout Luites. Wout, as my direct supervisor your help was essential for this study. You have been patient with all the questions I had in the beginning and helped me where needed. You furthermore provided me with all the data I needed, for a number of times. I enjoyed our weekly meetings. Especially when we were forced to work from home. Furthermore, I would like to thank the whole design time for their help with a special thanks to Maarten van der Veen for his support. It was a pity I could not enjoy working at the office longer.

From the NTNU, I would like to thank Zhen Gao for his guidance. You have been supporting me during my literature research in Trondheim and I appreciate how you continued this commitment during my thesis in the Netherlands.

I would like to thank my fellow EWEM students for the great time abroad and the amazing trips we made. At last, I would like to thank my family, Nine, my roommates and everyone that has supported me throughout these years. I hope to talk to you all soon and celebrate this significant milestone!

Lukas Boogaart
Rotterdam, June 2020

Abstract

The yearly installed percentage of offshore wind jacket substructures is rising. The most common installation method for a jacket structure nowadays starts by driving the foundation piles in the seabed through a pre-piling template. The jacket is then lowered on top until the legs are resting on the foundation piles through friction-based stopper connections. In order to rigidly fix the connection, grout is pumped into the annulus between the pile and leg. During the curing period of grout, generally taken as 24 hours, environmental loads cause the jacket to oscillate in various directions. As a result, the jacket leg will move relative to the foundation pile. This movement, which is called Early Age Cycling (EAC), can cause crack formation in the cured grout therefore decreasing the shear capacity of the connection. The *DNV GL* has restricted this relative movement to a conservative 1 mm within the first 24 hours due to a research gap on the subject. The strict regulation forces companies to use expensive EAC mitigation concepts of which the real effects are a debated issue.

The objective of this research is to gain insight into the modelling approach and the magnitude of EAC movements and investigate how they can most efficiently be minimized. This is achieved by investigating three phases: 1) simulating a number of load cases on a global jacket model and extracting interface forces near the seabed, 2) using these interface forces to assess the EAC movement on a detailed pile-leg reference model with a full circular stopper 3) analysing this reference stopper by testing three modified configurations. These configurations are designed with respectively two, three and four brackets yielding the same contact area. A sensitivity study is then performed by increasing the contact area.

The largest EAC movement within all models can be measured at the tip of the jacket leg. The location of this movement on the circumference of the leg varies based on the loading condition and stopper model. In general simulations on the reference model showed EAC movements below 1 mm due to a uniform stress distribution from the stopper to the foundation pile. For larger wave loads, sliding occurred resulting in large EAC movements. The initial modified configurations show significantly larger EAC movement when compared to the reference stopper. In general, the EAC movement decrease when the number of brackets increases. This is the result of a more even stress distribution around the circumference of the pile. A phenomenon visible for the two bracket stopper is rotation around the axis of the wave direction resulting in large EAC movement. This effect, denoted as moment induced rotations, should be limited by all means. A sensitivity analysis on friction showed that sliding could most efficiently be solved by increasing the friction coefficient. This is highly recommended since it greatly improves the performance of the stopper connection for larger waves.

This research could be further extended by performing a large sensitivity study to normalize the current results. This would be needed to verify whether the current conclusions can also be adopted for general use.

Contents

List of Tables

List of Figures

Nomenclature

Latin symbol	Description	Unit
A	Cross sectional member area	[m^2]
C	Shape coefficient	[-]
C_D	Drag coefficient	[-]
C_M	Inertia coefficient	[-]
D	Jacket member diameter	[m]
EI_f	Equivalent bending stiffness	[Nm^2]
Q	Seabed shear force	[N]
f_L	Lift force per area	[N/m^2]
f_N	Normal force per area	[N/m^2]
f_T	Tangential force per area	[N/m^2]
F_W	Wind Force	[N]
H_{max}	Maximum design wave height	[m]
H_s	Significant wave height	[m]
I	Turbulence intensity	[-]
J	Soil constant	[-]
k	Surface roughness	[-]
K_c	Keulegan-Carpenter number	[-]
l_f	Equivalent fixity length	[m]
l_t	Turbulence length scale	[m]
M	Seabed moment	[Nm]
p	lateral soil resistance	[kN/m]
P	Axial pile force	[N]
q	Basic wind pressure	[N/m^2]
Re	Reynolds number	[-]
s_u	Undrained shear strength	[kN/m^2]
S	Projected area wind load	[m^2]
T_{POP}	Planned operational period	[hr]
T_{ass}	Design wave period	[s]
T_C	Contingency time	[hr]
T_{high}	High wave period	[s]
T_{low}	Low wave period	[s]
T_p	Peak period	[s]
T_R	Operational reference period	[hr]
T_z	Zero up-crossing period	[s]
U_{10}	2 hour windspeed at 10 m	[m/s]
$U_{T,z}$	Average wind velocity	[m/s]
v_N	Normal particle velocity	[m/s]
$\dot{v_N}$	Normal particle accelerations	[m/s^2]
w	Seabed defection	[m]
y	Lateral pile deflection	[-]
z_0	Roughness parameter	[-]

Greek symbol	Description	Unit
α	Angle of attack	[^{o}]
γ	Peak enhancement factor	[-]
γ'	Submerged unit weight soil	[kN/m^3]
ϵ_{50}	Strain at half max. stress	[-]
λ	Wave length	[m]
μ_d	Dynamic friction coefficient	[-]
μ_s	Static friction coefficient	[-]
ρ	Density	[kg/m^3]
ϕ	Seabed rotations	[^{o}]
ω_n	Natural frequency	[Hz]

Abbreviation	Description
AF	Apparent Fixity
CapEx	Capital Expenditure
EAC	Early Age Cycling
FE	Finite Element
FLS	Fatigue Limit State
LAT	Lowest Astronomical Tide
LCOE	Levelized Cost Of Energy
MP	Monopile
OWE	Offshore Wind Energy
OWF	Offshore Wind Farm
ROV	Remotely Operated Vehicle
TP	Transition Piece
ULS	Ultimate Limit State
WTG	Wind Turbine Generator

Terminology

Within this report, a number of terms will be used to indicate movement and deflection within the pile-leg model. For clarity, this terminology will be consistent with the expressions as indicated in Figure 1 and as based on *DNVGL-ST-0126* [17]. Within this figure, arrows indicate movement/deflection.

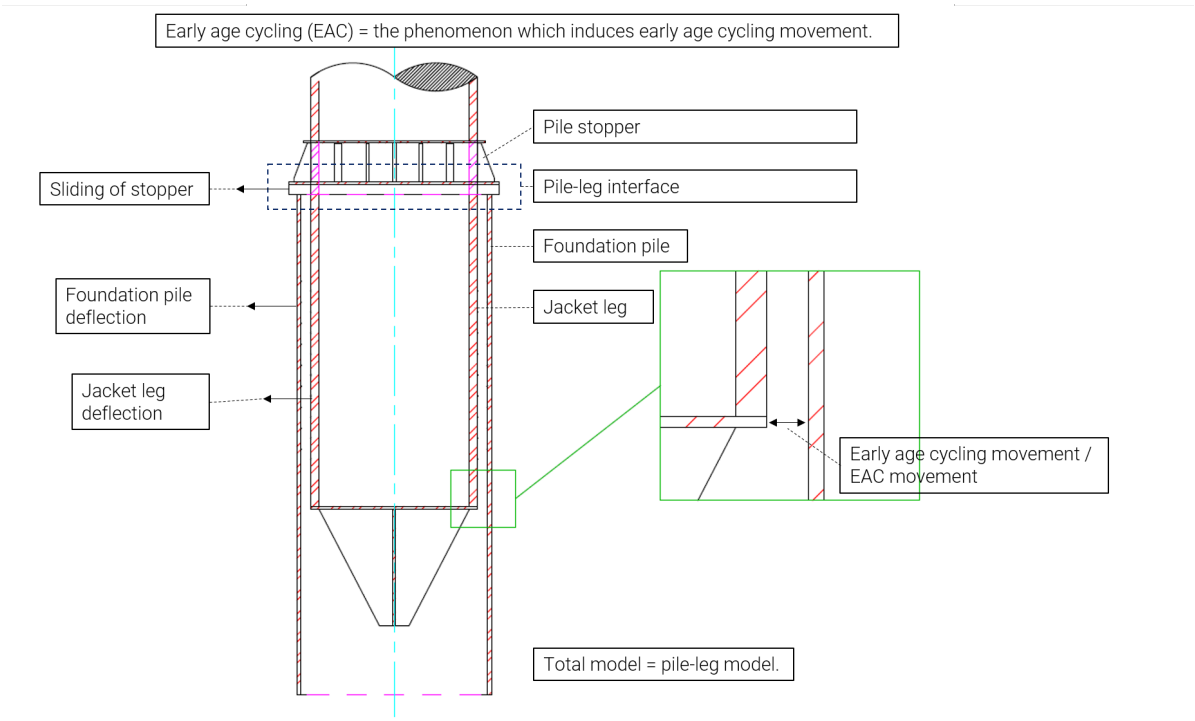

Figure 1: Terminology of pile-leg model as adopted in the *DNVGL-ST-0126* [17]

1 Introduction

1.1. Offshore wind energy

The Paris Agreement, part of the United Nations Framework Convention on Climate Change (UNFCCC), is a famous document signed by 195 countries during the 21^{st} conference of parties in Paris. The aim of this agreement is to limit the increase in global average temperature to well below 2^{o}C [71]. The main strategy to reach this target is to 1) reduce CO_2 emission, 2) increase the share of renewable energy and 3) increase the energy efficiency. A trend which is visible in a number of proactive countries these days is an increasing share of renewable energy [72]. A promising potential within this share is offshore wind energy (OWE). With relatively low sociological damage and increasing efficiency, offshore wind is becoming a big player in the energy transition [34]. However, the offshore wind market is not new and has been developing for decades. As a results a number of trends can be observed that are posing technical challenges.

First of all, the average water depth of installed Offshore Wind Farms (OWF) is increasing. The North Sea, with its relatively shallow water depth, has been the testing ground for the development of offshore wind for the last decades. From 1990 to 2019, roughly 75% of all commissioned OWF's were build in water depth below 30 meter using monopiles (MP's) [21]. However, as the capacity of installed offshore wind rises, the average dept and distance from shore increases. This is visible in the recent statistics from the International Energy Agency (IEA) [32] and International Renewable Energy Agency (IRENA) [24] as displayed in Figure 1.1.

The jacket substructure, dating back from the oil and gas industry, has proven itself reliable for deepwater locations. Due to it's multimember set-up, the jacket can facilitate sufficient stiffness in deeper water at relatively lower costs when compared to MP's [14]. Since the substructure is an important factor within the capital expenditure (CapEx) of a wind farm, this cost reduction could significantly improve the levelized cost of energy (LCOE).

Furthermore, there are other other factors that drive up the interest in the jacket structure. New markets are opening up in for example; the United States, China and Korea. These sites have proven to be more challenging with greater water depth and complex geotechnical conditions ([62] [14]). Large diameter MP's bear a high drilling risk when installed in complex soil layers. The technical options to mitigate these risks are complicated and expensive. As a result, the usage of smaller diameter foundation piles used in jacket structures becomes attractive, even for shallow water depth. Also, the MP market nowadays is dominated by a number of large players located mostly in Europe [21]. Especially for these sites outside Europe, jackets are more easily fabricated by the large number

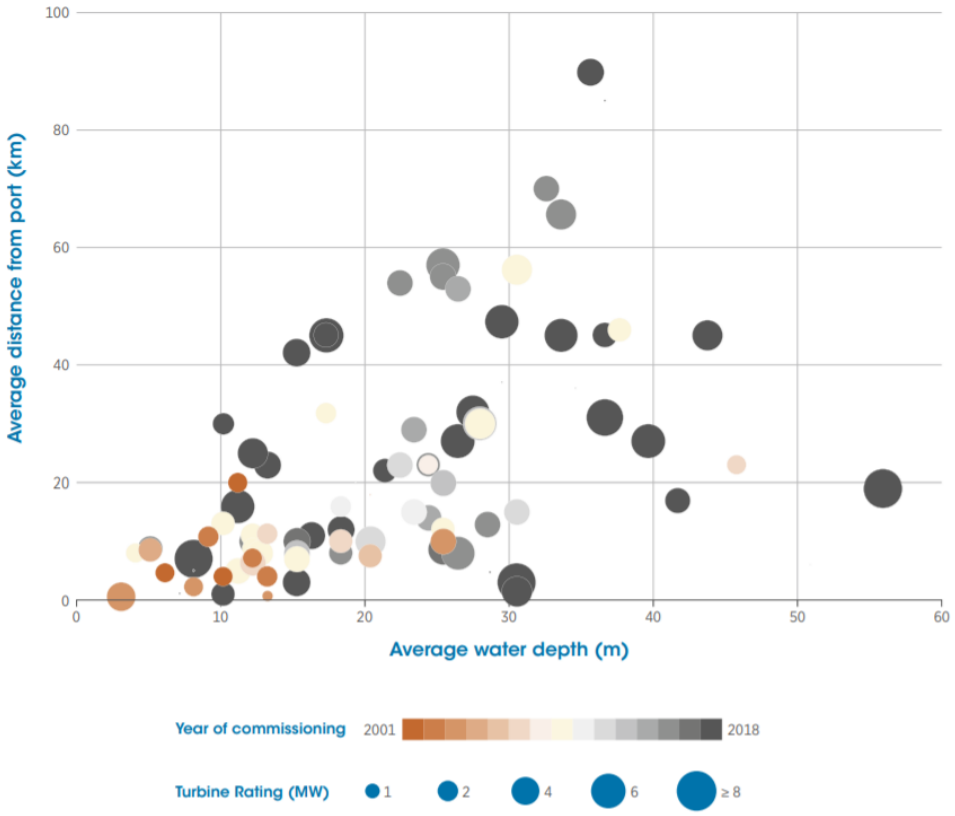

Figure 1.1: Distance to port vs. water depth for commissioned wind farms between 2001 and 2018 [24].

of steel companies working in the oil and gas industry.

As a result of these changing factors, a record amount of jackets will be installed globally in the year 2020. With a total of 258 turbines, the jacket structure will represent around 20% of the substructures installed this year [21]. Boskalis Offshore Energy is involved in the design and installation of several jacket founded OWF's. By offering large installation vessels capable of lifting and transporting jacket structures, they are a key player within this growing market.

A large problem Boskalis and the industry are facing at the moment is the strict regulation around early age cycling (EAC) as described in the *DNVGL-ST-0126 Support structures for wind turbines* [17]. The phenomenon of EAC is based on relative movement between the jacket leg and foundation pile within the first hours of grout curing. This movement can cause crack formation in the grout connection, therefore decreasing the shear capacity. The actual magnitude of this problem is not yet known resulting in over-conservative design regulations and high costs for mitigation measures. As indicated by the *DNV GL* in agreement with the industry, extra research is needed in order to better predict the behaviour and consequences of EAC.

1.2. Background

This chapter describes the background information needed to understand the problem of EAC. The general jacket installation procedure will be discussed as adopted in projects executed by Boskalis nowadays. Furthermore, a detailed overview of the pile-leg model will be discussed together with the physical consequences of EAC.

1.2.1. Jacket installation

A result of the iterative process underlying the constantly evolving jacket is the change in connection between the foundation pile and structure. This process is visualised in Figure 1.2, showing the main configurations which have been adopted during the lifetime of the jacket structure. The left configuration shows the first generation jacket structures as used in the North Sea between the 60s and 70s. In these jackets, piles were driven through the legs after which the deck structure was welded to the top of the pile. The deck structure was now fixed to the piles directly which resulted in full axial load going through the pile. Grout was mainly used to transmit lateral forces in the jacket [6]. As industry knowledge increased, jacket structures were designed more efficient and cost effective [13] resulting in the usage of sleeves to save material costs and optimize the installation procedure. For the sleeve connection, grout started to play a more important role as it would now be the only structural connection between the structure and its foundation [7]. The usage of jacket structures for the offshore wind industry has led to a further increase in design efficiency. Due to the large number of jackets within an OWF, minimizing material costs and optimizing installation time could result in a reduction of LCOE. The most common connection as used in OWF's nowadays is therefore the leg in pile configuration as shown in the right of Figure 1.2. This configuration requires the foundation piles to be installed before the jacket, therefore opening up the possibility to split the installation into two campaigns. The first campaign could efficiently install all foundation piles while the second campaign could optimally install all jackets. This leads to a more efficient use of expensive installation vessels. The leg in pile configuration will be used as default during this report as it is applicable to all projects Boskalis is currently involved in.

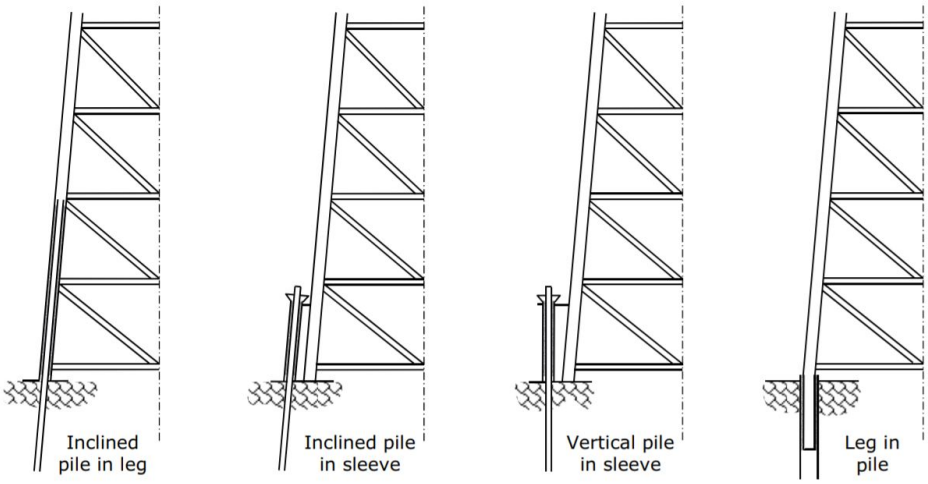

Figure 1.2: Jacket configurations [17].

A simplified jacket installation procedure for the leg in pile configuration is visualised below. This procedure covers the basic steps of jacket installation in order to create the necessary knowledge for this report.

- In order to accurately install the foundation piles into the soil, a self leveling pre-piling template will be lowered onto the seabed as visualised in Figure 1.3. The purpose of this template is to position and install the foundation piles within project tolerances. All piles are lowered into the pre-piling template and driven into the soil.

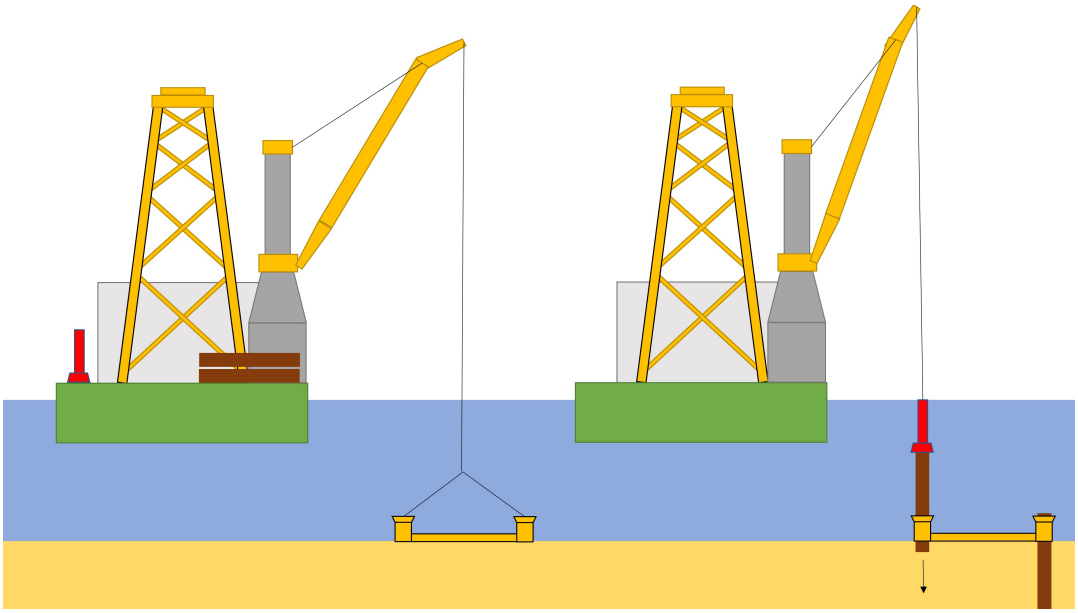

Figure 1.3: Lowering pre-piling template and pile installation.

- After all foundation piles are installed, the pre-piling template is removed as visualised in Figure 1.4. It will be re-used for all foundations in the wind farm. The foundation piles will be accurately dredged and cleaned so the jacket leg will fit in.

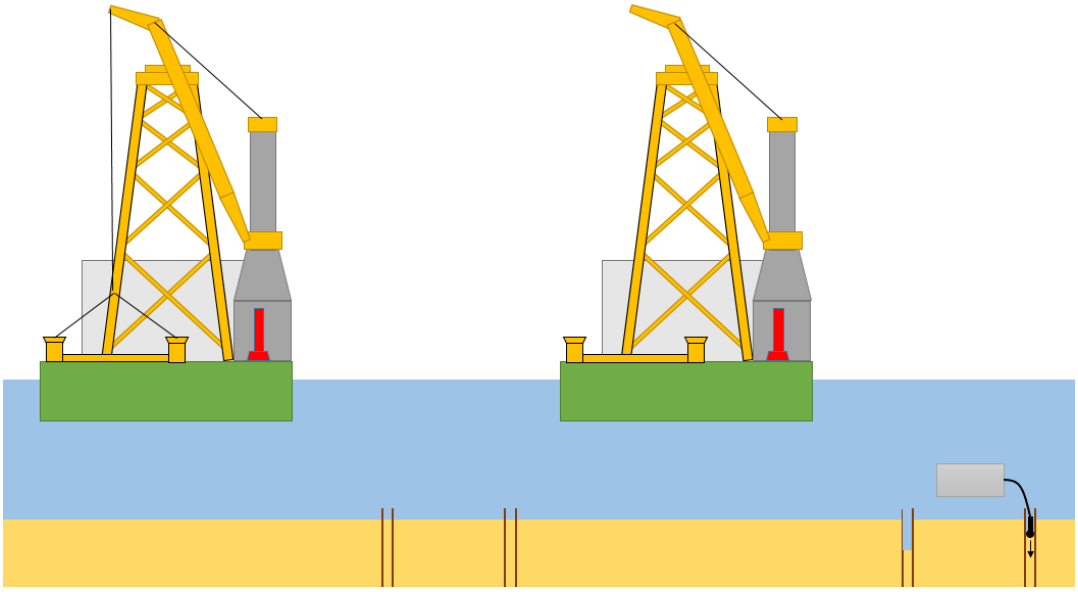

Figure 1.4: Removing pre-piling template and dredging piles.

- The jacket structure can now be lowered on the already installed piles as seen in Figure 1.5. In order to simplify this operation, pointy guiders are placed at the end of the jacket legs. A stopper is used as a temporary support to transfer loads between the jacket and the foundation pile. Other temporary supports, such as fixation cylinders, might also be used dependent on the project.

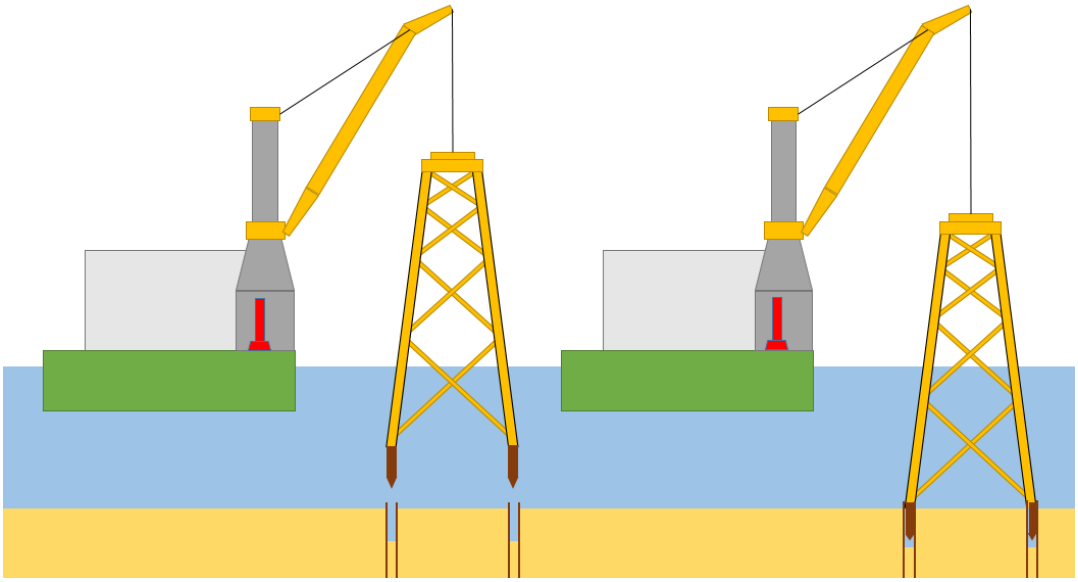

Figure 1.5: Lowering jacket into foundation piles.

- After the jacket is placed on the foundation piles, the annulus between the pile and leg can be filled with grout to secure the connection. This is done by pumping the material from the installation vessel through a temporary hose in the jacket leg. From there, the annulus will fill itself with grout while pushing the sea water out. The soil in the pile forms a natural barrier at the bottom and must therefore be removed with care. The grout which flows out of the connection at the top is checked for its quality. Whenever the quality is sufficient, proving that no water or sand is present in the annulus, the pumping operation is stopped. This process is visualised in Figure 1.6. The details of the leg in pile connection will be further explained in subsection 1.2.2. After roughly 24 hours, the grout has gained sufficient strength to make it less susceptible to any damage due to movement of the jacket. This strength increase, together with the load transfer through temporary supports, make it possible to start other work such as installation of cables or the Wind Turbine Generator (WTG). It generally takes weeks, dependent on the type of grout, until the full compressive strength of the material is reached [46]. This time dependency is further discussed in Appendix A.

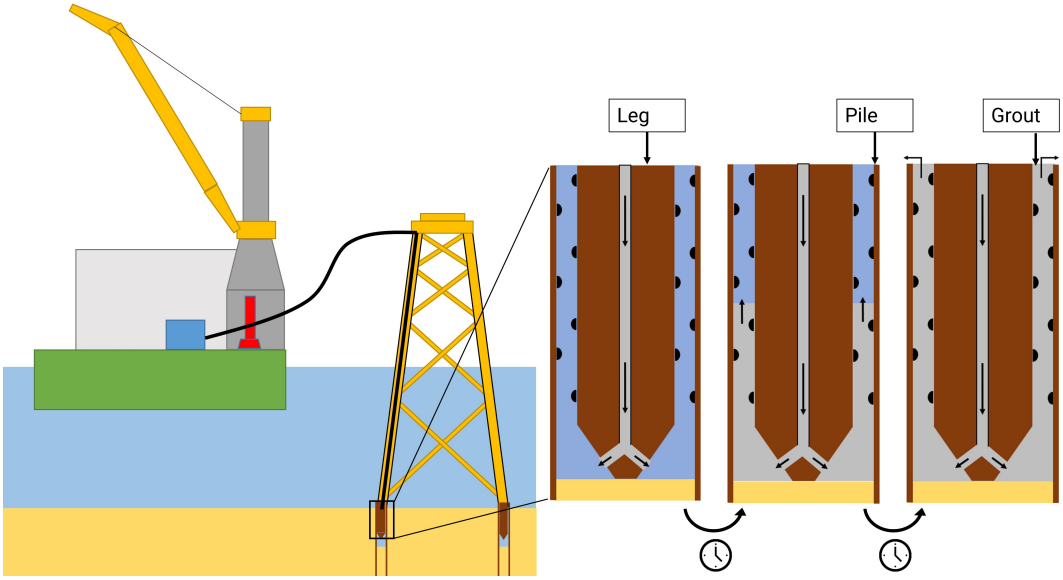

Figure 1.6: Filling pile-leg annulus with grout.

1.2.2. Leg in pile configuration

As discussed in subsection 1.2.1, temporary supports are used for the initial load transfer between the jacket and the foundation pile. The most common support is the pile stopper which is visualised in Figure 1.7, showing a more detailed overview of the leg in pile configuration. The connection between the stopper and the foundation pile is based on steel to steel friction and could therefore rotate or translate in case of large environmental loads. The actual geometry of the stopper is dependent on a number of factors as will be further explained in chapter 3. The load path through the stopper support is temporary and will be taken over by the grout when fully cured.

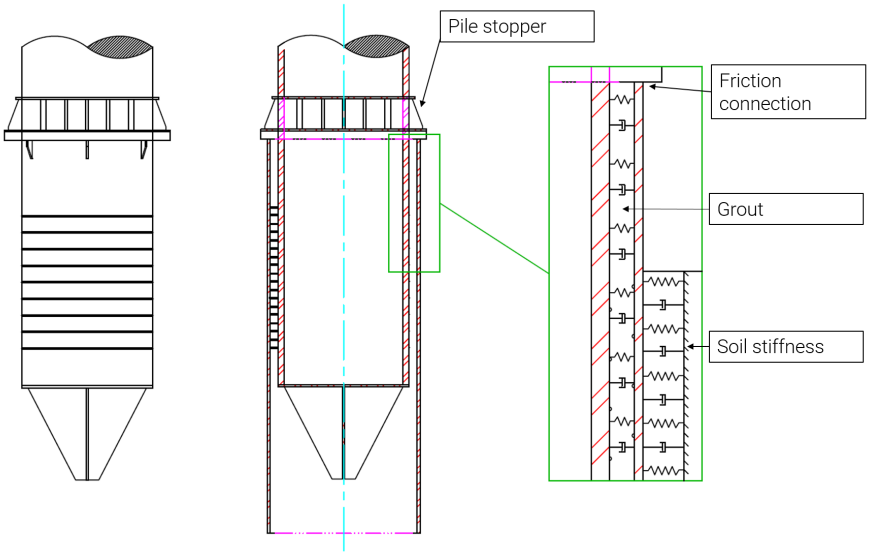

Figure 1.7: Pile-leg model overview.

As explained in subsection 1.2.1, the annulus between the leg and pile will be filled with grout. During the piling process, misalignments of the pile may occur due to varying soil layers and extreme

hammer impact. The maximum allowable rotational tolerance along the length of the pile is generally +/-0.5^o and the survey height tolerance between piles can be +/- 50 mm. This can result in a total pile misalignment of +/- 350 mm. In order to cope with these misalignments and install the jacket within installation margin, grout is used to connect the foundation to the piles. Grout is a material that consists of water, cement and fine sand aggregates. It shows a lot of similarities when compared to concrete. The main difference in this instance is that grout contains smaller aggregates and a higher water content compared to concrete. It therefore flows more easily which makes it suitable to use as a joint connector or to fill up spaces. This is important as grout has to be pumped into the leg in pile connection during installation of the jacket structure. The benefit of using grout to connect the pile to the leg is that it is an efficient way to secure the structure to the foundation while coping with the installation tolerances. It is therefore used in almost all offshore structures as no suitable efficient replacement has been found yet [13]. In present day grout connections, the pile and leg are generally fitted with shear keys. Shear keys are circumferential weld beds used to increase the shear capacity of the grouted connection which is induced when an axial load is placed on the pile or leg [50].

1.2.3. Early age cycling

The governing failure mode in a grout connection with shear keys is interface shear capacity as stated in the *DNVGL-ST-0126* [17]. This failure mode is visualised in Figure 1.8, displaying a test sample from a fatigue experiment conducted by Lotsberg for the *DNV GL* in Oslo [53]. Whenever the pile and leg are axially loaded during an Ultimate Limit State (ULS) case or Fatigue Limit State (FLS) case, most of the shear capacity will be taken by compression struts that form in the diagonal between the weld beds. These compression struts are visualised in a schematic drawing in the right of Figure 1.8. The direction of the compression strut is dependent on the direction of the axial load. Finite Element (FE) analysis has shown that with an increased axial load on the leg, tensile stresses are formed in a direction normal to the compression strut. These stresses lead to crack propagation parallel to the compression strut [51] resulting in the failure mode as visualised in Figure 1.8. The two directional zigzag pattern in Figure 1.8 indicates that this is the result of a FLS loading case.

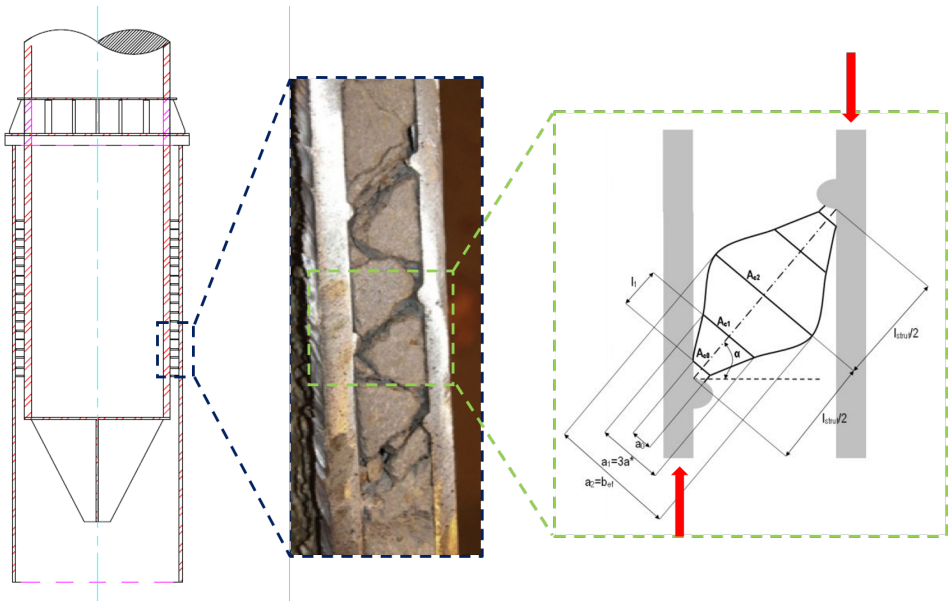

Figure 1.8: Crack formation during reversed cycling [53]. Observed failure mode is interface shear capacity.

A serious problem encountered during the installation of a jacket nowadays is the phenomenon of EAC. During the first hours of grout curing, relative movement between the jacket leg and foundation pile can locally reduce grout strength around the shear keys [47]. This local strength reduction occurs during the critical curing phase when accelerated hydration changes the grout from fluid like to solid. This is visualised in Figure 1.9 and will be further discussed in Appendix A.

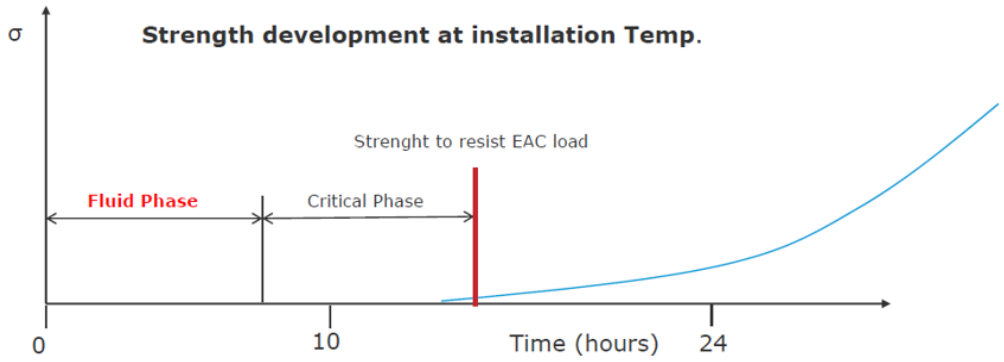

Figure 1.9: Strength development grout.

As a result of reduced grout strength along the shear keys, some relative sliding can occur between the grout steel interface of the jacket leg and foundation pile. For a static ULS case, this problem is not significant as the required strength capacity will be reached after some sliding. However, problems arise during the dynamic FLS. As a result of reversed cycling [38], larger and repetitive sliding motions will take place between the steel grout interface. As a result, the connection fails according to the interface shear capacity as shown in Figure 1.8.

The problem of EAC has always been known in the industry. For decades, design regulations adopted an empirical reduction factor to account for the decrease in shear capacity [33]. However, these reduction factors are outdated and do not represent the current high strength grouts and changing geometrical connections anymore.

Therefore, in 2014, the *DNV GL* has changed their regulation regarding EAC. The maximum relative movement between the leg and pile shall not exceed **1 mm** during the first **24 hours** of curing. This must be proven by conducting an on-bottom analysis using the maximum expected sea state in 24 hours. Furthermore, the grout can not contribute towards the stiffness in this analysis.

As indicated by the *DNV GL*, this conservative regulation is a result of limited knowledge and a lag of representative test data on the subject. A large joint industry project is needed in order to perform full scale tests and assess the actual damage due to this EAC movement. In the mean time, maximum movements are limited to 1 mm causing serious problems for the industry. In order to limit the relative movement at the sea bed, EAC mitigation measures are commonly used. These concepts are generally based on fixing the connection between the leg and the pile by means of cylinders or shims. However, these mitigation concepts are expensive and their effects are a debated issue. Decreasing the current research gap would therefore be beneficial for the *DNV GL* and the industry.

1.3. Objective and scope

As indicated by the *DNV GL* and supported by the industry, the new and strict regulation on EAC is the effect of a research gap on the subject. The available literature on EAC in a jacket structure is limited. The information which is available roots back to the 70s and 80s and has become unreliable due to the higher performance grouts available on the market nowadays and changed jacket geometry.

As can be observed in Figure 1.10, the problem of EAC can be tackled by either easing the regulation (left) or by minimizing the EAC movements (right). Easing the regulation could be accomplished by performing a large joint industry project and proving larger movements than 1 mm are acceptable. However, such a project is time consuming, expensive and therefore not feasible for this research. However, minimizing the EAC movements as visualised in the right of Figure 1.10 can contribute in great extend towards the problem the industry is facing at the moment. Performing research into efficient reduction of EAC movements could save installation time and production costs reducing the overall LCOE of an OWF.

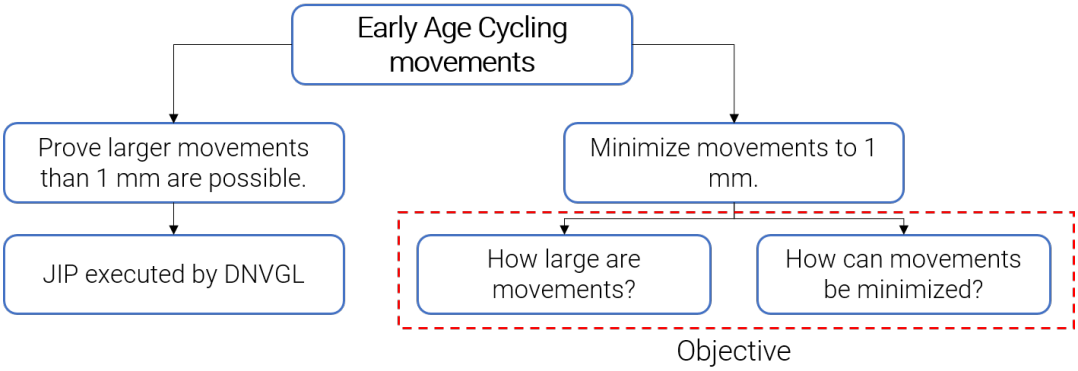

Figure 1.10: Problem solve flow chart EAC.

As visualised in Figure 1.10, the objective of this thesis is twofold. The first objective is to gain insight into the modelling approach and magnitude of EAC movements. Based on this information, the second objective will be to investigate how these movement can efficiently be minimized. This will be done by investigating various pile stoppers.

The research question that will be answered is:

"What is the relation between stopper design and early age cycling movements in the grout connection of an offshore wind jacket structure. "

1.4. Approach and methodology

Due to an extensive amount of simulations and large Finite Element (FE) models within this study, an efficient modelling approach will be adopted to approach this problem. This chapter describes the basis of this approach. Based on this, a methodology is presented in order to meet the objectives and answer the overall research question.

1.4.1. Modelling approach

In order to quantify the amount of EAC movement, the relative movement between the outer shell of the jacket leg and the inner shell of the foundation pile needs to be determined. This can be done by modelling the full jacket geometry to match the actual behaviour at sea. This includes a full geometric representation of the foundation piles including the pile-leg interface with a friction connection as visualised in Figure 1.11. The relative EAC movements can then be monitored by measuring the deflection between the outer shell of the jacket leg and the inner shell of the foundation pile. In order to accurately model the behaviour of the friction connection, the pile and leg need to be modelled using solid elements. The jacket can be modelled using beam elements. This model, as displayed in Figure 1.11, will be referred to as the full model. The only simplification between the full model and reality is the linearization of the soil-pile interaction to an apparent fixity (AF) approach. The components in this model will be further explained in chapter 2 and chapter 3.

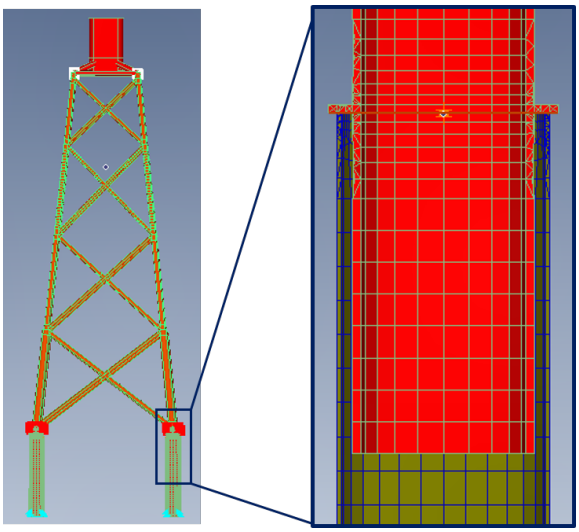

Figure 1.11: Full model.

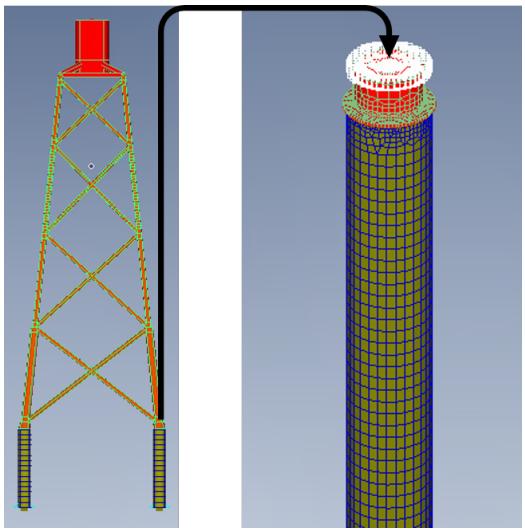

Figure 1.12: Global model (left) and detailed model (right).

Investigating this problem using a full model as displayed in Figure 1.11 has several downsides. First of all, the computational time is significant due to the complexity of the model. With roughly 70000 elements and 175000 nodes, simulations are slow. Furthermore, due to the frictional interface between the pile and leg, an extensive amount of contact iterations needs to be performed per time step. Since the basis of this research will rely on performing a large amount of analysis on the pile-leg model, it is beneficial to reduce this simulation time.

Therefore, most simulations will be performed using two models as visualised in Figure 1.12. First of all, interface forces will be determined using a global jacket model constructed with beam elements. After, a detailed study can be performed on a detailed pile-leg model constructed with solid elements. Since the number of detailed pile-leg models decreases from 4 to 1 when comparing Figure 1.11 with Figure 1.12, computational time is reduced with almost 75%. Furthermore, one could

modify the detailed model while keeping the interface conditions from the global unchanged. Figure 1.13 summarized this approach. In order to assess the uncertainty imposed by using two models, a validation will be performed using the full model. This will be further discussed in section 2.4.

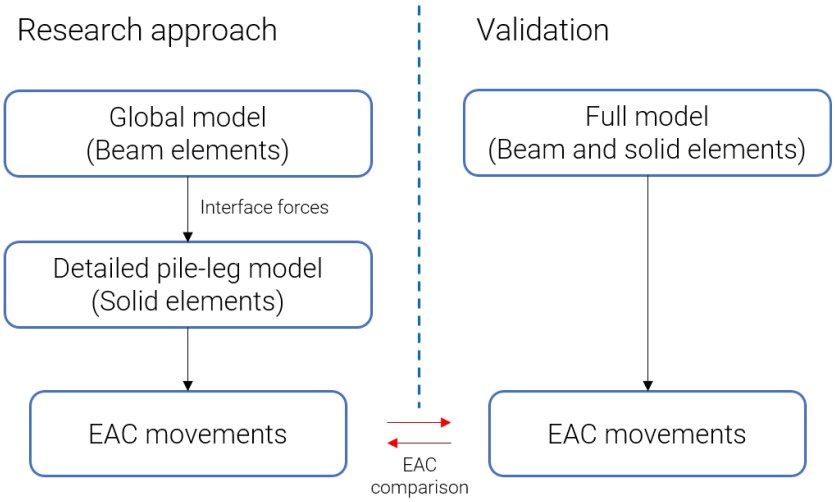

Figure 1.13: Modelling approach.

Model assumptions

Throughout this study, the assumption is made to not incorporate any grout stiffness into the model simulations. This assumption is based on the guideline of EAC as stated in *DNVGL-ST-0126* [17]. Incorporating grout stiffness is in reality difficult as its strength development is highly dependent on time and temperature in the first 24 hours. As discussed in Appendix A, the stiffness of grout is negligible for the first hours of curing. Only for the last hours of curing, whenever the right temperature is reached, grout stiffness can become significant in the reduction of EAC movement. However, including this would be advised after performing small scale tests on the material. Otherwise, due to a lack of reliable data, this would impose a large uncertainty in the simulation. This would therefore be a recommendation for any further research.

Three main assumptions that will also be used throughout this study are:

1. Dividing the total system into a global model and detailed model (discussed in this subsection and section 2.4).
2. Linearizing the soil-pile interaction by an apparent fixity method (discussed in subsection 2.2.5.
3. Simulating for a an equivalent largest design wave to replace irregular wave conditions (discussed in section 2.3 and subsection 3.2.3).

The uncertainty imposed by these assumptions will be discussed in the recommendations in section 5.2.

1.4.2. Research methodology

Figure 1.14 visualises the methodology of this research which will be used to meet the objectives as discussed in section 1.3. As can be observed, the total study will be divided into three phases. Each phase consists of a number of simulations indicated by the orange colour in the flowchart. The output of these simulations, which are movements, are indicated by the green colour. The input for these simulations, which are forces, are indicated by a blue colour. The methodology per phase will be discussed separately.

Phase 1
The main objective of phase 1 is to set up a global jacket model which can be used to determine the response for various load cases. Interface forces will be extracted from this model and used as an input for the reference model in phase 2. Phase 1 starts with the determination of the reference site as this partly results in the key geometry of the jacket structure. A global model will be made and simulated for a number of load cases. From this model, interface forces can be extracted to be used for phase 2.

Phase 2
The main objective of phase 2 is to set up a detailed reference model in order to quantify the EAC movements for the previous defined load cases. Furthermore, the objective is to gain insight into the behaviour of EAC movement for various loading conditions. Phase 2 starts with a detailed analysis of the pile-leg interface and a FE model set-up. Simultations will be run for the pile-leg model using the interface forces as determined in phase 1. The EAC results following from these simulations will be analysed. The load cases yielding the governing EAC movements will be used for the analysis of phase 3.

Phase 3
The main objective of phase 3 is to analyze the effect of a number of key stopper parameters on the behaviour of EAC movement. Phase 3 starts by investigating three configurations for the governing load cases as determined in phase 2. Each configuration will be analysed by performing an area and friction sensitivity study. Furthermore, each configuration will be tested for varying wave directions.

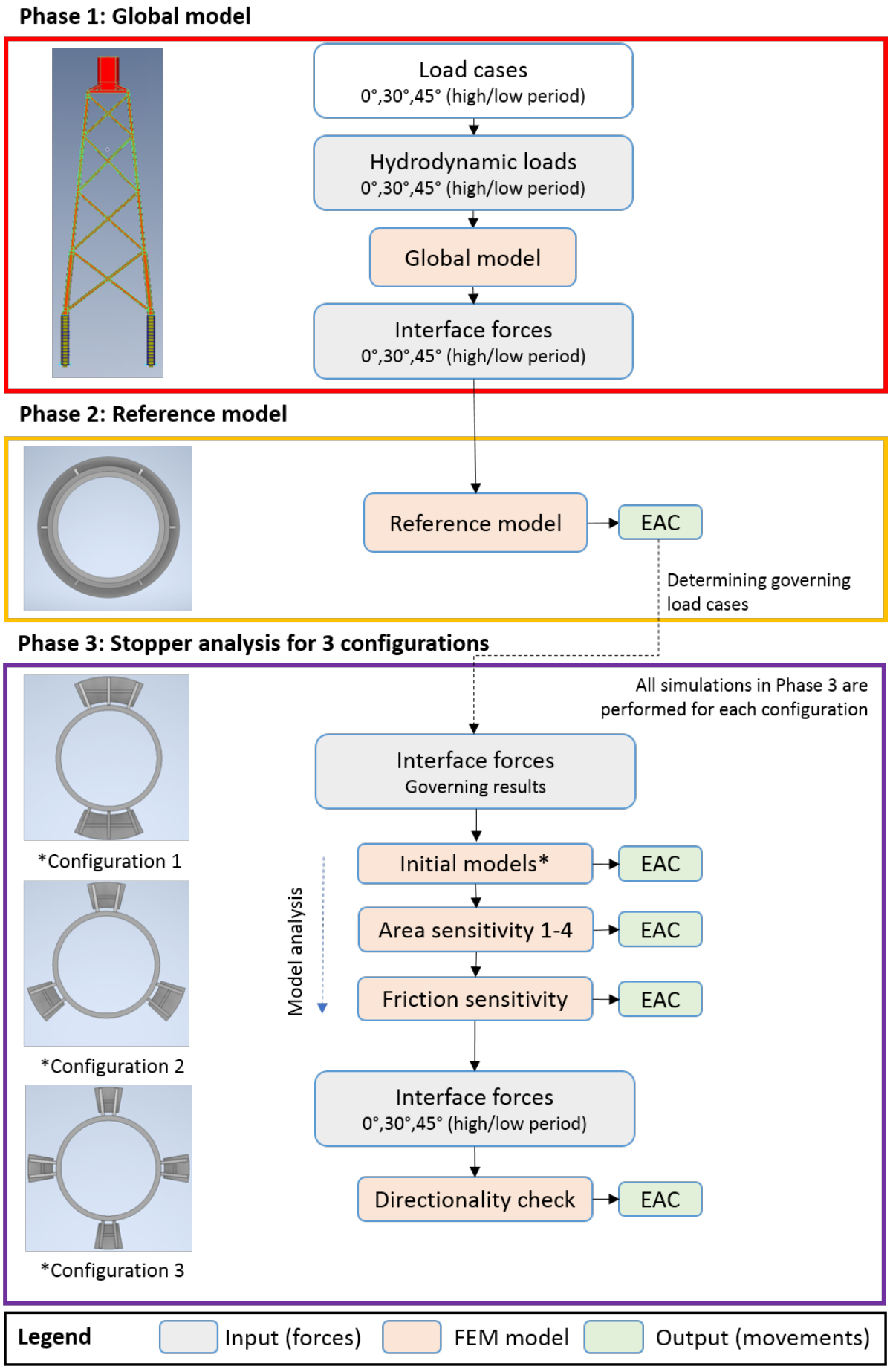

Figure 1.14: Research methodology.

2

Phase 1: Global model

The main objective of phase 1 is to set up a global jacket model which can be used to determine the response for various load cases. Interface forces will be extracted from this model and used as an input for the reference model. All assumptions that need to be made in order to achieve this will be justified in the following chapter.

The first phase is divided into four sub phases as visualised in Figure 2.1. First of all, the designated site will be selected. This will partly determine the global jacket geometry and will therefore, till some extend, scope the project. These jacket dimensions will be used to create a global FE model in Femap [65]. This FE model will be used to simulate the jacket behaviour to specified load cases. These load cases will be determined based on the *DNVGL-ST-N001 Marine operations and marine warranty* [19] design regulations in order to map all possible conditions encountered during the grouting operations and curing. The interface conditions will then be extracted from the global jacket model. These will act as an input for the detailed analysis in Phase 2.

Figure 2.1: Overview phase 1.

2.1. Site specifications

Site selection together with WTG size will influence the jacket geometry and therefore the EAC movements in the grout connections. Key site parameters that can influence this research till great extend are:

- Water depth
- MetOcean conditions
- Soil conditions
- Special site characteristics (seismic activity, typhoon danger etc).

Conducting this research for a site in Taiwan, where deep water, complex soil conditions, seismic activity and typhoon danger can be expected [62], will result in different jacket geometry compared to a site in the North Sea. These geometrical changes could be the variation between a three or four legged jacket, flooded members or deeper foundation piles. The influence of WTG size will also have a large impact on the geometry of the jacket. Although the WTG will not be present in this study, the size will influence the geometry and therefore the EAC movements. In order to thoroughly scope this research project, a single site will therefore be chosen together with a fixed WTG.

The reference site which will be used is the Inch Cape Wind farm which is, as visualised in Figure 2.2, located at the north-west of Scotland. The WTG used for this projects has a capacity of 9.5 MW. The main consideration to investigate this site is the extensive amount of data Boskalis has got on it. This not only includes MetOcean conditions but also a detailed geometric design. This will therefore increase the accuracy of this research.

Inch Cape Wind farm consists of 72 jacket foundations divided into three clusters based on water depth. The shallow cluster ranges from 43 to 47 m of water depth, the intermediate cluster from 48 to 51 meters and the deep cluster from 51 to 54 meters. For this analysis, a jacket from the deep cluster will be used to define a scope. There is no quantitative research predicting whether this will yield the largest deflections. Although the hydrodynamic forcing is higher for a large jacket, the smaller stiffness of a shallow jacket might induce more EAC movement. A further study should further investigate this difference.

Figure 2.6 shows the general arrangement of the Inch Cape jacket structure. The jacket is 4 legged and consist of only inclined members. The width at the sea bed is 26 meters and the overall parameters for a deep cluster jacket are displayed in Table 2.2.

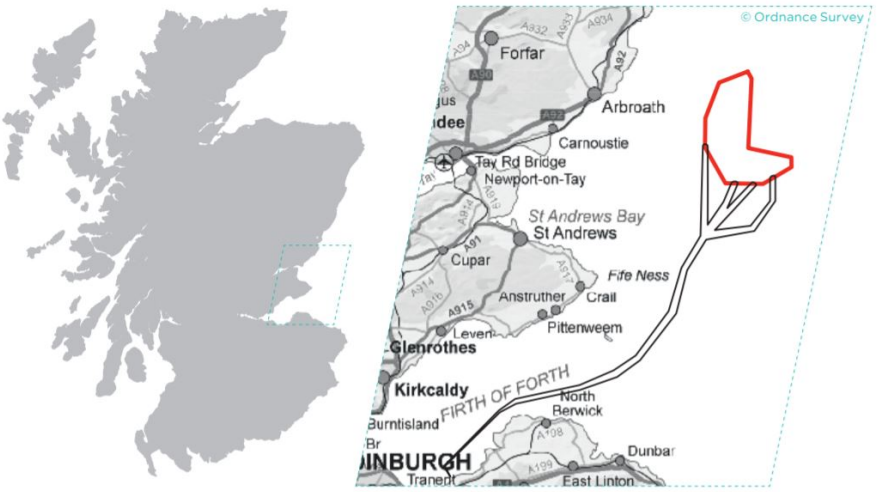

Figure 2.2: Location of Inch Cape Wind Farm and Offshore Export Cable Corridor [31].

2.1.1. MetOcean data

As part of the Inch cape project, an extensive MetOcean study has been performed. Figure 2.3 shows a rose plot of the annual significant wave height (H_s) [m] versus the mean wave direction (MWD) [^{o}] for the total sea state. This comprises the wind induced waves and swell induced waves.

Figure 2.4 and Figure 2.5 show the annual swell induced significant wave height and the annual wind induced significant wave height respectively. As one can clearly see, the main swell direction ranges from the north-east to south-east. This can be justified by the fact that all other directions are

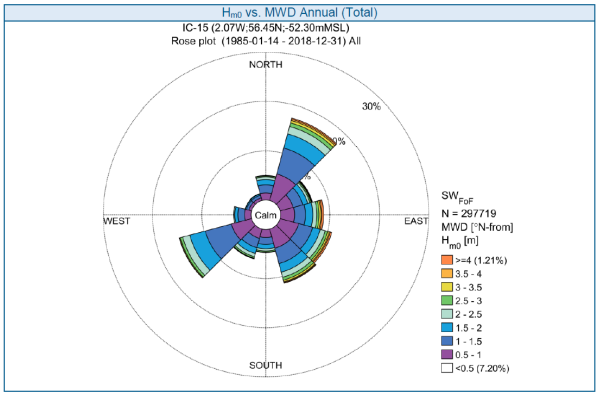

Figure 2.3: Total annual significant wave height versus direction.

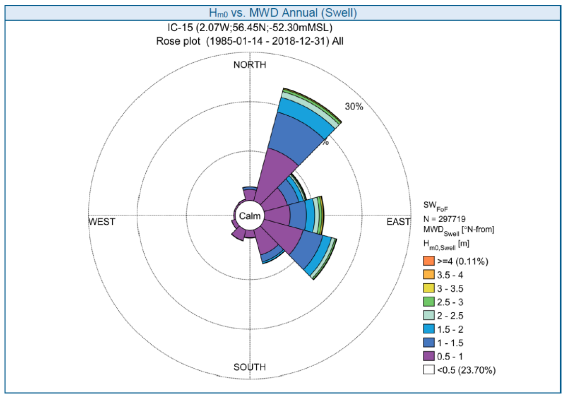

Figure 2.4: Total annual swell induced significant wave height versus direction.

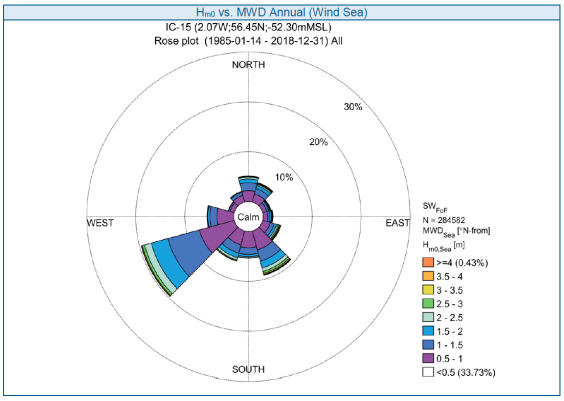

Figure 2.5: Total annual wind induced significant wave height versus direction.

shaded by the mainland of Scotland. The wind induced waves on the other hand are predominantly formed in the main North Sea wind direction which is south-west ([69][70]) . As a result, two kind of wave directions might be experienced simultaneously. Furthermore, referring to Table 2.1 which shows the MetOcean statistics, one can conclude that the swell induces wave period is much longer compared to the wave induced period. This might result in a complex load combination which could yield unfavourable jacket response from an EAC point of view.

The measured governing wind direction at the site is from the south-west. The 2 hour average wind speed at 10 m height is displayed in Table 2.1. The measured current is following the coastline and running north-northeast to south-southwest. This is predominantly tidal induced current and a small amount of residual current. All MetOcean statistics are displayed in Table 2.1.

Table 2.1: Inch Cape MetOcean statistics.

	$H_{s,total}$ [m]	$T_{p,total}$ [s]	$H_{s,sea}$ [m]	$T_{p,sea}$ [s]	$H_{s,swell}$ [m]	$T_{p,swell}$ [s]	U_{10} [m/s]	Current [m/s]
Min	0.1	1.5	0.0	1.0	0.1	2.0	0.0	0.00
Mean	1.4	6.8	0.9	4.1	0.9	7.9	7.6	0.29
Max	7.9	22.4	7.6	12.9	6.6	23.1	27.3	0.95
Std	0.8	2.5	0.7	1.6	0.6	2.7	3.6	0.15

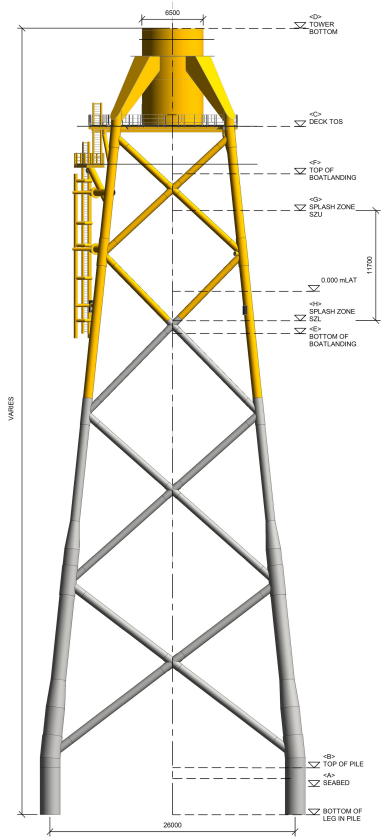

Figure 2.6: General arrangement Inch Cape jacket structure.

2.2. Model set-up

The global geometry of the Inch Cape jacket, as designed by Boskalis, is visualised in Figure 2.6. The specific dimensions of the largest deep cluster jacket are displayed in Table 2.2.

Table 2.2: Jacket dimension with respect to LAT in meters.

Hub height	Water depth	Top of pile	Top of deck	Tower bottom	Bottom of BL	Top of BL	Upper splash zone	Lower splash zone
123	-54.59	-50.64	17.53	27.96	-5.00	12.50	9.00	-2.70

The detailed jacket design is used in order to create a global FE model in Femap. The global FE model is displayed in more detail in Appendix B. Beam elements are used to describe the members as they provide accurate results for framed structures [17]. Furthermore, beam elements are suitable as the total response of the jacket is of interest and not the stress in a specific section. All members and braces have a characteristic diameter and thickness to describe the cross section. These diameters and thicknesses are generated from the detailed jacket design as used by Boskalis. The foundation piles are also represented by beam elements and are rigidly connected to the jacket frame. An AF length will be used in order to account for the soil-pile interface. This will be further explained in subsection 2.2.5.

The transition piece should in reality be modelled by plate elements if a higher accuracy is needed around this area. However, as it structurally does not contribute in a large extend towards the EAC movement in the foundation pile, it is simplified as beam elements. All structural elements are

modelled using S355 steel as material property. This is a commonly used offshore structural steel [28] according to European standards. The material properties are displayed in Table 2.3.

In general the global jacket model is meshed such that all members and braces between two joints form an element. The loads which will be added to the model are nodal point loads as will be further discussed in subsection 2.2.2 and subsection 2.2.3. A higher element density will be used around the waterline as the largest wave kinematics and thus the largest loads will be experienced there. This will increase the overall accuracy of the model.

Table 2.3: S355 steel material properties.

Youngs Modulus	Poisson ratio	Tension Limit stress	Mass density
210 [Gpa]	0.3 [-]	355 [Mpa]	7850 [kg/m^3]

2.2.1. Static versus dynamic behaviour

The global model will be solved using the FE analysis solver NX Nastran. There are several types of analysis that can be performed based on the desired output. A first distinction which should be made is whether the analysis can be simplified from dynamic to quasi-static as this could significantly reduce the computational time. Running a dynamic analysis on an irregular sea state would require to run long time series in order to skip the initial transient response and capture all dynamic effects. Simplifying the analysis to quasi-static would result in the simulation of a single wave period.

The first natural frequency of the jacket is $\omega_{n,1}$=1.419 Hz which is relatively high as the structure has a high stiffness compared to the mass due to the missing turbine. In order to position this frequency within a wave and wind spectrum, the power spectral density of a small period wave and extreme wind are calculated as visualised in Figure 2.7. Furthermore, the design bandwidth of the total system is displayed whenever the turbine is installed to provide perspective on the relative difference.

For the sea state, a JONSWAP spectrum [25] is taken with a general peak enhancement factor of γ=3.3 [-]. A small period wave is used as this could excite the high natural frequency of the structure. This corresponds to a H_s=1 m and T_p=3.6 s. For the irregular wind, a Kaimal spectrum [40] is adopted with a turbulence intensity of I=0.14 [-] and a turbulence length scale of l_t=340 m. A 2 hour maximum mean wind speed at 10 m height is taken as U_{10}=27.3 m/s. As can be seen from Figure 2.7, the first natural frequency of the jacket, compared to the total system is significantly higher. Running the simulation using an irregular sea state will, due to the high natural frequency, most likely not result in any dynamic response. A quasi-static approach will therefore be used as default. However, in order to verify this assumption, two dynamic simulations will be run using an irregular sea state. These cases will be further explained in section 2.3.

2.2.2. Hydrodynamic loads

The load calculation for this model is based on the *DNVGL-RP-C205 Environmental conditions and environmental loads* [18] design guide which is the industry standard at this point. All loads will be calculated in the Boskalis in-house developed Python Design Tool (PDT) [8] and are based on the global model node coordinates. They will then be exported to Femap and applied to model by means of nodal point loads.

The water particle kinematics that will be used to determine the hydrodynamic loads can be due to

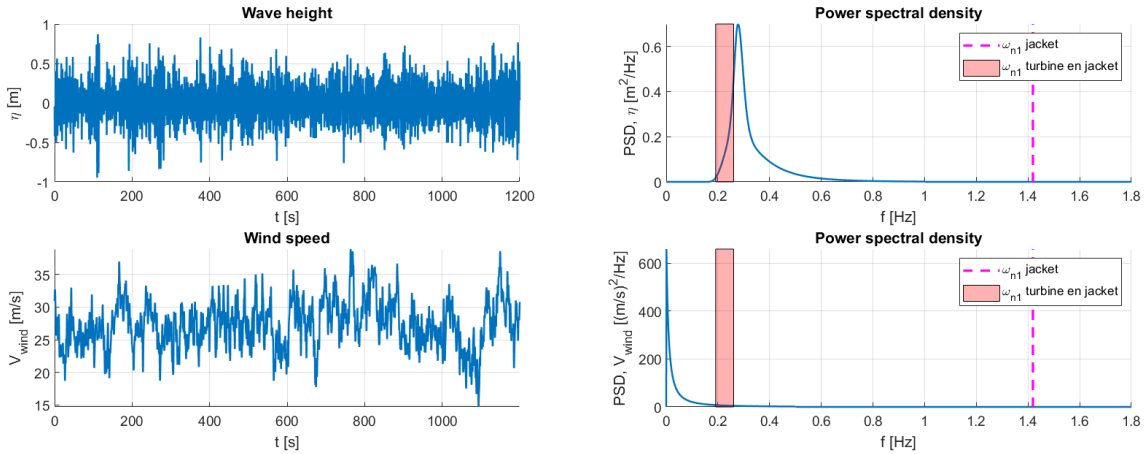

Figure 2.7: Power spectral density of irregular wave and wind time series.

wave or current effects dependent on the load case. The current will cause a steady particle motion changing direction every six hours. This will therefore result in an offset of the jacket oscillating with a large period. The wave loads will cause a short period cyclic motion. As discussed in subsection 2.2.1, all load cases will be simulated using a quasi-static analysis. For this reason, a regular design wave will be used as input for the model. The benefit of this approach is a significant decrease in computational time. A stokes 3^{rd} order wave will be used in order to map the particle kinematics. More information on this can be found in Appendix C.

The hydrodynamic loads that will be applied to the global model are calculated using the Morrison equation [56]. This equation is generally valid whenever the condition $\lambda > 5D$ is satisfied. Here, λ is the wave length [m] and D is the diameter [m] of the jacket member. For this simulation the jacket is assumed to be a fixed structure within the waves and current as the movement of the jacket will be very small. The velocities and accelerations will therefore also be small and will not have a significant effect of the hydrodynamic forces. As a result, the Froude-Krylov force and the velocity and acceleration of the structure can be neglected.

The Morison equation divides the wave forcing into a drag and inertia component as shown in Equation 2.1. As the flow direction with respect to the members and braces is generally under an angle, the force components can be dived into a normal force, tangential force and lift force as displayed in Figure 2.8.

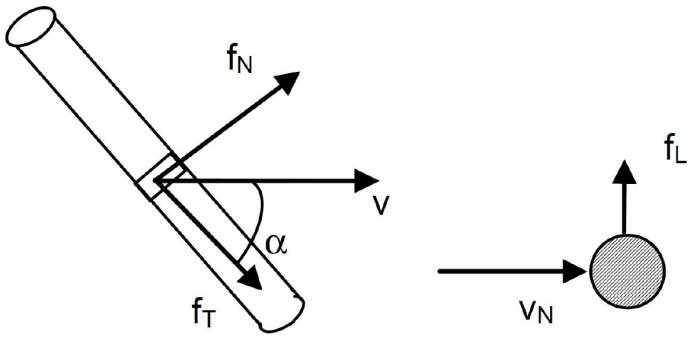

Figure 2.8: Definition of normal force f_N, tangential force f_T and lift force f_L on an inclined slender structure [18].

The normal force per unit length f_N [N/m] is found using the Morison equation with the normal velocity components of the water particles. The tangent force per unit length f_T [N/m] is a result of skin friction and is mostly negligible small [44]. As only the first 24 hours after jacket installation are of interest, there will be no marine growth present resulting in low skin friction. The tangent force will therefore be neglected. The lift force f_L [N/m] can be induced due to unsymmetrical cross-sections, wake effects or vortex shedding. Due to the symmetry of the jacket structure, this force component will be small. It will therefore also be neglected. The normal drag component and normal inertia component of the Morison equation can therefore be calculated using Equation 2.2 and Equation 2.3 respectively.

$$f_{\text{hydro}} = f_{\text{drag}} + f_{\text{inertia}} \tag{2.1}$$

$$f_{\text{drag}} = \frac{1}{2}\rho C_D A v_N |v_N| \tag{2.2}$$

$$f_{\text{inertia}} = \rho(C_M) A \dot{v_N} \tag{2.3}$$

The Morison equation calculates force per unit length f_{hydro} [N/m] and is valid for a 2-dimensional non uniform flow normal. ρ denotes the water density [kg/m^3], v_N and $\dot{v_N}$ are the water particle velocity [m/s] and acceleration [m/s^2] normal to the member respectively. A is the cross-sectional area of the member [m^2], C_M is the inertia coefficient [-] and C_D is the drag coefficient [-]. The total force is obtained by integrating the force per unit length over the length of the member.

From a physical point of view, the wave force in the Morison equation is a superposition of the drag force which is in phase with the flow acceleration and the inertia force which is in phase with the flow velocity. The assumptions made here is that the the submerged members of the structure have no influence on the wave loads. Also, flow induced vortices or the influence of velocity vectors in different directions are not taken in to account. These effects must be accounted for by two empirical coefficients, the drag (C_D) and inertia (C_M) coefficients. These coefficients are determined in various different ways.

The drag coefficient (C_D) [-] is dependent on the Reynolds number (Re) [-], Keulegan-Carpenter number (K_c) [-] and the surface roughness (k) [-]. The mass coefficient (C_M) [-] is dependent on the Keulegan-Carpenter number and the surface roughness. A more in depth explanation on these parameters can be found in Appendix C.

2.2.3. Wind loads

As described in the *DNVGL-ST-0126* [17], wind loads will not contribute in a great extend towards the EAC movement. This is mostly because the assumptions is made that the relative contribution with respect to the hydrodynamic loads is small. However, in order to justify this statement, a conservative constant wind load will be investigated in the simulation. Simulating for a time varying wind load would, due to the high first natural frequency, not lead to any dynamic response. The simulation can therefore be simplified to a constant wind load.

The largest part of the jacket structure which is susceptible to wind is the transition piece, due to its large area. It can be conservatively modelled as a large box as visualised in Figure 2.9. The wind load can then be calculated using Equation 2.4.

$$F_W = CqS\sin\alpha \tag{2.4}$$

Here, C [-] is the shape coefficient which can be taken as approximately 0.9 for a 3D rectangular box

with the dimensional ratio of a transition piece [18]. S is the projected area [m^2] of the transition piece, in this case the area of the rectangle normal to the wind direction. α is the angle [^{o}] between the wind direction and the exposed member which will be taken as 90^o, 70^o and 45^o to match the load angles of the wave and current load cases as will be discussed in section 2.3. q is the basic wind pressure [N/m^2] which can be calculated using Equation 2.5.

$$q = \frac{1}{2}\rho_a U_{T,z}^2 \tag{2.5}$$

Here, ρ_a is the density of air [kg/m^3] and $U_{T,z}$ is the average wind velocity [m/s] over a time interval T [s] at height z [m]. The height of interest is at the centre of the 'box' around the transition piece. $U_{T,z}$ at this height can be found by extrapolating the wind speed at 10 m height using the logarithmic wind profile as described by Equation 2.6.

$$U(z) = U(H) \cdot \left(1 + \frac{\ln\left(\frac{z}{H}\right)}{\ln\left(\frac{H}{z_0}\right)}\right) \tag{2.6}$$

Here, $U(z)$ is the wind speed [m/s] at height z [m]. $U(H)$ is the wind speed [m/s] at reference height H [m], in this case 10 m. z_0 [-] is the roughness parameter which can vary between 0.0001 to 0.001 depending on the amount of waves. For this case, 0.01 is taken as this results in the most conservative approach.

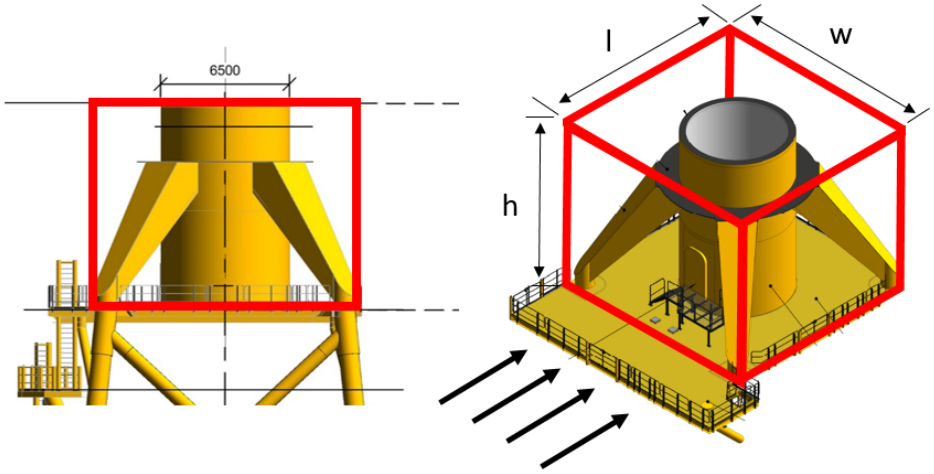

Figure 2.9: Wind force on transition piece.

2.2.4. Buoyancy

The buoyant forces of the jacket depend on the amount of unflooded/flooded members which is an important design parameter. From an EAC point of view, more unflooded members will result in more buoyant force decreasing the normal force at the friction connection of the stopper. 'Lighter' jackets are therefore more susceptible to encounter slipping between the pile and leg. For the Inch Cape project, the self weight of the deep water jacket is roughly 1200 ton including the TP weight. The average normal force in water is around 926 ton corresponding to 20 % or 274 ton of buoyant forces. This will be set as a fixed parameter for this research. However, the influence of submerged jacket weight on EAC movement is interesting to investigate and will be further mentioned in chapter 5.

2.2.5. Soil-pile interaction

An important aspect within the global jacket model is the interaction between the soil and the foundation piles. The behaviour of soil under cyclic loading is very complex and until now not fully understood [5]. Capturing the full nonlinear complexity of soil in a FE model is a difficult and time consuming task. Simplifying or linearization of the soil-pile interaction is industry practice and has proven to give accurate results ([9],[75]).

There are several foundation models available in order to simplify the soil-pile interaction. Commonly used models are based on work done by Passon [59] and Jonkman et. al [39]. As displayed in Figure 2.10, these models are based on the usage of distributed springs, apparent fixity and coupled springs.

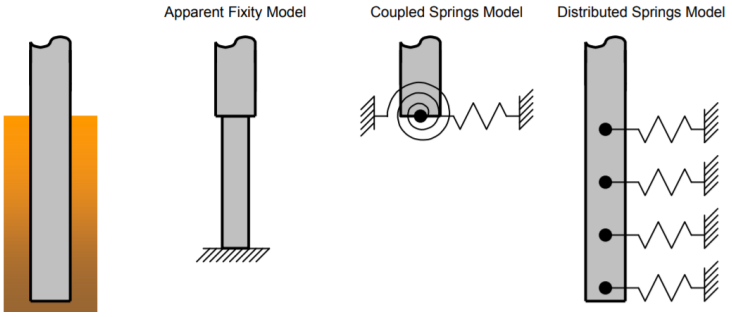

Figure 2.10: Soil-pile interaction models [39].

These models are dependent on soil properties and therefore differ per site. For the Inch Cape project, extensive soil data is available for different site locations. For this analysis, the deep water location with the softest soil profile will be analysed. A soft soil profile will result in large pile deflections and therefore large EAC movement. The soil profile at the designated location is displayed in Figure 2.11. As one can observe, a relatively soft clay layer is present near the soil surface with an undrained shear strength of s_u = 20 kPa. Due to this soft later, in order to obtain sufficient lateral and axial capacity, the designed pile length on this site is 50 meter.

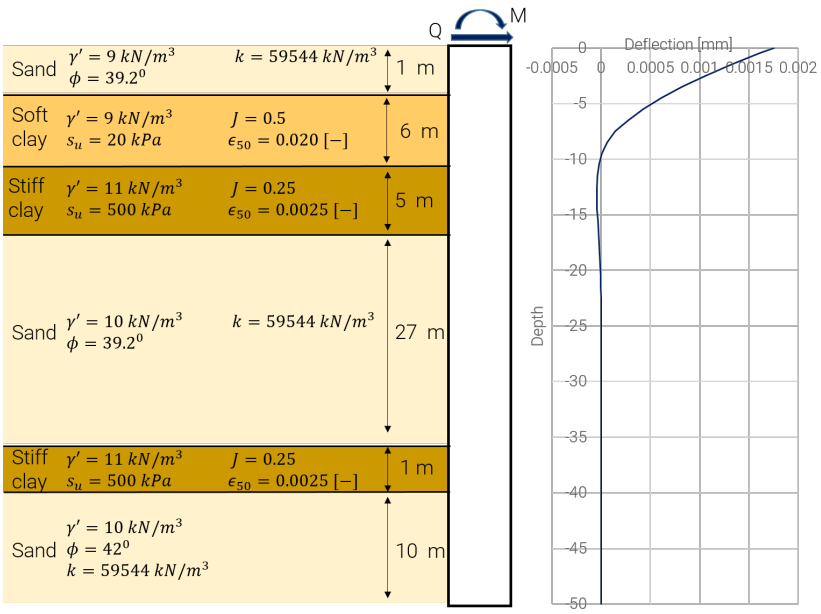

Figure 2.11: Soil profile and pile deflection example Inch Cape.

An accurate way to simplify the soil-pile interaction is the usage of distributed springs [59],[39]. This model simplifies the soil layers as discrete lateral springs. Each spring is characterised by a non-linear p-y curve representing the elasticity of the soil. P-y curves can be determined based on recommendations from the *API-RP-2A-WSD* [3] or *DNVGL-ST-0126* [16] and differ per soil layer. A more in-depth explanation on the p-y calculation is given in section D.1. Based on these recommendations, the p-y curves or load displacement curves for the Inch Cape site can be computed. By adding these load displacements curves to the full length foundation pile, realistic values can be obtained for the seabed deflection w [m] and rotation ϕ [^{o}] at a given seabed shear force Q [N] and moment M [Nm] as visualised in Figure 2.11.

A commonly used linearization of the discrete spring model is the AF method which further simplifies the soil-pile interaction. It is based on modelling the foundation pile with equivalent properties below the mudline in order to match the stiffness of the p-y pile system. As displayed in Figure 2.12, the foundation pile is modelled as a cantilever beam, not taking into account the effect of shear deformation. The equivalent length l_f [m] or AF length of this beam should yield the same seabed deflection w [m] and rotation ϕ [^{o}] as the p-y model. Furthermore, the overall dynamic response of the system should be similar as to the p-y model [39].

As the pile-leg interface is located above the seabed, no relative movement of any sort will occur in the soil submerged part of the foundation piles.

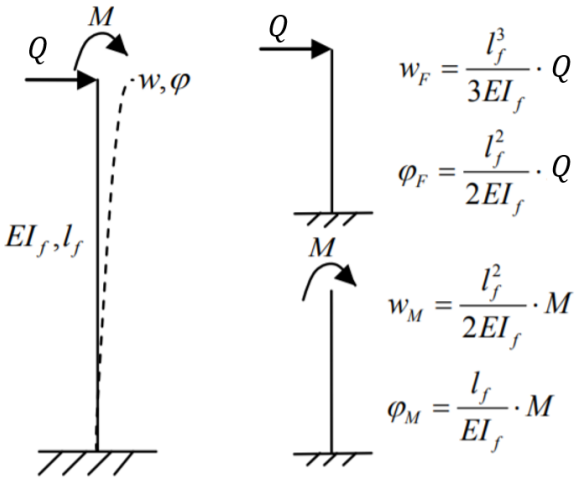

Figure 2.12: Apparent fixity model [75].

By combining the equations from Figure 2.12, the following relation can be found for the displacement and rotation of a cantilever beam.

$$EI_f = \frac{Ql_f^3}{3w} + \frac{Ml_f^2}{2w} \tag{2.7}$$

and

$$EI_f = \frac{Ql_f^2}{2\phi} + \frac{Ml_f}{\phi} \tag{2.8}$$

Equation 2.7 and Equation 2.8 should be satisfied to match the p-y model. This results in an equivalent pile length l_f [m], equivalent bending stiffness EI_f [Nm^2] and an equivalent density ρ_f [kg/m^3].

In this case, the objective is to keep $EI_f = EI$ [Nm^2] so only the AF length l_f [m] needs to varied. Furthermore, the natural frequencies of the two models should be in range.

Based on the full p-y model, as shown in section D.1, the deflections w [m] and rotations ϕ [^{o}] can be determined for a set of mudline shear forces Q [N] and moments M [Nm]. This is done by modelling the pile in FEMAP and applying 50 non-linear springs to represent the soil stiffness. Based on the obtained deflections w and rotations ϕ, the AF length l_f [m] can be calculated by either using Equation 2.7 or Equation 2.8.

Since there might be a period of time between pile installation and grouting, the effect of scour needs to be taken into account. This will mainly be induced by current and can vary based on a large number of variables. As a rule of thumb, the *DNVGL-ST-0126* [17] states a relation of $S/D = 1.3$ for current induced scour where S is the water depth [m] and D the pile diameter [m]. This results in a approximate scour depth of 3.25 m which is taken into account during the simulations. This will most likely be a conservative estimate since only the top meter is sand after which cohesive clay layers start. Scour will occur less within these cohesive layers.

Due to the non-linearity of the soil, the applied shear force and moment will influence the AF length. Figure 2.13 shows the AF length for a large range of load cases with a scour depth of 3 m. As can be observed, the AF length start to increase when the non-linear regime of the p-y curves is reached (Load case 5: Q=500 kN, M=500 kN). Before this, the p-y springs behave linear resulting in a constant AF length. Since a high AF length will result in large EAC movement, the highest load combination will be governing to assure a conservative approach. This design loadcase, as obtained from the Inch Cape detailed design, results in a shear force Q of around 3 MN and a bending moment M of around 3 MN. The corresponding AF length is 12 meters.

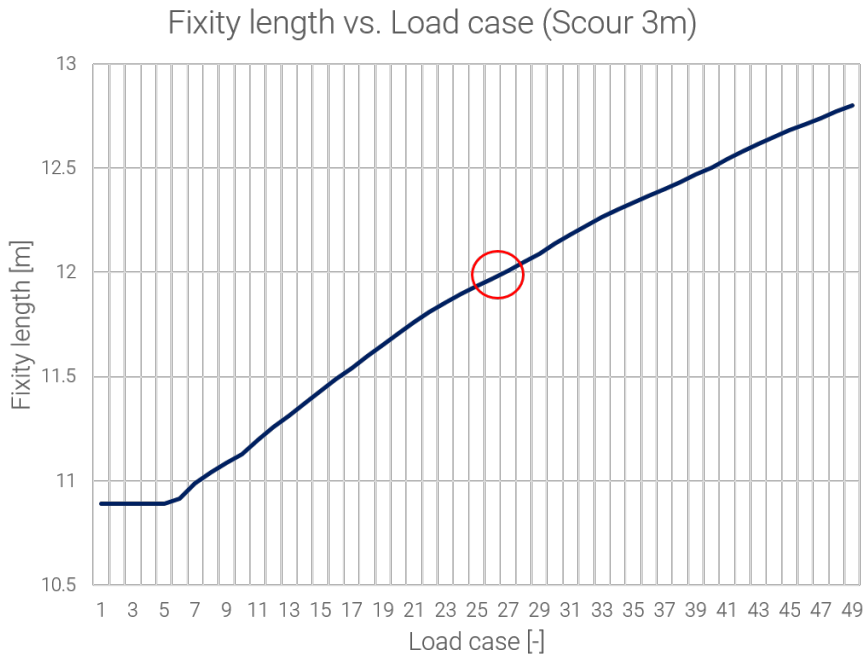

Load case [-]	Q [kN]	M [kNm]
1	200	200
3	400	400
5	600	600
7	800	800
9	1000	1000
11	1200	1200
13	1400	1400
15	1600	1600
17	1800	1800
19	2000	2000
21	2200	2200
23	2400	2400
25	2600	2600
27	2800	2800
29	3000	3000
31	3200	3200
33	3400	3400
35	3600	3600
37	3800	3800
39	4000	4000
41	4200	4200
43	4400	4400
45	4600	4600
47	4800	4800
49	5000	5000

Figure 2.13: Fixity length for all load cases with a scour depth of 3 m.

The AF method is based on matching the lateral displacement of the p-y model to the cantilever beam. However, the axial force in a jacket structure can be relatively high compared to shear force and moment [52]. Due to this large axial force, one should consider the effects of secondary moments when the pile deflects laterally. These secondary moments (P-Δ effects) can be significant for

high high axial force (P) or deflection (Δ). The previously discussed governing loadcase ($Q \approx 3$ MN , $M \approx 3$ MN) corresponds to an axial force of $P \approx 22$ MN. In order to asses the effect of secondary moments, two governing loadcases are simulated. One including axial force and one excluding axial force. The difference in lateral deflection is determined and summarized in Table 2.4. As can be noted, the relative contribution (2.3%) of secondary effects are small. This is in line with observations made by Bush et al. [9]. Due to the relatively small lateral displacement, the effect of shear and moment are of greater importance resulting to negligible secondary effects. These effects will therefore be neglected in this research.

Table 2.4: Lateral deflection including secondary moments.

	Deflection [mm]
Without P	32.9
With P	33.7

The current AF length is determined using a scour depth of 3 meters. In order to asses the uncertainty of this assumption, a sensitivity analysis is performed with respect to the effect of scour depth on the influence of AF length. This is done for some governing load cases as visualised in Figure 2.14. One can observe that the influence of scour depth will in the most extreme case (0 vs. 6 m) result in a difference in AF length of around 0.75 meter.

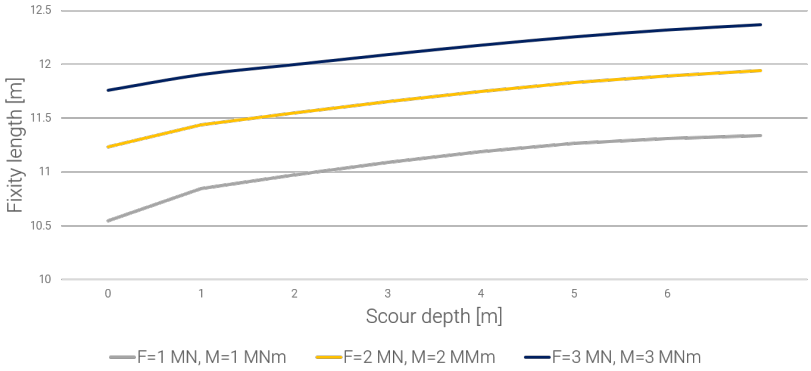

Figure 2.14: Fixity length vs. scour depth.

In order to asses the influence of a 0.75 m change in AF length, another sensitivity analysis is performed varying this parameter. Furthermore, this analysis also quantifies the uncertainty imposed by a fixed AF length for all simulations. The EAC movement are determined for three AF lengths: 11.25, 12 and 12.75 meters. This is done by simulating the full model for each AF length and assessing the EAC movement. Half a period of a relatively large regular wave of H=5 m and T=10 s is used for this simulation. The results are displayed in Figure 2.15. The maximum relative difference is 0.0097 mm which is around 14 % of the total. Although this is relatively little, it might be more significant for higher larger displacements. This should therefore be taken into account when investigating the end results.

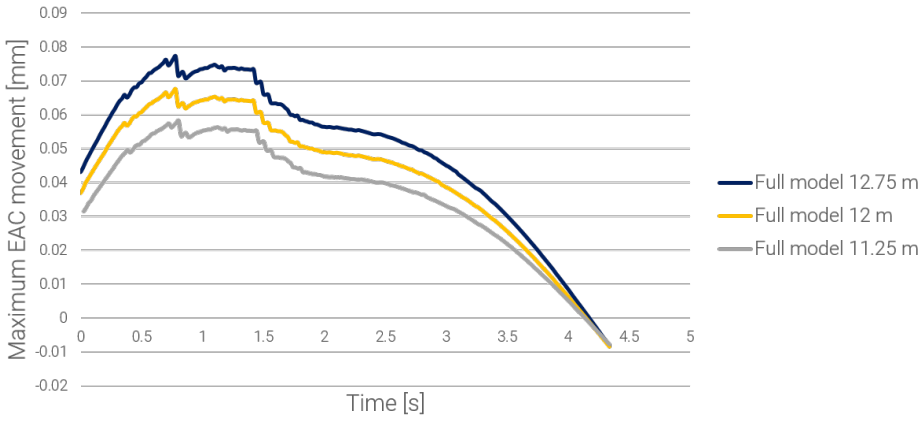

Figure 2.15: Maximum EAC movement for apparent fixity: 11.25, 12 ,12.75 m.

The method of using coupled springs to account for soil-pile interaction will not be used in this research. The method is in essence similar to the AF model [75]. However, this method replaces the pile below seabed for coupled springs. This is in other words a stiffness matrix representation of the interaction between the soil and pile. This approach is not feasible for the detailed model as the geometry of the pile below the seabed is needed to asses the EAC movement in the detailed model.

2.3. Load cases

The load cases that should be used to simulate the grouting operations are described in the *DNVGL-ST-N001 Marine operations and marine warranty* [19].

Within this regulation, a distinction is made between weather restricted and weather unrestricted operations. According to the *DNV GL* [19], weather restricted operations may be planned with design environmental conditions selected independent of statistical data, i.e. set by owner, operator or contractor. For weather unrestricted operations, extreme value statistics should be used in order to determine the environmental conditions.

In order to determine the type of operations, the operational reference period (T_R) [hr] should be defined as shown in Equation 2.9 and visualised in Figure 2.16. Here, T_{POP} [hr] is the planned operational period and T_C [hr] is the contingency time.

$$T_R = T_{POP} + T_C \tag{2.9}$$

The planned operational time (T_{POP}) start after the latest weather forecast is issued and finishes when the jacket is in safe condition. For the grouting procedure, the planned operational time will therefore consist of the grouting preparation/operation and the curing time. Jacket installation will not be included in this time frame as this is designed to be a separate operation. The planned operational period (T_{POP}) for grouting can be summarised as shown in Figure 2.17.

Furthermore, as described in Equation 2.9, a contingency time should be added. The contingency time in general covers the following aspects:

- Uncertainty in the planned operational period.
- Downtime during the operation. This can for example mean solving of unforeseen procedural problems.

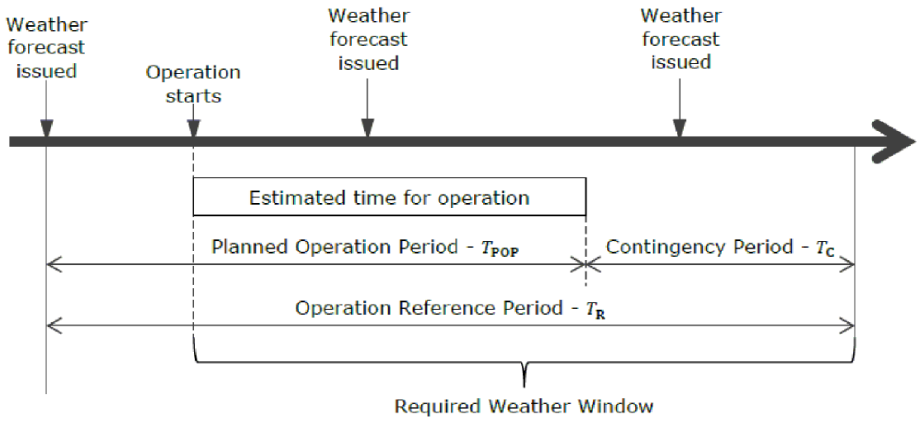

Figure 2.16: DNV operational reference period [19].

- A possible contingency operation.

According to the *DNV GL* [19], a contingency time of 50% can normally be accepted for repetitive operations were T_{POP} has been accurately defined based on experience with the actual operation. when including this, a total operational reference period of 43.5 h is reached as visualised in Figure 2.17. These operational time periods are estimated based on internal information from the Boskalis offshore operation department.

Operation	Time [hr]
Jacket access	1
Grouting prepatation	1
Grout operation	3
Grout curing	24
Planed operation period	29
50% Contingency time	14.5
Operation reference period	43.5

Figure 2.17: Operational reference period grouting operation.

Whenever $T_{POP} < 72$ h and $T_R < 96$ h, the operation can be classified as weather restricted, which is the case for the grouting operation.

As the design condition for a weather restricted operation can be set by the contractor, in this case Boskalis, a sea state will be chosen which will not result in unnecessary downtime. This will result in a design condition which is based on the operational limit of the installation vessel (OP_{LIM}). As a result, the design condition for grout curing cannot be lower than the operational limit of the installation vessel.

However, in order to account for any uncertainties in the weather monitoring and forecasting, a reduction factor is introduced. As shown in Equation 2.10, the actual operational weather forecasted limit (OP_{WF}) is obtained by multiplying the operational limit (OP_{LIM}) with an alpha factor (α).

$$OP_{WF} = \alpha \cdot OP_{LIM} \tag{2.10}$$

The alpha factor (α) can be extracted from the *DNV GL* standard [19] and is dependent on the following factors:

- The sensitivity of the operation.
- The presence of an on site meteorologist.
- The design method: Load and Resistance Factor Design (LRFD) or Allowable Stress Design (ASD) / Working Stress Design (WSD).
- Operational limit (OP_{LIM}).
- Operational reference period (T_{POP}).

A possible installation vessel for grouting operations could be the Bokalift 1. This fairly large vessel would be of interest as it can perform the grouting directly after the jacket installation. However, smaller grout vessels could also be used as they can decrease the operational costs. Table 2.5 shows the alpha factor (α) and the corresponding operational weather forecast limit (OP_{WF}) for two cases. As one can see, the alpha factor for a smaller operational limit is lower as it is more difficult to estimate the wave height for small sea states.

Table 2.5: α factor for two operational cases.

Vessel	Sensitivity class	On site meteo	Design method	OP_{LIM} [m]	T_{POP} [hr]	α [-]	OP_{WF} [m]
Bokalift 1	A1	No	LRFD	3.5	43.5	0.86	3.01
Small ship	A1	No	LRFD	1.5	43.5	0.78	1.17

From the operational limit (OP_{LIM}), a single maximum design wave can be computed which the structure should be able to resist. According to *DNV GL*, this wave can be computed using Equation 2.11. Here, H_s is the operational limit (OP_{LIM}) [m] and STF is the storm factor which can be taken as 2.0 [-].

$$H_{max} = STF \cdot H_s \tag{2.11}$$

The period corresponding to this design wave can be calculated using Equation 2.12. Here, T_{ass} is the period of the single maximum wave.

$$2.55\sqrt{H_{max}} \leq T_{ass} \leq 3.32\sqrt{H_{max}} \tag{2.12}$$

When using Equation 2.11 and Equation 2.12, design conditions for the two cases can be calculated as shown in Table 2.6. As one can see, milder EAC design conditions (H_{max}) are needed when grouting with a small ship. However, the downside of this approach is that this small ship can only start grouting when the forecasted significant wave height is below 1.17 m as shown in Table 2.5. This will significantly reduce the operational weather windows.

Table 2.6: Design conditions for two operation cases.

Vessel	OP_{LIM} [m]	H_{max} [m]	T_{low} [s]	T_{high} [s]
Bokalift 1	3.5	7	6.7	8.8
Small ship	1.5	3	4.4	5.8

In order to fully map the behaviour of the EAC movement for several sea states, a range of design waves and periods will be examined. These design waves (H_{max}) and periods (T_{low}/T_{high})

are based on a range of significant wave heights and determined using Equation 2.11 and Equation 2.12. These design waves represent the extreme wave loads in an irregular sea state. They are displayed in Table 2.7. Furthermore, waves can attack the structure at an angle. As the reference jacket is symmetrical, each design wave will be tested at three angels: 0^o, 30^o and 45^o(Figure 2.18).

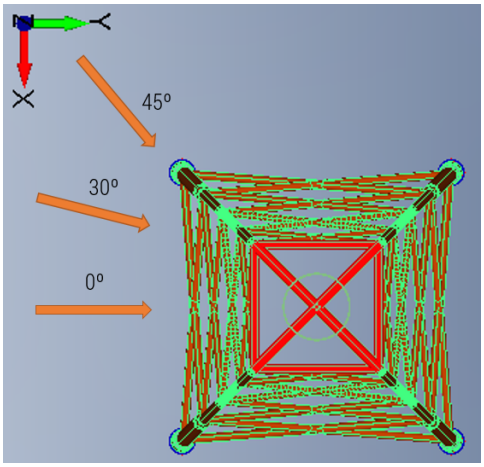

Figure 2.18: Jacket wave directions.

Table 2.7: Load cases for directions 0^o, 30^o and 45^o.

H_s [m]	H_{max} [m]	T_{low} [s]	T_{high} [s]
0.5	1	2.6	3.3
1	2	3.6	4.7
1.5	3	4.4	5.8
2	4	5.1	6.6
2.5	5	5.7	7.4
3	6	6.2	8.1
3.5	7	6.7	8.8
4	8	7.2	9.4
4.5	9	7.7	10.0

The design approach as explained in this section designs for an equivalent largest wave (H_{max}) to replace irregular wave conditions. The factor used in this case is STF=2 [-] and should account for any combination of large waves occurring in an irregular sea state. In order to verify this statement, two cases are simulated with an irregular sea state.

These cases will be compared to the corresponding design cases as summarized in Table 2.8. Both cases represent a sea state with significant wave height of H_s=2 m and respectively a wave period of T_{ass}=5.1 s and T_{ass}=6.6 s. The relation between T_{ass} and T_z can be defined as $1.05T_z < T_{ass} < 1.40T_z$ [26] and the relation between T_z and T_p for a peak enhancement factor of γ=3.3 can be defined as $T_p = 1.286T_z$[19]. This results in a corresponding peak period for the two irregular wave cases of T_p=5.4 s and T_p=6.9 s. The EAC movement of the irregular sea state should not be higher than the movement from the design wave in order to verify that the approach of a design wave is a representative estimate. Both cases will be tested using a dynamic analysis. The length of the irregular simulation will be 600 s and the length of the design wave simulation will be 60 s. A sampling frequency f_s of 25 Hz will be used.

Table 2.8: Irregular sea state and design wave case parameters.

	Case 1		Case 2	
	Irregular sea state	Design wave	Irregular sea state	Design wave
H_s [m]	2	2	2	2
H_{max} [m]	-	4	-	4
T_p [s]	5.4	-	6.9	-
T_{ass} [s]	-	5.1	-	6.6
γ [-]	3.3	-	3.3	-
Wave direction [^{o}]	0	0	0	0
Simulation time [s]	600	60	600	60
f_s [Hz]	25	25	25	25

The emphasis of this research will be on EAV movement induced by wave loading since these are governing according to *DNVGL-ST-0126*[17]. However, in order to quantify the effect of current and wind loads, separate simulations will be run testing these cases. Table 2.9 summarizes the current and wind load cases. A 0.95 m/s current is used since this is the maximum measured value at the Inch Cape site. A wind speed of 12 m/s is used since this is a realistic value of an operational threshold for the Bokalift.

Table 2.9: Load cases for current and wind.

Direction [^{o}]	Current speed [m/s]	Wind speed [m/s]
0	0.95	12
30	0.95	12
45	0.95	12

2.4. Interface conditions

The global jacket model will be analysed for all load cases as displayed in Table 2.7 and Table 2.9. The output of these simulations will be the interface forces at the four lowest joints, close to the seabed.

As visualised in Figure 2.19, these output time series will then be used as an input for the detailed model. The most severe combination of interface forces will be used as an input since this will result in the largest possible EAC movement. The applications of these loads on the detailed model will be further explained in Phase 2.

An important consideration to take into account is the fact that the global jacket model does not take into account any form of rotation or translation between the pile-leg interface. The foundation piles are modelled as beam elements. The interface conditions on the other hand, will be used to model the deflections in the detailed model which does account for rotation and translation between the pile and leg. The two models do therefore not perfectly coincide.

In order to assess the uncertainty imposed by this method, a comparison study is performed. This comparison study also includes the usage of interface deflections/rotations as a reference. The full model, as discussed in subsection 1.4.1 (Figure 1.11) is used as a validation since this model represents reality from an interface point of view. A design wave of height $H = 5$ and period $T = 10$ with direction 0^o is used for this simulation. An AF length of 12 meter is adopted as explained in

subsection 2.2.5. The results can be found in Figure 2.20.

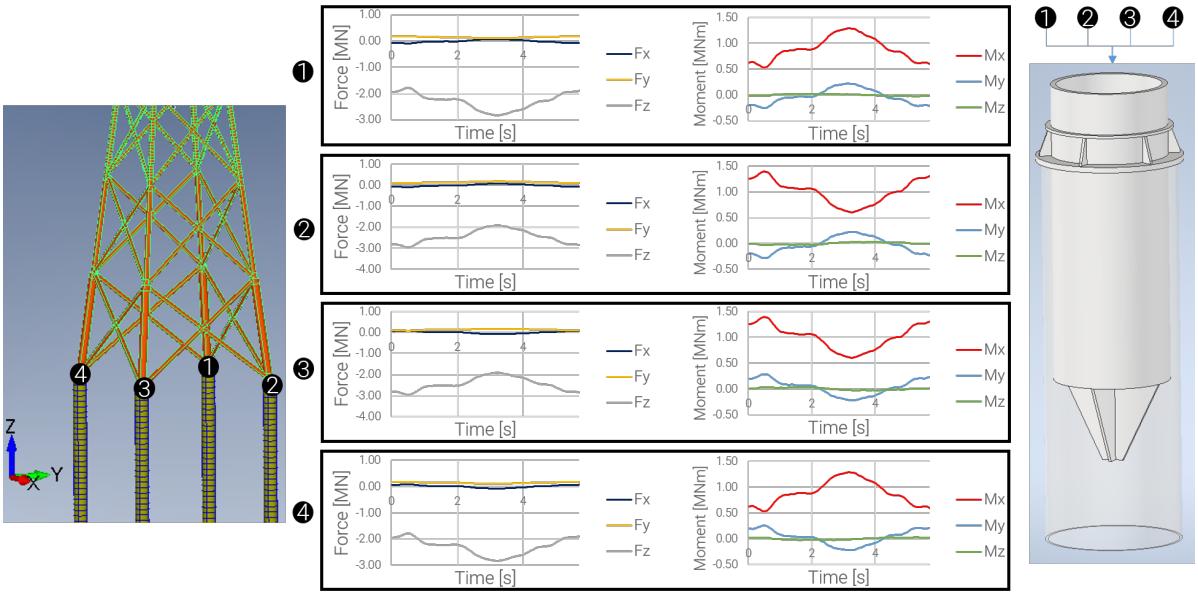

Figure 2.19: Visualisation of using interface forces and moments as input for the detailed model.

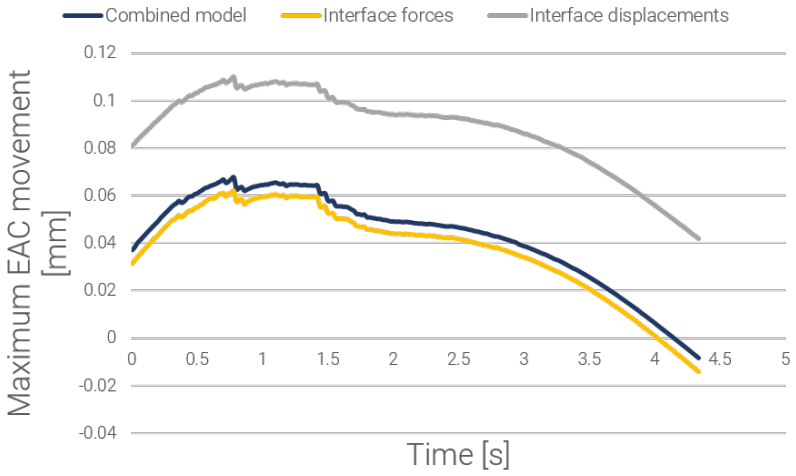

Figure 2.20: Maximum EAC movement for full model and interface conditions.

As can be seen from Figure 2.20, the EAC movement when using interface forces are slightly lower compared to the full model. However, the movement when using interface displacements largely over predict the EAC movement. The usage of interface forces is therefore a conservative estimate for the determination of EAC movement.

2.5. Discussion

The objective of Phase 1 is to define a solid basis for the detailed analysis that will follow in this report. This includes setting the scope for this project and making the necessary assumptions to obtain a feasible research. All improvements that can be made by widening the scope of the study will be discussed in the recommendations of chapter 5. The limitations induced by the assumptions made will be discussed in this section.

The hydrodynamic loads are determined using a 2D Morison equation with 3^{rd} order Stokes waves. In this equation, the lift force is neglected since this force is generally small [44]. However, this force might introduce a force component perpendicular to the wave direction which could influence the EAC movement. Investigating the effect of this force component on the influence of the interface forces should therefore be done.

The soil-pile interaction is linearized using an AF model. The resulting AF length is conservatively estimated in order to not under predict the movement and is used for all simulations. A scour depth of 3 meters is assumed for this analysis. However, the accuracy of this approach could be improved in several ways dependent on the overall precision. First of all, the AF length could be varied per load case or range of load cases in order to better capture the nonlinear behaviour of the soil. Furthermore, the actual scour depth could be assessed more precisely based on the soil parameters. Since the top soil layers consist of cohesive clay, the effect of scour might be limited. Furthermore, a full p-y model could be used to model the global and detailed model. This will fully capture the non-linearity of the soil and therefore yield more accurate results. This would also facilitate the option to include T-z curves in the model. This would capture the behaviour of the pile under axial force better and improve the accuracy of the results.

The modelling approach described in phase 1 uses two models in order to split up the simulations to decrease computation time. The interface forces which are determined using the global model do not take into account any relative deflections and rotations in the interface connection. The error induced by this method is relatively small whenever the deflections and rotations in the detailed model are small. However, higher accuracy would be reached when simulating the full model, consisting of the jacket including all foundation piles with a friction connection. This could be done for some governing cases in order to verify the results of the splitted models. If more computational power can be obtained, all simulations should be performed using the full model.

3

Phase 2: Reference model

The main objective of phase 2 is to set up a detailed reference model in order to quantify the EAC movements for the load cases as defined in phase 1. Furthermore, the objective is to gain insight into the behaviour of EAC movement for various loading conditions. Phase 2 is divided into three sub phases as visualised in Figure 3.1.

First of all, the pile-leg interface will be further examined as this plays a crucial role in the EAC movement and this research. The foundation pile and jacket leg with reference stopper will then be modelled in detail. Using the interface forces from the global model, the EAC movement in the reference model can be simulated. These results will be discussed and can be used as a comparison for the rest of this study.

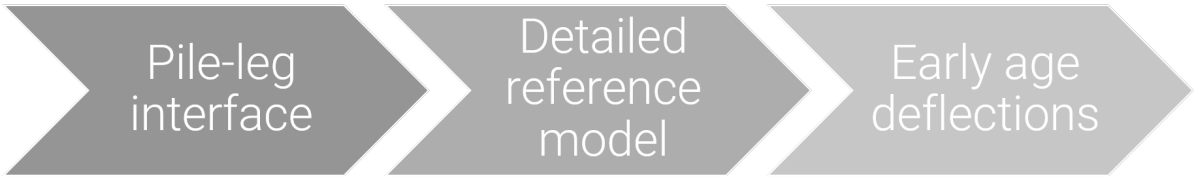

Figure 3.1: Overview phase 2.

3.1. Pile-leg interface

The design of the pile-leg interface, including stopper, is project specific and dependent on various parameters. This section will discuss the general geometry of the foundation pile and jacket leg which is based on the Inch Cape project. Furthermore, the main considerations are discussed in order to determine the overall stopper design.

3.1.1. General dimensions pile-leg model

The general dimensions of the pile-leg model are displayed in Table 3.1. These dimensions are determined based on ULS and FLS analysis as described in the *"DNVGL-ST-0126"* [17]. For this research, the general dimensions are calculated based on Inch Cape data and are set as fixed to limit the scope. Figure 3.2 shows the general pile-leg dimensions. As can be seen, the jacket leg is equipped with centralizers in order to simplify the alignment with the foundation pile. The jacket leg will, after set-down, rest on the pile stopper which is indicated by the green dotted square in

Figure 3.2. The actual design of the pile stopper is more complicated and is the effect of a trade off taking into account various counteracting effects. Since pile stopper design significantly influences the EAC movement, this will be further investigated in this research.

Table 3.1: General dimensions pile-leg model.

Geometry		
Outer diameter pile	2500	mm
Outer diameter jacket leg	2134	mm
Connection length	4000	mm
Width grout annulus	133	mm
Wall thickness pile	50	mm
Wall thickness jacket leg	100	mm
Number of effective shear keys	9	-

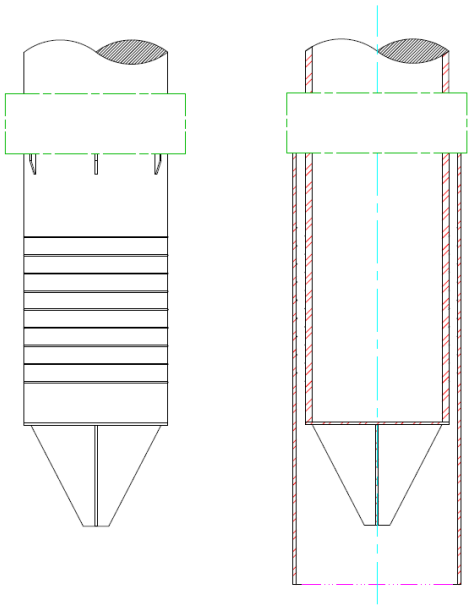

Figure 3.2: General pile-leg geometry without stopper.

3.1.2. Pile stopper

A pile stopper should be designed in order to meet several project requirements. The most important requirements will be briefly discissed:

- Limit the EAC movement.
- Create on-bottom stability to prevent sliding or overturning of the jacket.
- Limit the load transfer from pile to leg during the design life of the jacket to reduce fatigue around the stopper. The main load transfer should go through the grout.
- Adjust for installation pile misalignment or fabrication tolerances.
- Coop with the impact loads during set-down of the jacket on the piles.

Early age cycling movements
The main considerations in this research is limiting the EAC movement. This movement is limited to an absolute maximum of 1 mm and require a stiff pile stopper with a large frictional contact area.

On-bottom stability
On bottom stability can be characterised as:

- Leg uplift
- Global sliding
- Single leg sliding

Due to the self weight of the jacket, leg uplift is only likely to occur at large sea states. The largest issue in this case is single leg sliding which can occur as a result of limited contact area between the pile and leg [1].

Fatigue at stopper
Whenever the stopper connection is stiffer than the actual grout connection, cyclic loads will be transferred trough the stopper to the jacket leg. This can cause fatigue in the primary steel of the jacket which is not accounted for in the design life time of the structure. The main problem is therefore not the stopper failing but the damage to the primary steel of the jacket leg. Decreasing the stiffness of the stopper or removing it can resolve this problem.

Adjust for pile misalignment
The pile stopper will not perfectly coincide with the foundation pile if there is no active adjustment of the stopper height. In general, the survey height tolerance between foundation piles can be roughly +/- 50 mm. Furthermore, a pile inclination of +/- 0.5 ^{o} can be expected as a maximum. As a result, the active height adjustment of the pile stopper should range +/- 350 mm. This adjustment can be achieved by using for example cylinders or shimming plates.

Impact loads
During set-down of the jacket on the foundation pile, impact loads will be present. These impact loads are dependent on the stiffness of the connections, the mass of the jacket and the impact velocity. The impact velocity is influenced by the heave motion of the installation vessel. Whenever a high installation workability is expected, larger heave motions are present resulting in higher impact loads. Designing a stiff stopper connection might result in plastic deformation during set-down. Decreasing the stiffness or using cylinders to damp the impact are solutions used in projects nowadays.

The relative impact of each of the above mentioned requirements is site and project specific. Furthermore, decreasing the contribution of a specific requirement might lead to an increase of another. Increasing the contact surface to decrease EAC movement might lead to a stiffer stopper and therefore larger fatigue and impact loads. Carefully considering this design and weighing off each factor is therefore vital. As a result of this challenging trade off, varying stoppers have been used in projects over the years. As it tends to be difficult to meet all criteria using only a stopper, special pile grippers entered the market. These pile grippers are mostly external brackets in order to meet all criteria in a redundant way.

A commonly used example is the IHC pile gripper as visualised in Figure 3.3 ([29][30]). This pile gripper is welded to the jacket leg during fabrication. After set-down, it lifts the jacket from the foundation pile and aligns it using vertical cylinders. It then clamps the foundation pile sideways to rigidly fix the connection during grout curing. After curing, it retrieves the cylinders. Therefore,

it limits EAC, creates on-bottom stability, reduces load transfer from leg to pile, and adjusts for pile misalignment's. However, it is a costly extra and needs to be permanently installed on each jacket leg.

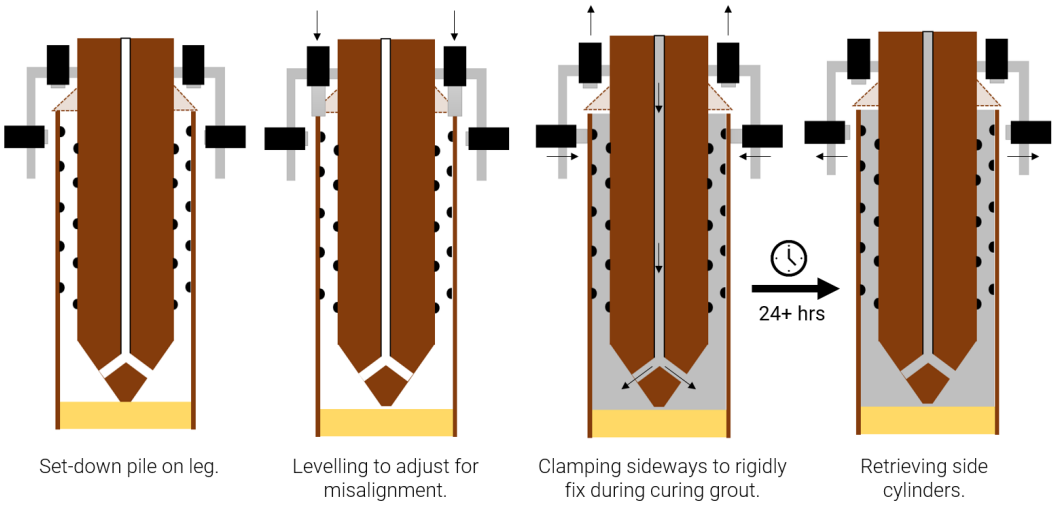

Figure 3.3: Schematic visualisation IHC pile gripper.

The amount of permanently or temporary pile grippers on the market is significant. However, these mitigation measures tend to be expensive while their effect on EAC movement is a debated issue. The scope of this research is focused on minimizing the EAC movement. Assessing the actual magnitude of this movement without mitigation measures is therefore vital. The reference model which will be used therefore includes a stopper which is modelled as a full circular flange connection with a perfect alignment to the foundation pile as visualised in Figure 3.4. A conservative friction coefficient of 0.2 [-] is assumed which will be further discussed in section 3.2. A detailed drawing of the reference stopper is displayed in Appendix E.

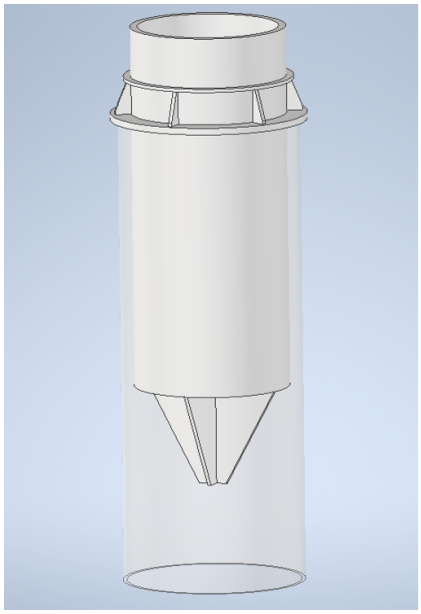

Figure 3.4: Reference model with flange stopper.

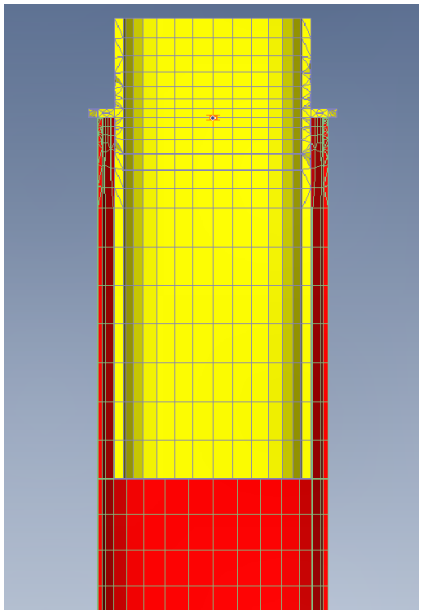

Figure 3.5: Cross section of reference model with flange stopper meshed in Femap.

3.2. Detailed reference model

The reference model is based on the geometry of Table 3.1 and includes a perfectly smooth, thick flange stopper connection. A large thickness is chosen to increase the stiffness and prevent deformation when subjected to large normal forces. As a result, an almost perfect contact surface is obtained for all simulations. In order to fully map the behaviour of the frictional flange connection, solid elements are used for the Femap model. All unnecessary geometrical features which do not contribute towards the stiffness of the connection, like the lower centralizer, are removed from the model.

3.2.1. Friction connection

The friction connection is modelled in Femap using a linear contact analysis [36] which behaves the same as a fully a non-linear contact analysis. However, the assumption made here is linear material behaviour and small displacements and rotations. In order to perform a contact analysis, a target and source regions needs to be assigned in between which contact elements are created during the analysis. Normal vectors are projected from the source region towards the target region. When the length of this vector is within the pre-defined search distance, a contact element is created [65]. This step is repeated for every contact iteration within a load case. Therefore, the amount of contact elements created will change depending on the relative change of the contact regions due to friction.

In order to increase the amount of contact elements formed, the source region should contain a fine mesh. As illustrated in Figure 3.6, swapping the source region from one element (A) to 4 elements (C) results in an increased number of contact elements and therefore accuracy. A more in-depth explanation regarding the contact analysis can be found in Appendix F.

Figure 3.6: Contact elements for source region (A,C) and contact region (B,D) [36].

Within the linear contact analysis, a static friction coefficient ($\mu_s[-]$) is used. Since this solution is valid for small displacements, no dynamic friction ($\mu_d[-]$) is incorporated. This analysis is therefore valid in order to check whether the interface "sticks" or "slips" [20]. In order to predict the behaviour after slipping, an advanced non-linear analysis should be performed. One can assume that when slippage occurs, the relative EAC threshold of 1 mm will be exceeded. For this research, simulating the behaviour after slipping would be too time consuming with respect to the gained knowledge. However, when assessing a specific stopper for a detailed design, performing an advanced non-linear analysis would be a recommendation.

For the current analysis, a static friction coefficient is needed. Determining the static coefficient of friction for a a dry steel surface is relatively accurate if the surface roughness and type of machining is known [35]. However, in the case of the pile-leg interface, water is present in the contact surfaces acting as a lubricant.

The presence of a layer of lubricant molecules between two contact surfaces is called boundary lubrication. According to Lyons et all. [54], boundary lubrication exists due to peaks in surface roughness, also referred to as asperities. The presence of asperities is unavoidable, regardless the amount of material finishing. The lubricant enters the space between the asperities forming a boundary

film. The amount of contact pressure, viscosity of the fluid and speed determines the lubrication regime and therefore the contact between asperities. This at its turn influences the friction of the connection. The first regime characterises the friction without relative movement as can be seen in Table 3.2. This regime behaves different dependent on the amount of contact pressure.

Table 3.2: Regimes of lubrication [22].

	Conformal contacts: low contact pressure	**Nonconformal contacts: high contact pressure**
Regime I (static)	Boundary lubrication	Extreme pressure (EP) lubrication

Dependent on the amount of pressure on the contact, the lubrication regime will behave differently. A low pressure film usually has a mean pressure between 10^5 Pa and 10^7 Pa whereas a high pressure film ranges from $2 \cdot 10^8$ Pa and $3 \cdot 10^9$ Pa. The contact pressure on the Inch Cape jacket can be roughly estimated in order to determine the pressure regime. The maximum frictional contact area consists of the cross sectional surfaces of the four foundation piles. Each pile has a thickness of 50 mm and a radius of 1250 mm. This results in a cross sectional area of 0.46 m^2 per pile thus resulting in a total surface of 1.84 m^2. The maximum jacket weight of a small cluster jacket is 1200 tons. This results in a total surface pressure of $6.39 \cdot 10^6$ Pa. This amount of pressure would result in a low pressure film. However, due to environmental loading the pressure will vary in time and might also reach the high pressure regime. According to work done by Pijers et al. [61], a decrease in friction can be observed for increased contact pressure. The magnitude of increased contact pressure should be further investigated when simulating the environmental loads on the jacket structure. For now, a low pressure film is assumed.

The first regime, associated with zero or limited relative velocity, is boundary lubrication. In this regime, the friction is mainly dependent on the surface properties, contact pressure and the properties of the fluid. According to Frene et all. [22], viscosity of the fluid does not influence the friction. As the surface finishing and contact pressure largely influences the friction, the coefficient can change per jacket and over time. In general, steel to steel friction coefficients in offshore environments range between 0.15 [-] and 0.3 [-] ([12][68][2]). As there will be some rust formation on the stopper, since it is not coated, a relatively conservative estimate in this case is 0.2 [-].

3.2.2. Mesh convergence study

The element types used to mesh the reference model are the six sided CHEXA elements, the four sided CTETRA elements and the five sided CPYRAM elements. The preferred element type for this model is the six sided CHEXA elements since this yields the most accurate results ([64] [4]). Around the frictional interface, a refined mesh is needed in order to improve the accuracy of the contact iterations. This refined mesh is not necessary along the length of the pile since this will increase the computational time without gaining a more accurate result. The transition towards a smaller mesh in the flange area is meshed using CTETRA and CPYRAM elements. Due to limitations in the Femap meshing toolbox, modelling the flange with only CHEXA elements can not be achieved.

For all elements, the option can be used to incorporate midside nodes. Elements without midside nodes tend to underpredict the deflections and stresses due to their linear interpolation. Furthermore, shear locking might occur in the elements [55]. Changing to a higher order interpolation method by including midside nodes might increase the accuracy of the deflections and stresses [77].

In order to obtain an optimal mesh distribution, a mesh convergence study is performed. Three

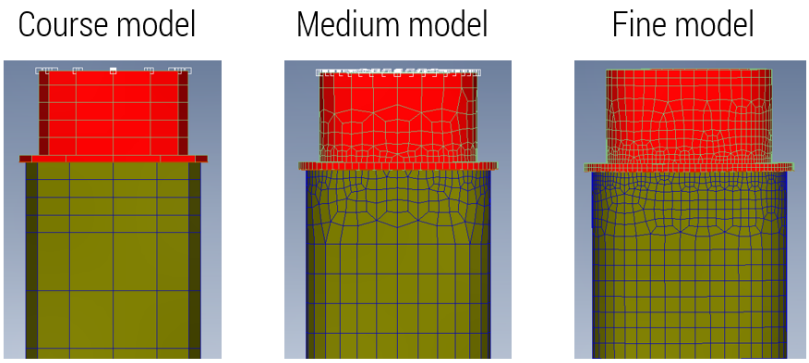

Figure 3.7: Mesh convergence study.

models are tested as displayed in Figure 3.7 ranging in element density. Furthermore, each model is tested with and without midside nodes as can be seen in Table 3.3. The transition from a course mesh to finer mesh within a model can not be done using CHEXA elements since this is limited by the FEMAP meshing toolbox.

Table 3.3: Mesh convergence models.

Model	**Simulation number**	**N of nodes**	**N of elements**
Course	1	1153	1832
Course	2	4747	1844
Medium	3	6609	14232
Medium	4	16425	14316
Fine	5	29908	32431
Fine	6	73331	32455

All models have been tested using a nodal top load of 100 kN. Figure 3.8 shows the maximum deflections of the models, which occurs at the top center node. Furthermore, Figure 3.9 shows the computational time for each simulation. Each even simulation number (2,4,6) represents a model with midside nodes. As can be seen in Figure 3.8, models without midside nodes underpredict the deflections compared to the same models with midside nodes. However, computational time is also lower without midside nodes. The deflections converge at the medium model and do not differ significantly towards the fine model. Although the computational time is relatively low for all models, each load case will be iterated multiple times if friction is taken into account. Furthermore, a significant amount of time steps is simulated for all load cases. Therefore, reducing the simulation time without decreasing the accuracy is beneficial in this case. Therefore, the medium model will be used with midside nodes.

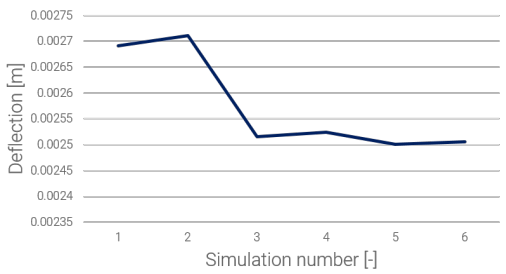

Figure 3.8: Maximum deflections vs. simulation number.

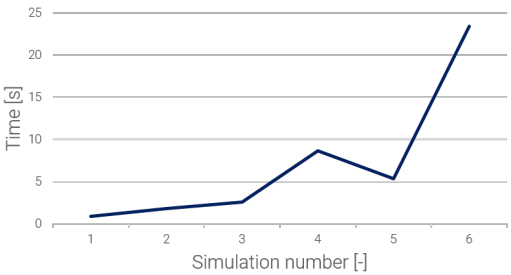

Figure 3.9: Computational time vs. simulation number.

3.2.3. Interface forces

As described in chapter 2, the reference model will be analysed using interface forces extracted from the global model. These interface forces are obtained at 4 nodes that geometrically coincide with the top of the reference model. As explained in section 2.3, the global jacket loads will be simulated using an equivalent design wave to account for an irregular sea state. In order to verify whether the usage of a design wave does not underpredict the EAC movement compared to an irregular sea state, two irregular cases will be tested. For each case, a simulation will be run using respectively a number of design waves and an irregular sea state. The parameters for these cases are given in Table 2.8. Case 1 simulates a significant wave height of H_s=2 m and a small period of T_p=5.4 s and case 2 simulates a significant wave height of H_s=2 m and a large period of T_p=6.9 s. The forces in y-direction for case 1 are displayed in Figure 3.10 and Figure 3.11. These time series represent the steady state part of the response. Both analysis are simulated dynamically. For the dynamic simulation, a structural damping coefficient of 1% is taken as this is a conservative estimate for commonly used jacket simulations [37]. Since the energy within the design wave does not represent a spectrum which is excited by the first natural frequency, no real dynamic effects are visible for this case. Some small oscillations within this response could be the effect of the initial transient response, a result of the simulation or an effect of the nodal point loads changing in magnitude. This same effect is visible when closer examining the irregular sea state. The load characteristics for all forces and moments for case 1 are displayed in Table 3.4 and Table 3.5.

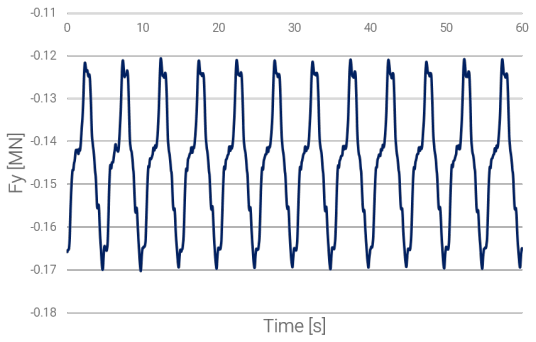

Figure 3.10: F_y component for multiple design waves H_{max}=4 m, T_{ass}=5.1 s.

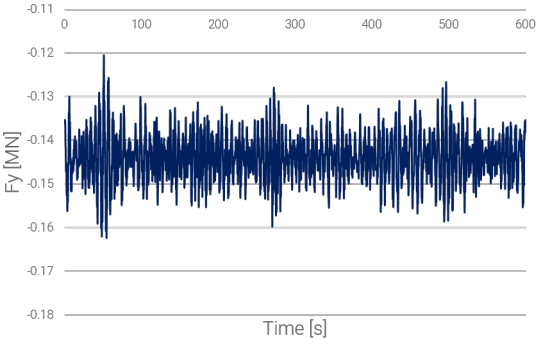

Figure 3.11: F_y component for irregular wave H_s=2 m, T_p=5.4 s.

When comparing the load characteristics for the design wave and the irregular sea state, some interesting observations can be made. In general, the mean loading that coincides with the wave direction (Fy,Mx) are of same magnitude for both analysis. The extremes of the design wave are slightly higher compared to the irregular sea state. This is in line with expectations since the most probable maximum wave height (H_{max}) can in general be estimated using Equation 3.1 [58]. The design wave which is adopted in this study is determined as $H_{max} = 2H_s$ as recommended in *DNVGL-ST-N001* [19]. Using this design wave will therefore most likely result in an over prediction of wave loading.

$$H_{max} = 1.86 H_s \tag{3.1}$$

The standard deviation of the irregular sea state is much lower compared to the design wave. This is in line with expectations since the amount of small scale fluctuations is much higher for the irregular sea state. However, the maximum values are of importance for both analysis as they result in the largest EAC movement. These values will therefore be used to simulate the maximum EAC movement.

Table 3.4: Design wave (H_{max}=4 m, T_{ass}=5.1 s) and irregular sea state (H_s=2 m, T_p=5.4 s) force characteristics. DW denotes 'Design Wave' and ISS denotes 'Irregular Sea State'.

	DW Fx [MN]	ISS Fx [MN]	DW Fy [MN]	ISS Fy [MN]	DW Fz [MN]	ISS Fz [MN]
Mean	0.0042	0.0001	-0.1454	-0.1439	2.3409	2.3739
Min	-0.0438	-0.0417	-0.1703	-0.1624	2.0444	2.1827
Max	0.0519	0.0336	-0.1206	-0.1205	2.6631	2.6120
Std	0.0291	0.0097	0.0143	0.0051	0.1904	0.0594

Table 3.5: Design wave (H_{max}=4 m, T_{ass}=5.1 s) and irregular sea state (H_s=2 m, T_p=5.4 s) moment characteristics. DW denotes 'Design Wave' and ISS denotes 'Irregular Sea State'.

	DW Mx [MN]	ISS Mx [MN]	DW My [MN]	ISS My [MN]	DW Mz [MN]	ISS Mz [MN]
Mean	-0.9298	-0.9502	0.0119	0.0004	0.0010	0.0001
Min	-1.1548	-1.1445	-0.1329	-0.1266	-0.0187	-0.0208
Max	-0.7080	-0.8011	0.1520	0.0975	0.0195	0.0177
Std	0.1344	0.0446	0.0837	0.0286	0.0116	0.0044

Figure 3.12 and Figure 3.13 show the maximum EAC movement for the design wave and irregular sea state of case 1 and case 2. As can be observed, the EAC movement for an irregular sea state does not exceed the movement of the design wave. When examining the results of case 1, no significant difference can be noted. This is in line with observations made in Table 3.4 and Table 3.5 showing no large difference in extreme values between the design wave and the irregular sea state. For case 2, the design wave is a conservative estimate to predict movement from an irregular sea state. The conclusion which can be drawn from this test is that the design wave method does not under predict the EAC movement when compared to an irregular sea state. This assumption will therefore be used throughout the report.

Directions: 0° Design wave

H_s [m]	H_{max} [m]	T_{ass}[s]	EAC [mm] (Case 1)	Thigh [s]	EAC [mm] (Case 2)
2	4	5.1	0.279	6.64	0.331

Figure 3.12: Maximum absolute EAC movement for a design wave at H_{max}=4 m.

Directions: 0° Irregular sea state

H_s [m]	γ [-]	T_p[s]	EAC [mm] (Case 1)	Tp [s]	EAC [mm] (Case 2)
2	3.3	5.4	0.277	6.9	0.290

Figure 3.13: Maximum absolute EAC movement for an irregular sea state at H_s=2 m.

3.3. Early age cycling movements

As discussed in subsection 3.2.3, the usage of a design wave is a conservative estimate to replace an irregular sea state. The response of the reference model will therefore be analysed using the interface forces as explained in section 2.3. For each load case, the input forces resulting in the largest EAC movement are chosen. This is in general determined by examining the magnitude of forces and moments. The interface forces are applied at the top of the model using a rigid spider element, connected to the top nodes. The distance between the spider element and the start of the stopper interface is 1.3 meter in order to provide enough distance for the stress to distribute evenly over the jacket leg. This section provides the results for the EAC movements for wave loads, current loads and wind loads.

3.3.1. Wave load

The maximum absolute EAC movement for all load cases is displayed in Figure 3.14, Figure 3.15 and Figure 3.16. These results represent the absolute maximum movements measured in one wave period. One can observe that the magnitude of movements is relatively small. According to *DNVGL-ST-0126* [17], the maximum relative movements should not exceed 1 mm. When observing Figure 3.14, Figure 3.15 and Figure 3.16, this is the case for all load cases, whenever sliding does not occur. However, some interesting observations can be made which will be discussed.

Directions: 0°

H_s [m]	H_{max} [m]	T_{low}[s]	EAC [mm]	T_{high}[s]	EAC [mm]
0.5	1	2.55	0.223	3.32	0.232
1	2	3.61	0.239	4.7	0.249
1.5	3	4.42	0.238	5.75	0.292
2	4	5.1	0.279	6.64	0.331
2.5	5	5.7	0.399	7.42	0.396
3	6	6.25	0.501	8.13	0.473
3.5	7	6.75	Sliding	8.78	Sliding
4	8	7.21	Sliding	9.39	Sliding
4.5	9	7.65	Sliding	9.96	Sliding

Figure 3.14: Maximum absolute EAC movement 0^o.

Directions: 30°

H_s [m]	H_{max} [m]	T_{low}[s]	EAC [mm]	T_{high}[s]	EAC [mm]
0.5	1	2.55	0.224	3.32	0.228
1	2	3.61	0.227	4.7	0.241
1.5	3	4.42	0.276	5.75	0.286
2	4	5.1	0.281	6.64	0.319
2.5	5	5.7	0.318	7.42	0.369
3	6	6.25	0.395	8.13	0.398
3.5	7	6.75	0.427	8.78	0.435
4	8	7.21	Sliding	9.39	Sliding
4.5	9	7.65	Sliding	9.96	Sliding

Figure 3.15: Maximum absolute EAC movement 30^o.

Directions: 45°

H_s [m]	H_{max} [m]	T_{low}[s]	EAC [mm]	T_{high}[s]	EAC [mm]
0.5	1	2.55	0.221	3.32	0.226
1	2	3.61	0.227	4.7	0.250
1.5	3	4.42	0.248	5.75	0.313
2	4	5.1	0.271	6.64	0.319
2.5	5	5.7	0.302	7.42	0.419
3	6	6.25	0.445	8.13	0.410
3.5	7	6.75	0.397	8.78	0.451
4	8	7.21	Sliding	9.39	0.517
4.5	9	7.65	Sliding	9.96	Sliding

Figure 3.16: Maximum absolute EAC movement 45^o.

Location of largest early age cycling movement

The movements displayed in Figure 3.14, Figure 3.15 and Figure 3.16 are the absolute value of the largest relative movement between the outer shell of the jacket leg and the inner shell of the foundation pile. This movement is measured in vertical and horizontal direction but is governing in horizontal direction. The largest movement can, for limited sliding, always be measured at the bottom of the foundation pile since this point is located furthest away from the pivot point in at the stopper. This is visualised in Figure 3.17 where a scaled deformation of the jacket leg and pile is dis-

played. However, since the model moves in a 3D space, the location of the largest movement could by anywhere on the circumference of the pile and leg.

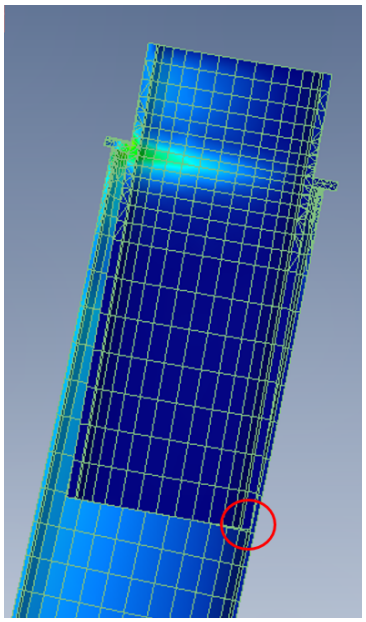

Figure 3.17: Horizontal location of maximum EAC movement (scale factor 15).

Figure 3.18 (Top left) shows the EAC movement around the circumference of the pile. This is measured as the the relative difference between the jacket leg (yellow) and the foundation pile (red). The angles displayed in this graph correspond with the reference frame around the foundation pile visualising the magnitude of EAC movement with respect to the wave angle. As can be noted, the EAC movement tends to be largest within the direction of the incoming wave (180^0 and 0^0). However, the maximum EAC movement for this load case occurs at 154^0 which is a deviation of $26\ ^0$ with respect to the incoming wave direction. The corresponding EAC movement versus time for this point is displayed in Figure 3.18 (Bottom left). This maximum absolute movement within this period is 0.473 mm.

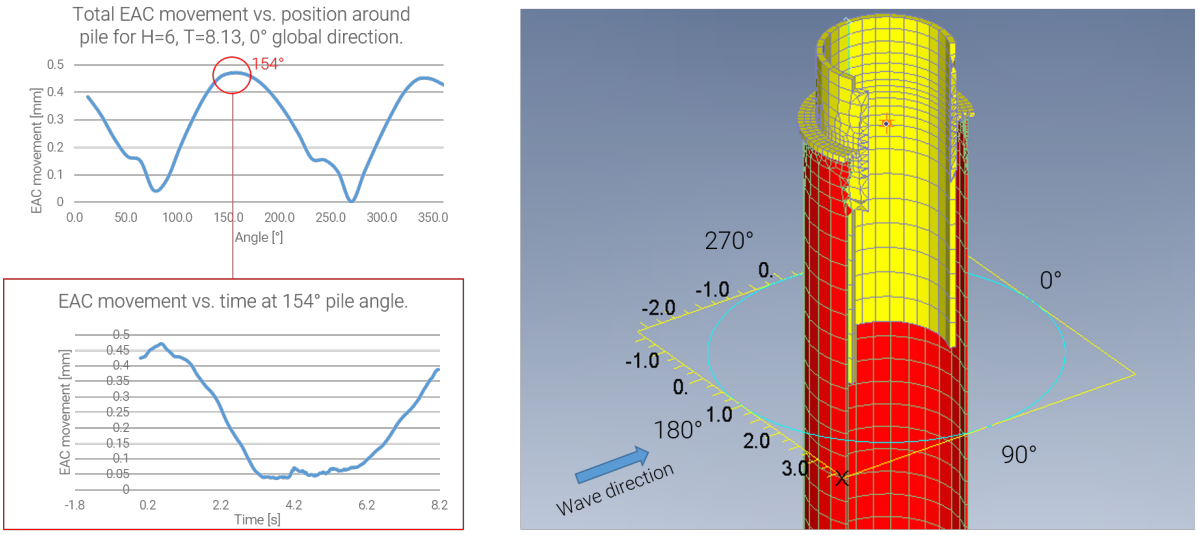

Figure 3.18: Analysis of EAC movement for H_{max} = 6 m, T = 8.13 s and incoming global wave direction of $0\ ^0$.

Table 3.6 shows the direction of the largest EAC movement with respect to the incoming wave angle for all load cases. As can be observed, the largest EAC movement for lower waves occur in line with the wave direction. From H_{max}=4 m, a deviation is visible for 0^0 incoming wave angle. From H_{max}=6 m, a deviation is visible for 30^0 wave angle. This can be explained by the fact that at higher wave forces, the relative contribution of a horizontal force component perpendicular to the incoming wave angle increases. This force component is not a result of lift force in the Morison equation since this is neglected in the simulations as discussed in subsection 2.2.2. The horizontal force perpendicular to the wave angle is a resultant component induced by the inclination of the structure. The self weight of the jacket in combinations with wave loading induces a compressive force in the jacket leg. Due to the inclined orientation of the leg, a horizontal and vertical reaction force is needed to create equilibrium. This is visualised in Figure 3.19, showing the 2D force components for a structure with a batter angle. For larger wave loads, the compressive member force increases inducing a larger horizontal resultant force. As a result, the jacket leg moves out of line with the wave direction. As a result, a deviation of the EAC movement away from the wave direction is visible as displayed in Table 3.6. Note that these values display the absolute deviation and can therefore also be negative. Similar as the horizontal force component, moments are also induced by the wave loading. For the reference stopper, the stresses induced by these moments are uniformly distributed in the jacket leg therefore only inducing some bending. For a modified stopper, these moments can result in rotation of the stopper. This will be further discussed in chapter 4.

Table 3.6: Absolute deviation of largest EAC movement with respect to the incoming wave angle. S denotes 'Sliding'.

H_s [m]	H_{max} [m]	T_{low} [s]	Absolute deviation [^{o}]			T_{high} [s]	Absolute deviation [^{o}]		
			0^o	30^o	45^o		0^o	30^o	45^o
0.5	1	2.55	0	0	0	3.32	0	0	0
1	2	3.61	0	0	0	4.7	0	0	0
1.5	3	4.42	0	0	0	5.75	13	0	0
2	4	5.1	13	0	0	6.64	13	0	0
2.5	5	5.7	13	0	0	7.42	13	13	0
3	6	6.25	13	13	0	8.13	26	13	0
3.5	7	6.75	S	13	0	8.78	S	13	0
4	8	7.21	S	S	S	9.39	S	S	0
4.5	9	7.65	S	S	S	9.96	S	S	S

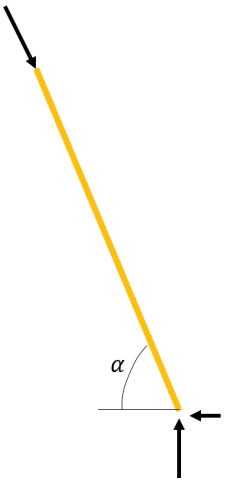

Figure 3.19: Horizontal force component due to inclination of the structure. α is the batter angle.

At 45^o wave angle, no deviation of EAC movement with respect to the wave angle is visible when observing Table 3.6. This can be justified by the fact that one of the foundation piles within the diagonal of the wave direction is examined. For this foundation pile, the force induced by the batter angle has moved in line with the wave direction. Therefore, no significant force component perpendicular to the wave angle can be observed. This phenomenon is also present for the 30^o wave angle and explains why the deviations occur at higher waves.

Magnitude of early age cycling movement

When observing the results for all load cases, as displayed in Figure 3.14, Figure 3.15 and Figure 3.16, one can conclude that the EAC movements are generally small. An explanation for this is the fact that limited rotation and no translation occurs in the interface of the reference stopper. The hydrodynamic loads are distributed evenly over the stopper resulting in limited deformation. This can be seen in Figure 3.20, showing the von Mises stress in the reference model. The maximum stress concentration is around 45 Mpa which is well within elastic limits when looking at the material properties of S355 Steel (Table 2.3). As a result, limited elastic strain is present in the elements therefore decreasing the total deformation and EAC movement.

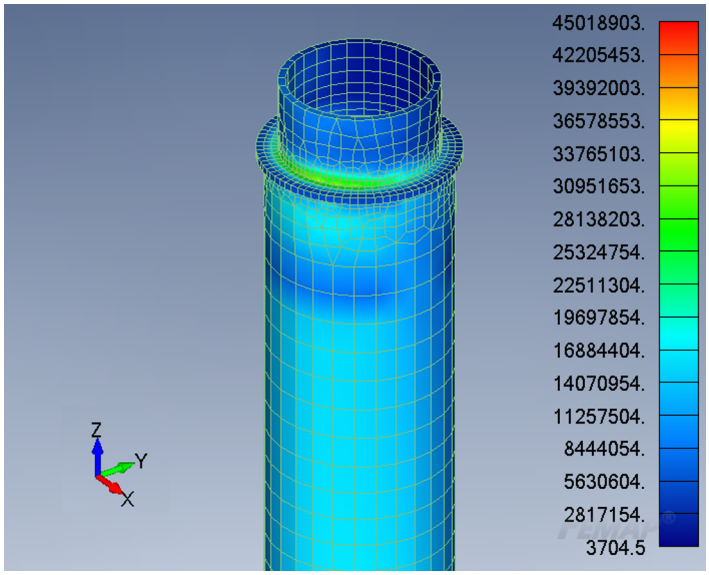

Figure 3.20: Von Mises stress in the reference stopper at H_{max} = 6 m, T = 8.13 s and incoming global wave direction of 0^0.

Directional difference between movements

Table 3.7 shows the mean EAC movement for low and high period waves within the maximum range of which data is available for all directions. As can be noted, the largest mean EAC movement occurs when the waves attack the structure perpendicular (0^0) and decrease for larger wave angles. This effect can be justified by a decrease in Morison loads for waves at an angle. When observing the Morison equation in Equation 3.2, Equation 3.3 and Equation 3.4, one can observe that for varying wave angles, the local normal particle kinematics ($v_N, \dot{v_N}$) and global area A change. Figure 3.21 visualises this phenomenon for a 0^o and 45^o wave. For a 45^o wave, a global area increase of $\sqrt{2}$ can be noted. However, the local normal particle kinematics decrease with a factor of sin(45) ≈0.71. Since the particle velocity is quadratically present in the drag term of the Morison equation, this effect is governing.

Table 3.7: Mean EAC movement for 1 m ≥ H_{max} ≤ 6 m.

Wave direction [^{0}]	Mean EAC T_{low} [mm]	Mean EAC T_{high} [mm]
0	0.313	0.329
30	0.286	0.323
45	0.287	0.307

$$f_{\text{hydro}} = f_{\text{drag}} + f_{\text{inertia}} \tag{3.2}$$

$$f_{\text{drag}} = \frac{1}{2}\rho C_D A v_N |v_N| \tag{3.3}$$

$$f_{\text{inertia}} = \rho(C_M) A \dot{v_N} \tag{3.4}$$

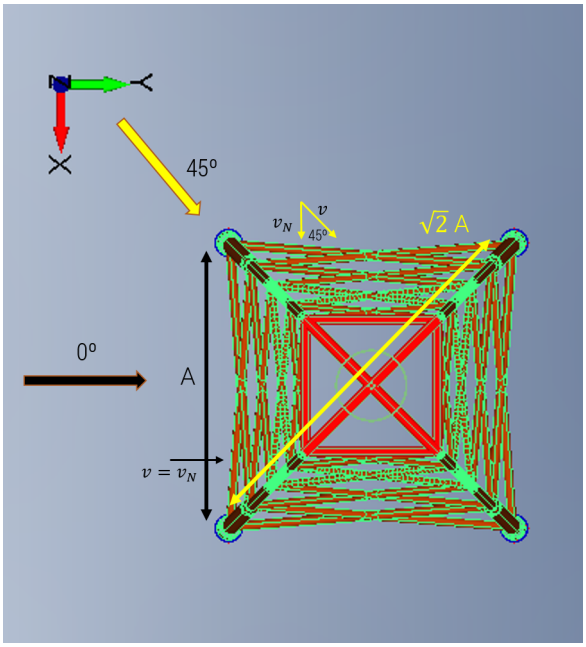

Figure 3.21: Difference in global area and local wave kinematics for 0^o and 45^o incoming wave angle.

Furthermore, as visualised in Figure 3.22 (right), Figure 3.23 and Figure 3.24, the largest mean EAC movements occur at the high period waves. In general, Morison loads decrease for larger period waves due to a decrease in particle velocity and acceleration. However, another factor influencing this is a result of the orbital path the wave particles follow. For shorter waves, two consecutive legs can experience different force components as the orientation of the water particles vary per leg. This effect can cause the force components to reinforce whenever two consecutive jacket legs are within a wave peak. However, this effect can counteract whenever two consecutive legs are in a peak and through respectively. As visualised in Figure 3.22, the counteracting effect cannot occur for wave lengths (λ) longer than 4 times the leg to leg distance. This condition is reached earlier for long period waves. As can be observed from Figure 4.14, a design wave of H_{max}=4 m result in a counteracting effect for a small period wave and a reinforcement effect for a long period wave. As a consequence, the mean EAC movement is higher for a long period wave. This effect is governing over the decrease in particle velocity and acceleration.

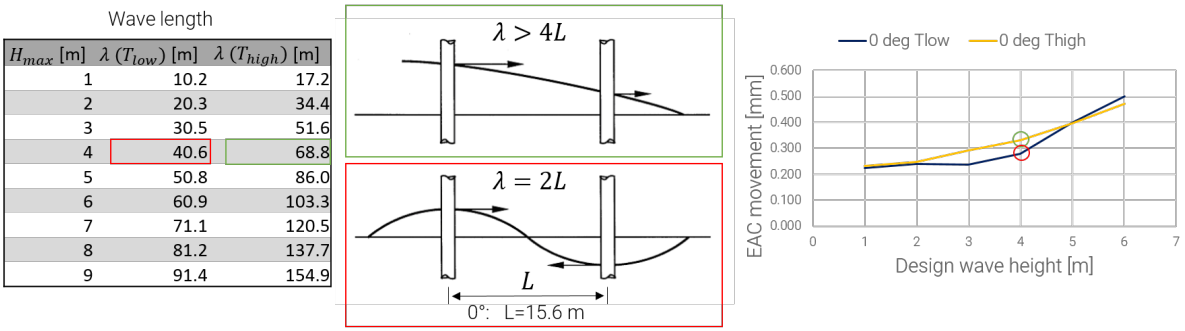

Figure 3.22: Periodical difference absolute EAC for high and low wave period at 0^o.

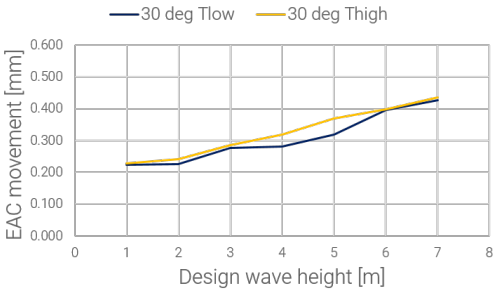

Figure 3.23: Maximum absolute EAC movement for high and low wave period at 30^o.

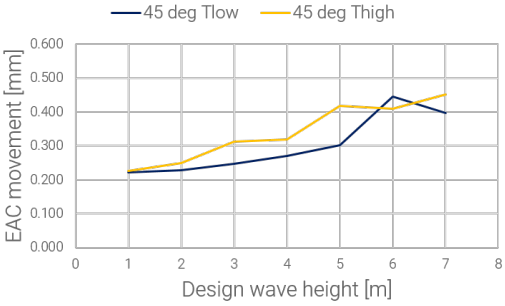

Figure 3.24: Maximum absolute EAC movement for high and low wave period at 45^o.

Sliding at larger design waves

Another observation that can be drawn based on the results from Figure 3.22 (right), Figure 3.23 and Figure 3.24 is that sliding occurs at all load sets. The specific point where sliding occurs is dependent on the wave angle, wave height and period. The magnitude of movement during sliding cannot be displayed since these large displacements and rotations need to be solved by an advanced nonlinear solver. However, one can assume that sliding movement will exceed the 1 mm threshold and is therefore not accepted. In general, sliding is dependent in the magnitude of the normal force, tangential force and a friction coefficient. As a result, this phenomenon is independent of contact area and thus of the size of the stopper. The origin of sliding is therefore the result of a load combination where the tangential force exceeds the traction generated by the normal force. The presence of moments could also influence this phenomenon as it could either decrease the normal component or increase the tangential force. The difference at which sliding occurs for various wave direction is a result of a change in load combination. A trend which is visible is that sliding occurs at higher design waves for waves at an angle. This is the effect of smaller Morison loads at these load cases as explained in the result *"Magnitude of early age cycling movement"*.

3.3.2. Current load

Figure 3.25 shows the maximum EAC movement induced by a current of 0.95 m/s. As shown in Table 2.1, this is the maximum measured current at the Inch Cape site. The EAC movement due to this current is significant when compared to wave induced movements. However, as the mean current speed is 0.29 m/s and the standard deviation 0.15 m/s, these values are extremes that will not be experienced much. One can observe that the current induced movements are largest at 0^o wave angle and smallest at 45^o wave angle. This is in line with the observations from the wave forces.

The current force is, in contrast to the wave loading, a steady force component with a large period oscillation of 6 hours. This will therefore also induce a steady EAC movement offset on top of which the wave induced movement will occur. This steady offset could result in excessive movement or sliding at lower sea states. However, it could also counteract the EAC movement induced by wave loading.

Current speed [m/s]	Direction [deg]	EAC [mm]
0.95	0	0.251
0.95	30	0.242
0.95	45	0.238

Figure 3.25: Maximum absolute EAC movement for current load.

3.3.3. Wind load

The effect of wind load on EAC movement is determined by running a single static loadcase for three wind directions. An operational windspeed of 12 m/s is used which is a realistic value for an installation using the Bokalift 1. The applicable forces for these load cases, as explained in subsection 2.2.3, are displayed in Figure 3.26. The wind load is simulated as a nodal point force at the height of the transition piece. The corresponding EAC movements are displayed in Figure 3.26. The magnitude of these movements are relatively small but can influence the overall results in combination with waves and current.

Wind speed [m/s]	Direction [deg]	Load [kN]	EAC [mm]
12	0	193.7	0.109
12	30	167.8	0.122
12	45	137	0.109

Figure 3.26: Maximum absolute EAC movement wind load.

3.4. Discussion

Since a linear contact algorithm is used to simulate the friction connection, no reliable estimate could be given for the behaviour of the connection after sliding. When using an advanced nonlinear contact algorithm, the model can also be simulated during sliding. This would be done by assigning a dynamic decaying sliding coefficient based on the relative velocity. This would give insight into the behaviour of the connection during sliding.

Assumption A regular design wave is used as an equivalent for simulating with an irregular sea state. A relatively conservative estimate of twice the significant wave height is taken for the design wave to account for any dynamic effect and an irregular sea state. As could be observed from Figure 3.13, this could lead to an over conservative design for some load cases. According to *DNVGL-RP-C205* [18], an irregular sea state may also be used for weather restricted operations if this improves the accuracy of the simulations. This approach would be more accurate. However, it requires to run longer simulations which will result in a less time efficient approach for a large number of simulations.

4

Phase 3: Modified stopper analysis

The detailed reference stopper, as discussed in chapter 3, clearly shows the behaviour of the EAC movement when a fully circular flange connection is used. For this configuration, EAC movement will be limited below 1 mm for most load cases. However, as discussed in section 3.1, stopper design is in reality also dependent on a number of other requirements which can be summarized as:

- Creating on-bottom stability
- Decrease fatigue at stopper during design life
- Adjust for pile misalignment
- Reduce impact loads

As a result, contact surfaces as used in projects are generally smaller resulting in limited performance from an EAC perspective. The objective of this phase is to analyze the effect of a number of key stopper parameters on the behaviour of EAC movement. This phase is subdivided into 4 sub phases as visualised in Figure 4.1.

First of all, the design of three modified stoppers will be discussed. These modified stoppers are geometrically modified to better suit the above mentioned design requirements. These stoppers will be used as an initial investigation and the EAC movement will be determined based on governing load cases from Phase 2. From there, a sensitivity analysis will be performed on the effect of contact area and friction. Furthermore, each configuration will be tested for varying wave directions.

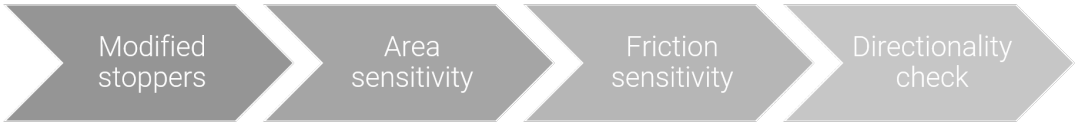

Figure 4.1: Overview phase 3.

4.1. Modified stoppers

This section justifies the considerations made to modify the reference stopper into three stopper configurations. These models will be used as initial starting point for the parameter analysis. The

modelling approach and test load cases will be discussed together with the first results of the EAC movements.

4.1.1. Design considerations modified stoppers

The reference stopper will be modified to three stopper configurations. The main consideration for this modification is to fulfill all design requirements as best as possible, while maintaining the EAC capabilities. In order to investigate the changes needed to achieve this, various real used stoppers are investigated. Figure 4.2 shows a trade off for all five requirements comparing the reference stopper and a possible design for a recent Boskalis project. As can be observed, the optional project stopper behaves well for most requirements except EAC and on-bottom stability. The project stopper is equipped with a cylinder between the jacket leg and stopper plate to improve performance. This cylinder limits fatigue when not operational, can adjust for pile misalignment's when operational and reduces impact loads due to it's damping behaviour. The EAC movement and on-bottom stability of this stopper can be improved by adding an extra pile gripper.

The reference stopper on the other hand, which should work without an extra pile gripper, does not behave well on the requirements of fatigue, pile misalignment and impact loads without the use of extra equipment. These elements should therefore be improved. The general modification needed in order to meet these requirements will be briefly discussed.

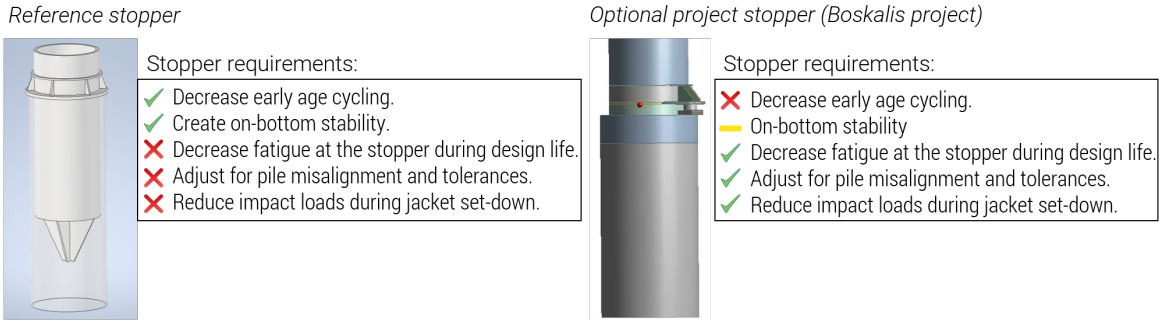

Figure 4.2: Pile stopper design requirement trade off.

- **Decrease fatigue at the stopper during design life**

  In general, decreasing the fatigue can be done by making sure the stopper connection is less stiff compared to the hardened grout connection during the design life of the jacket. This can be done by removing the stopper after grout curing, retracting the stopper using a cylinder or designing it less stiff. Each of these options, as seen in real used stoppers, can most easily be designed when smaller brackets are used. This is visible in the optional reference stopper from Figure 4.2, which uses a cylinder to decrease fatigue.

- **Adjust for pile misalignment**

  Adjusting for pile misalignment is mostly done by using cylinders or shimming plates. As discussed in section 3.1, pile misalignment's reach up to +/- 350 mm. When not accounted for correctly, this could result in a decrease of contact area. As a results of this decrease in area, bending moments could result in rotation and therefore an increase in tangential force or decrease in traction force. Furthermore, a decrease in contact area could lead to overloading of the other stoppers which could lead to failure. As a results, mostly smaller brackets are used as these can be adjusted easily to fit the inclined foundation pile.

- **Reduce impact loads**

  Impact loads can be decreased by lowering the operational sea state, installing with a larger vessel or slowing down the lowering procedure. However, a stopper can actively improve the behaviour of reducing impact loads by including damping cylinders or elastomeric material in the connection. This does not necessarily needs to result in smaller bracket connections. However, in combination with the above mentioned requirements, this is often the case.

When summarizing the above mentioned requirements, the reference stopper can be improved by decreasing the contact area to a number of contact brackets. This allows for the usage of shimming plates or the installation of a levelling cylinder. Furthermore, a contact bracket can more easily be removed by for example a Remotely Operated Vehicle (ROV) when installed at the sea bed. Since the focus of this research is on limiting the EAC movement, no further in depth analysis will be performed on the implications of specific brackets on the other requirements. This should be analyzed in another study.

4.1.2. Modified stopper models

An analysis will be performed on three modified stopper configurations. These configurations, as displayed in Figure 4.3, consist of respectively 2, 3 and 4 brackets. The general dimensions of the stopper brackets are displayed in Table 4.1. These values are based on a stoppers used in a similar sized jacket in order obtain realistic values. Each stopper is designed using sufficient support to assure limited deformation in the brackets. In this way the contact surface will be maximized. The stoppers in configuration 1, 2 and 3 are designed to yield the same initial contact surface. In this way, the three configurations can be compared more accurately. As displayed in Table 4.2, all three configurations have an initial contact area which is 22 % of the reference stopper.

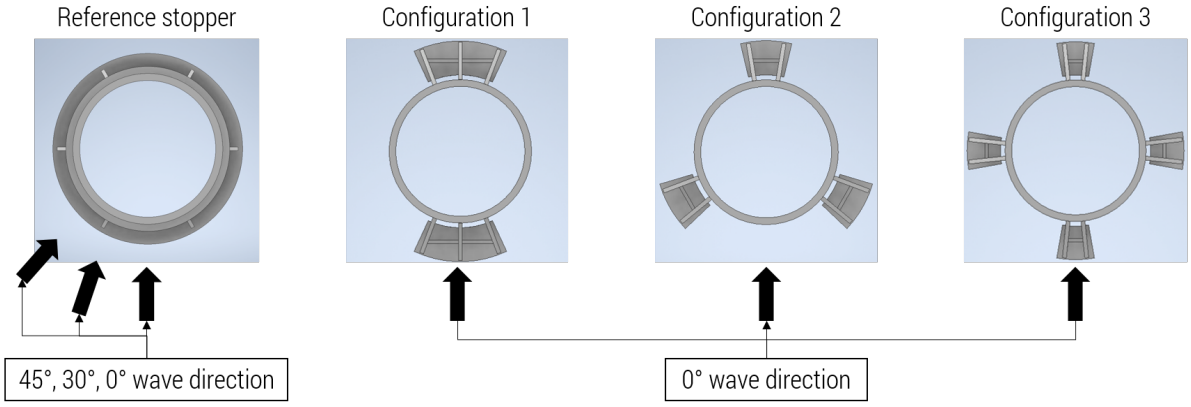

Figure 4.3: Pile stopper configurations and wave direction as used in parameter analysis.

4.1.3. Load cases

The reference stopper, as discussed in section 3.3, is tested on a large number of load cases to fully map the behaviour for varying environmental conditions. For the modified configurations, a more time efficient approach can be used due to the already obtained information.

Based on the results from the reference stopper, large period waves at an incoming angle of 0^0 result in the most severe EAC movement. These wave conditions, as visualised in Figure 4.3, will therefore be used as this will result in a conservative approach to test the modified configurations. The condition which will be used is to ensure EAC movement at H_{max} = 6 m < 1 mm which is a realistic

Table 4.1: General dimensions stopper bracket.

Geometry		
Stopper plate width	505	mm
Stopper plate thickness	60	mm
Vertical connection height	740	mm
Vertical connection thickness	60	mm
Horizontal stiffener height	250	mm
Horizontal stiffener thickness	50	mm
Friction coefficient	0.2	[-]

Table 4.2: Contact area modified stoppers.

Stopper	Contact area m^2	percentage of total %
Reference stopper	0.327	100
Configuration 1, 2, 3	0.0727	22

value used by Boskalis nowadays. According to research performed by Lohaus et al.[48] on a similar North Sea site, the probability of exceeding H_{max} = 6 m within 24 hours is roughly 5% in summer and 22 % in winter. This is given the fact that the maximum initial installation sea state is H_{max} = 6 m. When lowering this threshold, the probability of exceedance becomes much more favourable. In order to observe the behaviour of the EAC movement, a range of load cases as displayed in Table 4.3 will be used to test the modified configurations. A design wave H_{max}=7 m is also included in the simulations. However, this design wave is not part of the design condition.

Table 4.3: Governing load cases for 0^o wave direction.

H_s [m]	H_{max} [m]	T_{high} [s]	Design condition
0.5	1	3.3	EAC < 1 mm
1	2	4.7	EAC < 1 mm
1.5	3	5.8	EAC < 1 mm
2	4	6.6	EAC < 1 mm
2.5	5	7.4	EAC < 1 mm
3	6	8.1	EAC < 1 mm
3.5	7	8.8	

4.1.4. Meshing

The modified stoppers are designed in Femap using the same model configurations as the reference stopper (section 3.2). The stoppers are meshed using CTETRA and CPYRAM elements with midside nodes in order to increase the accuracy of movements and stresses. The mesh quality is checked by making sure the Jacobian matrix norm is below 0.7 as visualised in Figure 4.4 [65]. This is a normal threshold for Femap since some FE solvers adopt a different scale for this measure. The Jacobian describes the amount of element shape distortion with respect to the ideal shape [42]. Furthermore, the foundation pile is modelled with a finer mesh density at the stopper contact locations. This will increase the accuracy of the local deformation at this interface, therefore improving the accuracy of the contact simulation. These conditions are maintained for all stopper models which will be discussed in this chapter.

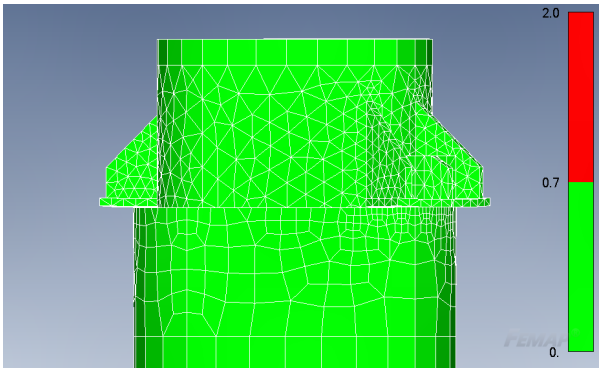

Figure 4.4: Mesh quality check with condition Jacobian < 0.7.

4.1.5. EAC movements

Figure 4.5 shows the EAC movement for the three configurations as displayed in Figure 4.3 and the load cases as displayed in Table 4.3. Note that all these configurations yield the same contact area. When further investigating these movements, a number of conclusions can be drawn.

Configuration 1

H_s [m]	H_{max} [m]	T_{high}[s]	EAC [mm]
0.5	1	3.32	0.923
1	2	4.7	0.953
1.5	3	5.75	1.753
2	4	6.64	2.683
2.5	5	7.42	4.061
3	6	8.13	Sliding
3.5	7	8.78	Sliding

Configuration 2

H_s [m]	H_{max} [m]	T_{high}[s]	EAC [mm]
0.5	1	3.32	0.700
1	2	4.7	0.738
1.5	3	5.75	0.831
2	4	6.64	0.917
2.5	5	7.42	1.033
3	6	8.13	Sliding
3.5	7	8.78	Sliding

Configuration 3

H_s [m]	H_{max} [m]	T_{high}[s]	EAC [mm]
0.5	1	3.32	0.387
1	2	4.7	0.407
1.5	3	5.75	0.466
2	4	6.64	0.520
2.5	5	7.42	0.600
3	6	8.13	Sliding
3.5	7	8.78	Sliding

Figure 4.5: Absolute EAC movement modified stoppers for 0^o and T_{high}.

Magnitude of movements and difference between configurations

The magnitude of movements as displayed in Figure 4.5 vary significantly between configurations and are in general larger when compared to the reference stopper (section 3.3). Furthermore, none of the configurations meet the design conditions of EAC< 1 mm at H_{max}=6 m due to sliding. The magnitude of these movements can be justified when closer examining each configuration.

Figure 4.6, Figure 4.7 and Figure 4.8 show the Von Mises stress and scaled deformation for a design wave of H_{max}=5 m, T=7.4 s at time step 0.16 s for each configuration. This time step results in the largest stresses within the analysis of that specific design wave. A visual observation that can be made from these figures is the variation in stress and deformation between the configurations. All three configurations show a similar stress hot spot in the interface between the pile and stopper. These stress hot spots result in element strain and therefore elastic deformation at these areas. For a smaller number of brackets, the stress distribution around the circumference of the pile becomes less uniform. This effect is visible when comparing the stress around the circumference of the pile top. Since the loading combination is similar for all configurations, limited stress distribution results in larger stress variations around the circumference of the pile and therefore larger variation of deformations as visible in Figure 4.6. Although the contact area is similar for all three configurations, the effective area differs slightly due to deformations at the pile stopper interface. As a result, the largest stress is can be observed at the edges of the stopper pads.

Another factor influencing the difference in EAC movement between configurations is the result

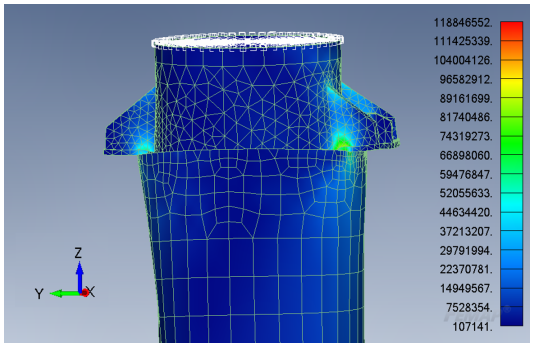

Figure 4.6: Von Mises stress and deformation (scale 2) for configuration 1 at H_{max}=5 m, T=7.4 s and t=0.16 s.

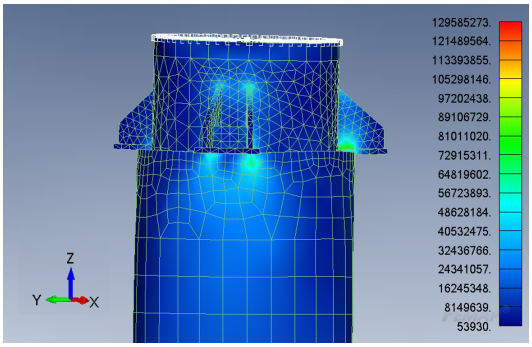

Figure 4.7: Von Mises stress and deformation (scale 2) for configuration 2 at H_{max}=5 m, T=7.4 s and t=0.16 s.

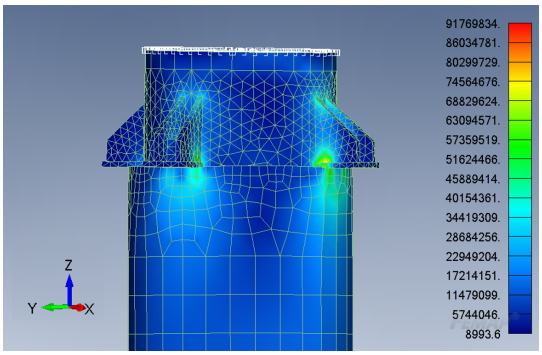

Figure 4.8: Von Mises stress and deformation (scale 2) for configuration 3 at H_{max}=5 m, T=7.4 s and t=0.16 s.

of the complex loading combination, which is the input for the model. For larger wave loads, the influence of moments starts to become significant in the response of the model. As explained in section 3.3, larger wave loads will induce a horizontal force component perpendicular to the wave direction which causes deviation of the pile with respect to the center line. The moments induced by these large wave loads did not induce significant extra movement for the reference stopper since it is supported around the full circumference of the pile. As the modified stoppers are not fully supported around the circumference of the pile, the effect of rotation due to moments becomes significant. In the case of the two bracket stopper, a moment around the y-axis (Figure 4.6) will induce a rotation that can not be limited by a bracket. This will therefore result a in large relative rotation at a 90^o angle to the wave direction. This phenomenon will be called moment induced rotation and will be further discussed in section 4.2.

4.2. Contact area sensitivity

The initial modified configurations do not meet the design criterion of EAC movement at H_{max}=6 m < 1 mm. Each configuration will be analysed by increasing the contact surface as visualised in Table 4.4. Each analysis step will result in a similar increase in contact surface between the three configurations to be able to compare the configurations per analysis step. The increase in contact surface per iteration is based on increasing the bracket angle of configuration 1 by 20^o. Since the stiffness of each stopper is sufficiently high, the main contributor towards the EAC movement is the deformation of the pile. The deformation of the stopper is negligible. Figure 4.9, Figure 4.12 and Figure 4.13 show the overview per configuration for this sensitivity study. The total contact area including the percentage of the reference stopper is displayed above each stopper. The bottom left table in each overview shows the EAC movement per stopper for the same load cases. The bottom

right graph visualises this movement. All analysed stopper are displayed in Appendix G.

Table 4.4: Stopper contact area per sensitivity step.

Stopper	Sensitivity number	Contact area [m^2]	percentage of reference [%]
Reference stopper	-	0.327	100
Configuration 1,2,3 (reference)	0	0.073	22
Configuration 1,2,3 (Sensitivity 1)	1	0.091	28
Configuration 1,2,3 (Sensitivity 2)	2	0.127	39
Configuration 1,2,3 (Sensitivity 3)	3	0.164	50
Configuration 1,2,3 (Sensitivity 4)	4	0.200	61

Figure 4.9 shows the results of the sensitivity study for the first configuration. As can be observed from the bottom left table, the EAC movements are generally high for lower contact surfaces. Only sensitivity 4 meets the criteria where the EAC movement at H_{max}=6 m < 1 mm. Figure 4.12 shows the overview for the second sensitivity study. Here, non of the load cases meet the design criterion as sliding occurs at H_{max}=6 m. However, the EAC movement at lower waves is generally smaller compared to configuration 1. The same holds for Figure 4.13, showing the results for configuration 3. The following observations can be made:

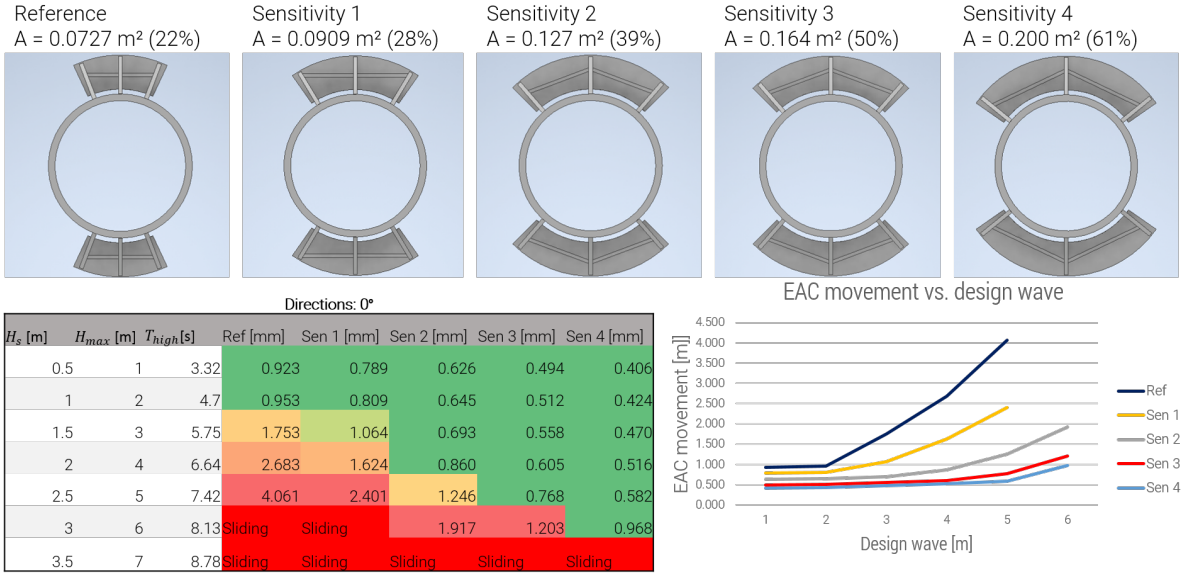

Figure 4.9: Area sensitivity study for configuration 1.

Moment induced rotations

As briefly discussed in subsection 4.1.5, moment induced rotations negatively influence the EAC movement for the two bracket stopper of configuration 1. The main problem is the moment in line with the wave direction, causing a rotation around this axis which can not be limited by a bracket. This effect is mainly visible for higher load cases. As a results, a large EAC movement occurs at 90^o angle to the wave direction. This effect disappears whenever the angular reach of the bracket becomes significantly large to limit the rotation. This effect is visualised when displaying two models for configuration 1 (Figure 4.10 and Figure 4.11) with respectively the smallest and largest bracket. Both models display the scaled deformation and Von Mises stress for a wave of H_{max}=6 m and T=8.13 s at time step 0.1 s. This is just before sliding occurs for the small bracket model.

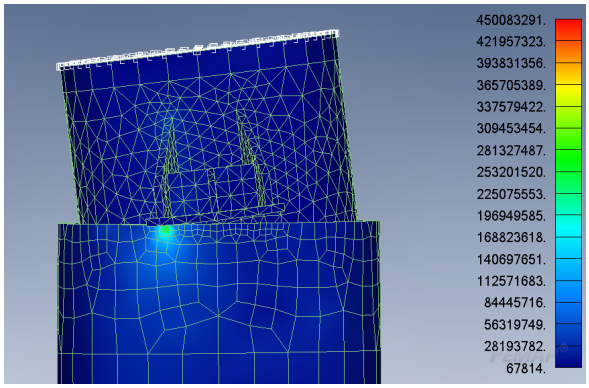

Figure 4.10: Moment induced rotation (scale 1.5) for configuration 1 reference model (A=0.0727 m^2) at H_{max}=6 m, T=8.13 s and t=0.1 s.

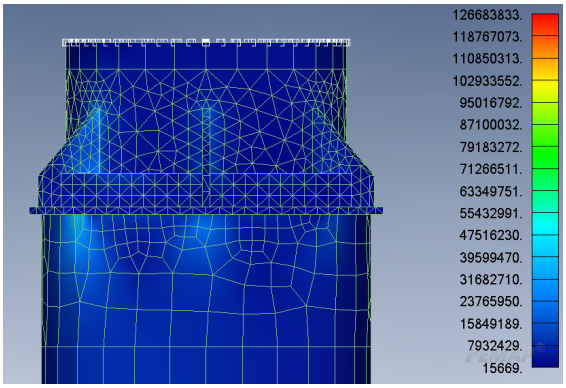

Figure 4.11: Moment induced rotation (scale 1.5) for configuration 1 sensitivity 4 model (A=0.200 m^2) at H_{max}=6 m, T=8.13 s and t=0.1 s.

As can be noted, the moment induced rotation causes local rocking of the jacket leg on the bracket resulting in large EAC movement. For the larger bracket with sufficient angular reach, this rotation can be limited. This effect is clearly visible for all models when observing Table 4.5, showing the direction of the largest EAC movement with respect to the incoming wave angle. For smaller brackets (reference, Sen 1), the direction of the largest EAC movement occurs at a 90^o angle to the wave direction. These movements are mainly moment induced. However, for larger brackets (Sen3, Sen4) this tendency moves back in line with the wave direction 0^o.

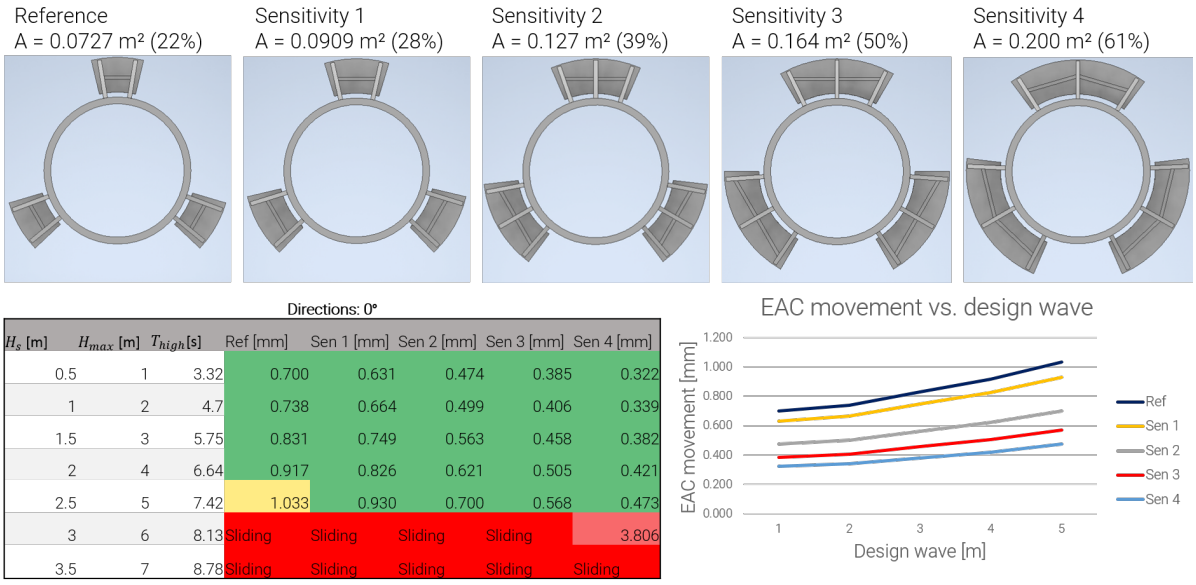

Figure 4.12: Area sensitivity study for configuration 2.

Moment induced rotations are hardly visible for the stoppers of configuration 2 and 3. Due to their more laterally located brackets, rotations are limited. This tendency is visible when comparing the bottom right graph of Figure 4.9, Figure 4.12 and Figure 4.13. Configuration 1 shows an exponentially increasing trend while configuration 2 and 3 show a more linear increasing trend. This exponential increase is the effect of moment induced rotations at large design waves causing excessive EAC movements. The linear trend for configuration 2 and 3 indicate that this phenomenon hardly occurs here. This can be verified by looking at Table 4.6, showing the absolute deviation of the largest EAC movement with respect to incoming wave angle for configuration 1 and 2. For configu-

Table 4.5: Direction of largest EAC movement with respect to the incoming wave angle for configuration 1.

H_s [m]	H_{max} [m]	T_{high} [s]	Absolute deviation from wave angle [^{o}]				
			Reference	Sen 1	Sen 2	Sen 3	Sen 4
0.5	1	3.32	0	0	0	0	0
1	2	4.7	23	0	0	0	0
1.5	3	5.75	90	90	23	0	0
2	4	6.64	90	90	23	23	0
2.5	5	7.42	90	90	90	23	0
3	6	8.13	90	90	64	36	23
3.5	7	8.78	Sliding	Sliding	Sliding	Sliding	Sliding

ration 2, little deviation can be observed supporting the fact that moments are generally absorbed by the laterally located brackets. For configuration 3, a little deviation can be observed for higher sea states. These deviations however, are not significantly higher compared to the reference stopper and can be induced by forces.

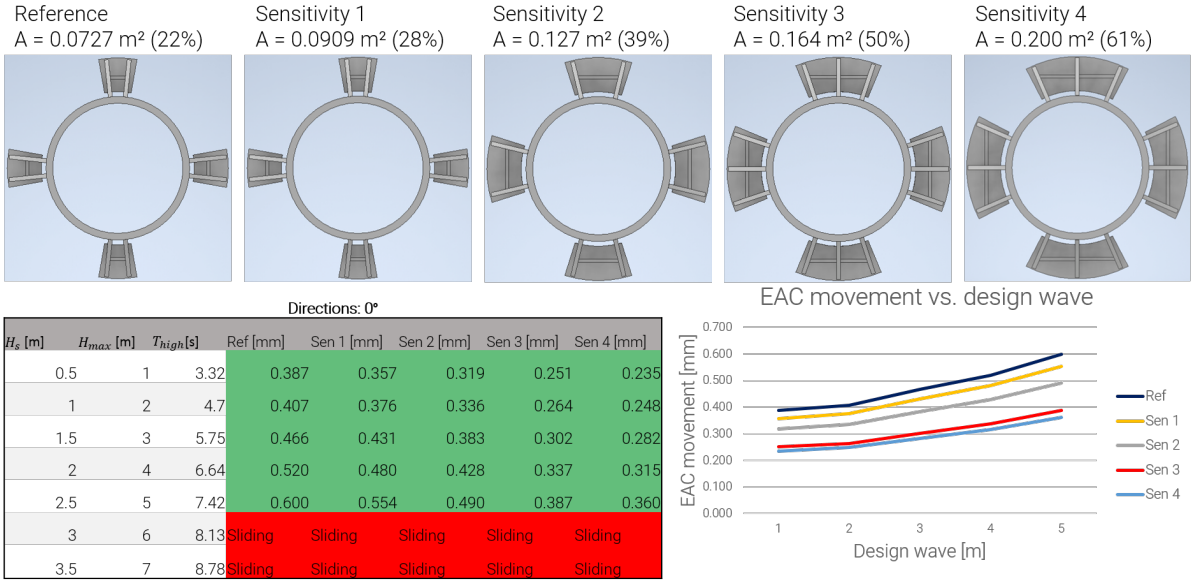

Figure 4.13: Area sensitivity study for configuration 3.

Table 4.6: Direction of largest EAC movement with respect to the incoming wave angle for configuration 1 and 2. S denotes 'sliding'.

H_s [m]	H_{max} [m]	T_{high} [s]	Absolute deviation Conf 2 [^{0}]					Absolute deviation Conf 3 [^{0}]				
			Ref	Sen 1	Sen 2	Sen 3	Sen 4	Ref	Sen 1	Sen 2	Sen 3	Sen 4
0.5	1	3.32	0	0	0	0	0	0	0	0	0	0
1	2	4.7	0	0	0	0	0	13	13	0	0	0
1.5	3	5.75	0	0	0	0	0	13	13	13	13	13
2	4	6.64	0	0	0	0	13	13	13	13	13	13
2.5	5	7.42	0	0	13	13	13	26	26	26	26	13
3	6	8.13	S	S	S	S	23	S	S	S	23	26
3.5	7	8.78	S	S	S	S	S	S	S	S	S	S

Magnitude of the movements

When comparing the magnitude of the movements from Figure 4.9, Figure 4.12 and Figure 4.13 some interesting observations can be made. First of all, sliding occurs for all configurations at H_{max} = 7 m. This is in line with expectations as this also occurred at the reference stopper. However, sliding also occurs for most cases of configuration 2 and 3 at H_{max} = 6 m while this is not the case for configuration 1. This is contradictory to the EAC movement which are generally larger for configuration 1 when compared to configuration 2 and 3. These two observations state that sliding is an independent phenomenon and not directly related to the magnitude of EAC movement. As explained in section 3.3, the critical component within sliding is the traction induced by the normal force whereas EAC movement is less dependent on normal force. When closer observing the cases for configuration 1 at H_{max} = 6 m where sliding does not occur, some small slipping is visible in the results. No clear conclusions can therefore be drawn and further research should indicate the behaviour of the stopper at the tipping point between sticking and sliding.

When observing the load cases where sliding does not occur, a clear trend between contact surface and EAC movement is visible. Figure 4.14 shows the average EAC movement per configuration for increasing contact area. Configuration 2 and 3 show a relatively linear decreasing trend while configurations 1 shows a more exponentially decaying function. This relatively rapid decrease is the effect of limiting moment induced rotations. Furthermore, one can observe all configurations converging towards an asympthote which is the average value for the reference stopper.

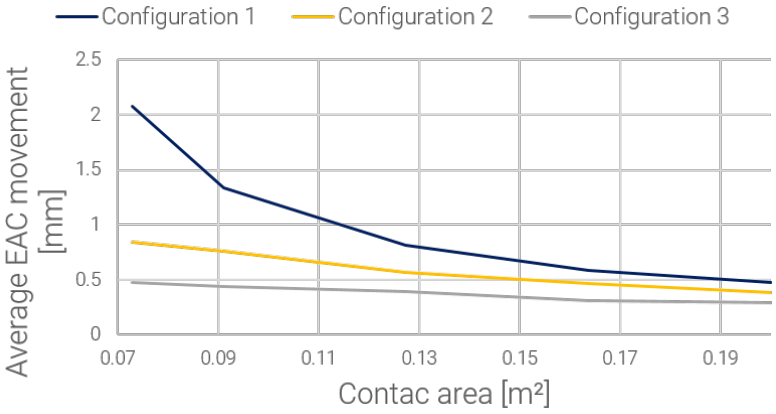

Figure 4.14: Average EAC movement vs. contact area.

4.3. Friction sensitivity

As described in section 3.2, a friction coefficient of 0.2 [-] is adopted since this is a conservative estimate for steel to steel friction under water. However, the usage of a frictional coating on the steel stopper surface can increase the friction coefficient and therefore might improve the behaviour of the connection. A conservative estimate for a frictional coating is taken as $\mu = 0.4$ [-] [61]. In order to efficiently assess the result of such a coating on the behaviour of the stopper connection, the critical load case of H_{max} = 6 m is simulated for all stopper models till the design condition of EAC<1 mm is met. Figure 4.15 shows the EAC movement for H_{max}=6 m, T=8.13 s and a friction coefficient of μ=0.2 [-] and μ=0.4 [-].

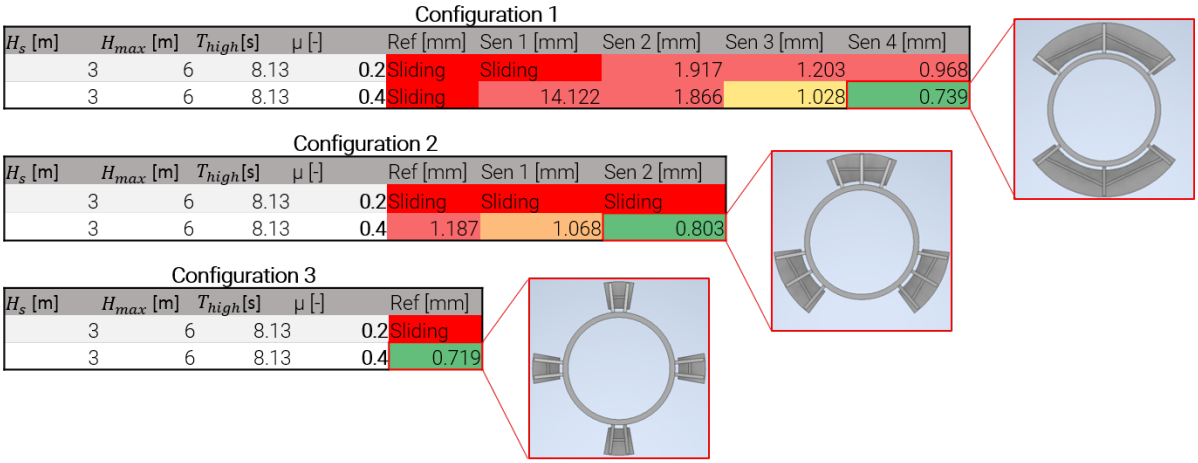

Figure 4.15: EAC movement for H_{max} = 6 m and μ=0.2 [-] and μ=0.4 [-].

As can be observed from Figure 4.15, an increase in friction coefficients (μ=0.2 [-] to μ=0.4 [-]) results in less sliding for all stoppers. A frictional sensitivity study is performed on all configurations for the same design condition (EAC<1 mm). The model at which the design criterion is met varies per configuration. Using more brackets, when comparing configuration 3 to configuration 1, results in a more optimal design from a contact surface point of view. This is summarized in Table 4.7 showing the contact surface needed in order to meet the design condition.

Table 4.7: Contact surface per configuration to meet design criteria: EAC movement at H_{max}=6 m < 1 mm. The sensitivity models correspond to Figure 4.9, Figure 4.12 and Figure 4.13.

Configuration	Sensitivity model	Contact area [m^2]	Percentage of reference [%]
Configuration 1	Sensitivity 4	0.200	61
Configuration 2	Sensitivity 2	0.127	39
Configuration 3	Reference	0.073	22

One can conclude that an increase in friction optimizes the performance of the stopper within the load cases where sliding occurs. However, as explained in section 4.2, sliding and EAC movement are different concepts. In order to also investigate the influence of friction on EAC movement for non-sliding load cases, the analysed stoppers as displayed in Figure 4.15 will be simulated with a friction coefficient of μ=0.4 [-] for a range of load cases.

Configuration 1, Sensitivity 4

H_s [m]	H_{max} [m]	T_{high}[s]	μ=0.2 [mm]	μ=0.4 [mm]
0.5	1	3.32	0.406	0.403
1	2	4.7	0.424	0.421
1.5	3	5.75	0.470	0.467
2	4	6.64	0.516	0.514
2.5	5	7.42	0.582	0.580
3	6	8.13	0.968	0.739
3.5	7	8.78	Sliding	0.834

Configuration 2, Sensitivity 2

H_s [m]	H_{max} [m]	T_{high}[s]	μ=0.2 [mm]	μ=0.4 [mm]
0.5	1	3.32	0.474	0.470
1	2	4.7	0.499	0.496
1.5	3	5.75	0.563	0.560
2	4	6.64	0.621	0.618
2.5	5	7.42	0.700	0.698
3	6	8.13	Sliding	0.803
3.5	7	8.78	Sliding	0.941

Configuration 3, Reference

H_s [m]	H_{max} [m]	T_{high}[s]	μ=0.2 [mm]	μ=0.4 [mm]
0.5	1	3.32	0.387	0.383
1	2	4.7	0.407	0.404
1.5	3	5.75	0.466	0.463
2	4	6.64	0.520	0.517
2.5	5	7.42	0.600	0.598
3	6	8.13	Sliding	0.719
3.5	7	8.78	Sliding	0.811

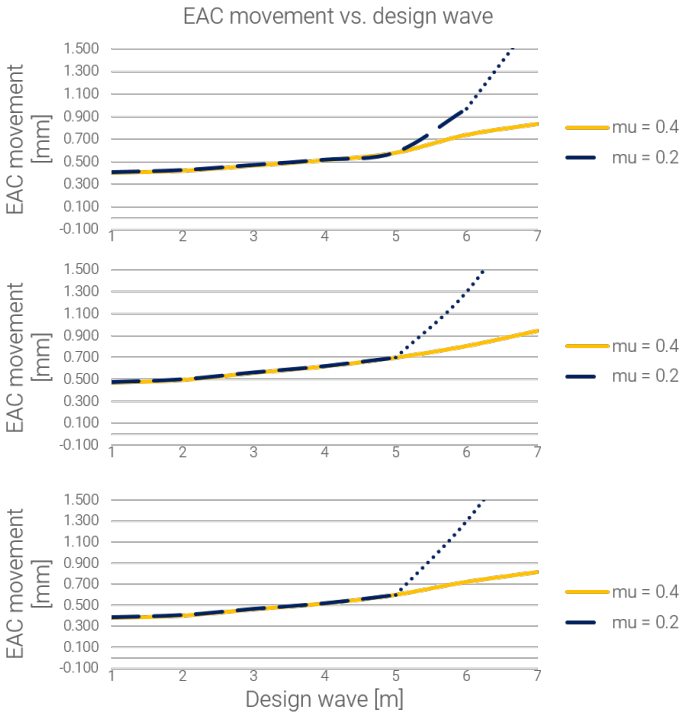

Figure 4.16: EAC movement for three analysed configurations at μ=0.2 [-] and μ=0.4 [-].

Figure 4.16 shows the EAC movement for two friction coefficients, μ=0.2 [-] and μ=0.4 [-], for all three analysed stopper configurations. Furthermore, all movements are visualised. When observing the magnitude of the EAC movement, one can conclude that for non sliding load cases, the effect of increased friction is negligible. This is also visualised in the graphs showing identical lines for both cases. However, at 'sliding' or 'almost sliding' (H_{max}=6 m, H_{max}=7 m) load cases, the effect of friction is significant. For these cases, the increase in friction facilitates the stopper to remain in position without translational movement. The stopper then follows a trend which is also visible for all other load cases as discussed in subsection 4.1.5. Therefore, one can conclude that friction does not influence EAC movement significant for non-sliding occurs. However it does improve the behaviour for sliding load cases.

4.4. Directionality check

All sensitivity studies so far have been simulated using an incoming global wave direction of 0^o. This wave angle, as discussed in section 3.3, resulted in the largest EAC movement for the reference stopper. However, due to the geometrical difference between the modified stopper configurations and the reference stopper, a change in wave direction might result in different effects. Furthermore, as discussed in subsection 2.1.1, swell induced waves and wind induced waves are likely to attack at a different angle. For the Inch Cape site, this increases the possibility of encountering different wave directions within 24 hours. Therefore, the stopper configurations will also be tested for an incoming wave direction of 30^o and 45 ^{o}. Configuration 1 will also be tested at an incoming angle of 90^o. Due to geometry, this is not needed for configuration 2 and 3. All three analysed stoppers are similar to the ones used in the friction sensitivity as displayed in Figure 4.15 and use a friction coefficient of μ=0.4 [-]. The results are displayed in Figure 4.17, Figure 4.18 and Figure 4.19.

Sensitivity 1, Opt 4

H_s [m]	H_{max} [m]	T_{high}[s]	EAC 0 deg [mm]	EAC 30 deg [mm]	EAC 45 deg [mm]	EAC 90 deg [mm]
0.5	1	3.32	0.403	0.397	0.394	0.561
1	2	4.7	0.421	0.415	0.426	0.590
1.5	3	5.75	0.467	0.472	0.509	0.663
2	4	6.64	0.514	0.516	0.515	0.728
2.5	5	7.42	0.580	0.577	0.645	0.816
3	6	8.13	0.739	0.610	0.631	0.896
3.5	7	8.78	0.834	0.663	0.681	0.967

Figure 4.17: Maximum absolute EAC movement for analysed stopper in configuration 1 (μ=0.4 [-]) at 0^o, 30^o, 45^o and 90^o.

Sensitivity 2, Opt 2

H_s [m]	H_{max} [m]	T_{high}[s]	EAC 0 deg [mm]	EAC 30 deg [mm]	EAC 45 deg [mm]
0.5	1	3.32	0.470	0.463	0.458
1	2	4.7	0.496	0.487	0.503
1.5	3	5.75	0.560	0.568	0.621
2	4	6.64	0.618	0.632	0.631
2.5	5	7.42	0.698	0.716	0.817
3	6	8.13	0.803	0.769	0.799
3.5	7	8.78	0.941	0.835	0.874

Figure 4.18: Maximum absolute EAC movement for analysed stopper in configuration 2 (μ=0.4 [-]) at 0^o, 30^o and 45^o.

Configuration 3, Reference

H_s [m]	H_{max} [m]	T_{high}[s]	EAC 0 deg [mm]	EAC 30 deg [mm]	EAC 45 deg [mm]
0.5	1	3.32	0.383	0.377	0.373
1	2	4.7	0.404	0.396	0.409
1.5	3	5.75	0.463	0.467	0.502
2	4	6.64	0.517	0.514	0.510
2.5	5	7.42	0.5980	0.591	0.657
3	6	8.13	0.719	0.634	0.643
3.5	7	8.78	0.811	0.724	0.703

Figure 4.19: Maximum absolute EAC movement for analysed stopper in configuration 3 (μ=0.4 [-]) at 0^o, 30^o and 45^o.

When observing the critical load cases at H_{max}=6 m, one can conclude that for all configurations the 0^o wave angle results in the highest EAC movement except for the 90^o case of configuration 1. Table 4.8 shows the average EAC movement for all configurations and incoming wave angles. As one can observed, the 45^o wave angle at configuration 2 yields higher average movements compared to the 0^o wave angle. Furthermore, all load cases with 45^o wave direction result in higher average movement compared to 30^o. This is different when compared to the reference stopper where the 45^o load cases resulted is the smallest movement. This change compared to the reference stopper can be justified by the location of the brackets for all analysed stoppers. For all stoppers, the support at 45^o wave angle is less compared to the support at 30 ^{o}. However, in general the 0^o load cases still result in the largest movements. Especially in the high waves which are governing for the design condition. This can be justified by the fact that the global loads are still the largest at this angle. One can conclude that, although the average movements might be higher at an angle, the design criterion is still met for all load cases.

The 90^o case for configuration 1 shows the largest movements. These movements are expected due to the lack of lateral located brackets. The origin of this movement is similar to the moment induce rotations as explained in subsection 4.1.5. Although the magnitude of movement is within limits for this case, one should pay attention since the magnitude of these sidewards EAC movement can be significant.

Table 4.8: Average early age cycling movement for configuration 1,2 and 3 and wave direction 0^o, 30^o, 45^o and 90^o.

Wave direction [^{o}]	Mean EAC Conf 1 [mm]	Mean EAC Conf 2 [mm]	Mean EAC Conf 3 [mm]
0	0.565	0.655	0.557
30	0.522	0.639	0.529
45	0.543	0.672	0.543
90	-	-	0.746

4.5. Practical feasibility

The focus within phase 3 has been to analyse three stopper configurations which have been modified based on the design requirements as discussed in subsection 4.1.1. The theoretical behaviour of these configurations is examined in this study resulting in clear observations from an EAC point of view. However, these theoretical observations might deviate from the practical feasibility when examined thoroughly. This section therefore discusses the benefits and limitations for potential implementation.

4.5.1. Stopper configurations versus design requirements

The main approach used in this research is to analyze the stoppers to fulfill all design requirements as best as possible, while maintaining the EAC capabilities. As a result, a sensitivity study is performed on three modified stopper configurations with the condition to reduce EAC movement below 1 mm for a design wave of H_{max}=6 m. These stopper configurations, as displayed in Figure 4.20, Figure 4.21 and Figure 4.22 will be discussed from a practical point of view. This will be done according to the design requirements as displayed below.

- Creating on-bottom stability
- Decrease fatigue at stopper during design life
- Adjust for pile misalignment
- Reduce impact loads

Figure 4.20 shows the analysed model for configuration 3. This model can reduce the EAC movement below 1 mm with a contact surface that is 22% of the reference stopper. It furthermore behaves well on minimizing the moment induced rotations due to the lateral located brackets. The bracket size is limited and might therefore be designed to be not removed after grout curing. However, if removal is necessary using an ROV, this would be an inefficient task due to the number of brackets. As the contact area is small, the supports are well suited for the usage of shimming plates or a levelling cylinder. The downside of using four supports is that the system is statically undetermined. Theoretically, one bracket would therefore float above the foundation pile which could overload the other supports leading to failure. In reality, deformation of the leg and stopper will result in a better alignment. However, till what extend this occurs should be further investigated.

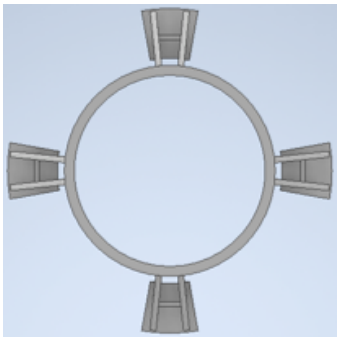

Figure 4.20: Configuration 3

Figure 4.21 shows the analysed model for configuration 2. This model can reduce the EAC movement below 1 mm with a contact surface that is 39% of the reference stopper. It also behaves well on reducing the moment induced rotations. However, the relative size of the brackets is larger when compared to configuration 3. Removing these brackets after jacket installation might therefore be inefficient. A benefit however is that this stopper is statically determined due to its number of brackets. The size of the brackets could still be used to install shimming plates or a levelling cylinder when compared to other projects investigated by Boskalis.

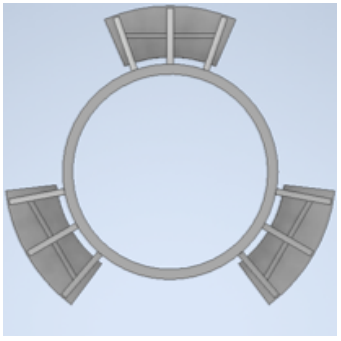

Figure 4.21: Configuration 2

Figure 4.22 shows the analysed model for configuration 1. This model can reduce the EAC movement below 1 mm with a contact surface that is 61% of the reference stopper. This model only behaves well on moment induced rotation whenever the angular reach of the brackets is large enough. However, the size of these brackets might become practically inefficient. It is difficult to use shimming plates or a levelling cylinder for such a contact surface since the variation of height underneath the bracket becomes too large. Furthermore, the bracket should be attached to the pile with at least three supports to provide enough stiffness. Removing the bracket therefore also becomes time inefficient.

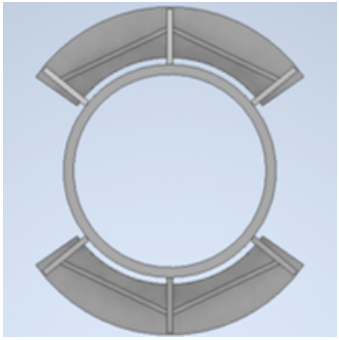

Figure 4.22: Configuration 1

4.5.2. Applicability range of the general pile-leg geometry

The general pile-leg geometry, as summarized in Table 3.1, is set as a fixed scope for this study. This geometry follows from the pile reaction loads which are the effect of a series of design steps. In order to assess the applicability range of the current research, the effect of varying a number of general parameters will be discussed.

Diameter jacket leg and foundation pile

The effect of jacket leg and foundation pile diameter on the EAC movement is an important parameter to assess since this can vary between projects. Simulating this change for the current modelling approach would result in changing the global and detailed model. When physically examining this, an increase in pile diameter would result in an increased horizontal stiffness for the jacket system. As a result, the horizontal deformation of the pile will be less which leads to a reduction of EAC movement. Furthermore, an increased pile diameter leads to a reduction of required grout length and therefore a reduction of the leg insert. Part of the EAC movement is caused by rotation at the stopper and is therefore dependent on the length of the leg insert. However, increasing the pile diameter while keeping the thickness constant might locally lead to extra deformation in the pile. This could therefore counteract the reduction of EAC movement due to a globally stiffer system.

Quantifying the difference in EAC movement for a decrease or increase in diameter is a complex study due to the dependency of several jacket parameters. Increasing the diameter would increase the horizontal moment of inertia and therefore the bending stiffness with a power of 4. Increasing the diameter would also lead to a decrease of grout length. This is based on the grout capacity which is a non-linear relation. On the other hand, the effect of the leg insert with respect to EAC movement is a linear relation. The amount of extra deformation due the larger diameter, which counteracts the reduction of EAC movement, is a non-linear relation. These relations make it complex to quantify the actual change in EAC movement due to varying diameter. Assessing this therefore requires a thorough parameter study.

Grout connection length

As discussed in section 3.3, the largest EAC movement can be measured at the bottom of the jacket leg since the pivot point of the connection is located at the pile-leg interface. When increasing the length of the jacket leg insert, the distance between the rotation point and bottom of the jacket leg increases. As a result, the EAC movement linearly increases.

Width grout annulus

Since no grout stiffness is taken into account for the current study, the effect of the grout annu-

lus width is negligible. When taking grout stiffness into account, this parameter should be further investigated.

Wall thickness foundation pile and jacket leg

Since no grout stiffness is taken into account, zero stress will be taken by the leg insert underneath the pile-leg interface. Varying this parameter has therefore no influence on the current study. However, a variation in thickness of the foundation pile will most likely have an influence on the EAC movement. The effect of pile thickness on the horizontal stiffness of the pile is linear. This can therefore most optimally be changed by adjusting the diameter. However, as discussed in subsection 4.1.5, stress hot spots underneath the bracket in the pile-leg interface cause elastic deformation of the pile top. This is a large contributor towards the EAC movement whenever moment induced rotations do not occur. Increasing the pile thickness will decrease this elastic deformation. As a result, EAC movement might be reduced. This increase in pile thickness can also be done locally at the top. Since the top section of the pile already has an increased wall thickness for the grouted connection or piling interface, adding extra steel will result in minimal cost. This might therefore be an effective way to cost efficiently reduce EAC movement.

4.5.3. Alignment of jacket for wave angle

In order to optimize the behaviour of a potential pile stopper, an optimal rotation with respect to the jacket should be determined given the fact that the jacket is optimally rotated with respect to the governing wave load.

In general, jacket heading is based on a maximum operational ULS load case. Note that this case is mainly wind driven. From an EAC point of view, the stopper should then be orientated to be in line with the direction of the maximum pile loads. These pile loads are mostly wave induced since the first 24 hours after grout installation are of interest. Furthermore, the effect of any moment induced rotations should be investigated. One should therefore investigate moments in a direction without a bracket support. As explained in subsection 4.1.5, more stoppers would improve this behaviour.

Note that the pile stopper is a temporary support. The orientation should therefore coincide with the wave loading during the first 24 hours. A study into the seasonal effects of wave loads could therefore be interesting. Furthermore, the option to adjust the orientation of a stopper before installation could be an innovative extra.

4.6. Discussion

Phase 3 discusses the analysis of three modified stoppers. These configurations consist of respectively 2, 3 and 4 brackets. A clear trend which is visible from the results is that an increase in number of brackets result in a decrease in EAC movement. This holds for the same contact area when compared to other configurations and is an effect mainly induced by a more even distribution of stresses around the circumference of the pile. In order to assess what the limit for this statement is, a number of extra stoppers should be tested with an increased amount of brackets. This allows to check what the optimum number of brackets is for a specific contact surface.

Two friction coefficients of respectively 0.2 [-] and 0.4 [-] have been adopted in this study. 0.2 [-] is a conservative estimate for steel to steel friction under water while 0.4 [-] is an estimate for a coefficient reached when using a frictional coating. The actual magnitude of these coefficients is difficult to asses since a large range of numbers can be found in literature. Furthermore, these coefficients of friction are dependent on various effects such as contact pressure or surface roughness. Performing small scale tests with a varying contact pressure would be optimal in order to verify this coefficient

for the specific project. This would allow to use a more validated number which might result in a more accurate simulation.

5

Conclusion and Recommendations

The objective of this thesis is to gain insight into the modelling approach and magnitude of EAC movement and investigate how these movement can efficiently be minimized. This will be investigated in order to *define a relation between stopper design and EAC movement in the grout connection of an offshore wind jacket structure*. This objective is reached by dividing this research into three phases. 1) Investigating the modelling approach and setting the design parameters of a global jacket model in order to obtain accurate interface forces. 2) Investigating the EAC movements in a detailed reference model in order to define the behavior and quantify the magnitude of movements. 3) Assess the effect of stopper modifications on EAC movement to obtain a more realistic design and analyse these modifications by means of a sensitivity study from an EAC point of view. During this research, the effect of stiffness induced by grout is not taken into account. This is recommended by the *DNVGL-ST-1026* since the stiffness for the first 24 hours is limited and unpredictable.

This chapter provides conclusions that can be drawn from the results as discussed in chapter 2, chapter 3 and chapter 4. Furthermore, it describes recommendations for any further work on this subject. First, the main conclusion will be drawn after which the conclusions from each phase will be summarized.

Main conclusion

Early age cycling and relative sliding of the jacket-pile interface are two different phenomena which need to be limited in order to meet the EAC design criterion as stated in *DNVGL-ST-0126*. EAC tends to be most efficiently solved by increasing the number of brackets in order to evenly distribute the stress around the circumference of the pile while limiting moment induced rotations in line with the wave direction. The effect of moment induced rotations on the magnitude of EAC movement is significant as it could result in rotation of the stopper around the axis of the wave direction. It therefore needs to be limited by all means. Furthermore, sliding can most efficiently be solved by increasing the friction coefficient. This is highly recommended since it greatly improves the performance of the stopper connection for larger waves.

5.1. Conclusions

5.1.1. Phase 1 - Global model

Phase 1 (chapter 2) describes the modelling approach for a global jacket model which will be used to simulate the response for a number of load cases. The non-linear effect of soil-pile interaction in

this model is linearized by adopting an apparent fixity method as described in subsection 2.2.5. This method is based on modelling the foundation piles as cantilever beams with equivalent properties below the mudline in order to match the stiffness of a soil-pile system with discrete lateral springs. Linearizing the soil-pile interaction for all load cases induces some uncertainty since the actual behavior is non-linear. A sensitivity study on this uncertainty showed that this could induce an error in the range of 14% as shown in Figure 2.15. Calibrating the model for the correct apparent fixity length or modelling with discrete later springs would reduce this uncertainty.

5.1.2. Phase 2 - reference model

Phase 2 (chapter 3) describes the initial EAC movement for a detailed pile-leg model with a reference stopper. The interface forces which will act as an input for this model are obtained by simulation the global model (*phase 1*) for a number of design waves with a quasi-static analysis. This design wave will act as an equivalent largest wave to replace irregular wave conditions. Based on recommendations from the *DNV GL*, a design wave height of H_{max}=2H_s is adopted. In order to check the accuracy of this assumption, a comparison study is performed for a design wave with a quasi-static analysis versus an irregular sea state with a dynamic analysis. The results showed that, when comparing the seabed force and moment characteristics, the extreme values of the design wave are slightly higher compared to the irregular sea state as visualised in subsection 3.2.3. This is also visible when simulating the EAC movement for both cases. In general, the most probable maximum wave height in an irregular sea state is described as H_{max}=1.86H_s. Simulating with the current design wave is therefore a conservative approach for estimating EAC movement. These higher values are therefore in line with expectations.

The reference stopper is modelled as a full circular flange which has a perfect alignment to the foundation pile in order to maximize the contact surface. A friction coefficient of 0.2 [-] is adopted. Two phenomena can be identified when examining the results of the simulations as presented in section 3.3. For smaller sea states, till a design wave of H_{max}=7 m, EAC movements can be measured which do not exceed the maximum allowed threshold criterion of 1 mm. At higher sea states, sliding occurs resulting in an EAC movement exceeding the criterion of 1 mm. There are no cases where the EAC movement exceeds 1 mm without sliding. The results are divided into non-sliding and sliding cases and will be discussed.

Non-sliding cases

EAC movement can be measured by examining the relative movement between the outer shell of the jacket leg and the inner shell of the foundation pile. The location of the largest EAC movement on the outer shell of jacket leg can be expressed by determining the corresponding height and angle on the circumference of the leg. For non-sliding cases, the largest EAC movement can always be measured at the tip of the jacket leg as displayed in Figure 3.17. When examining the pile-leg system, the pivot point of the connection is located at the pile-leg interface. The location furthest from this pivot point will experience the largest movement, which is the tip of the jacket leg. Increasing the length of the jacket leg will therefore result in a larger EAC movement.

The location of largest EAC movement on the circumference of the jacket leg can vary dependent on the wave load. For the reference stopper, the largest movement is generally measured in line with the wave direction which will be denoted as the centerline. For a number of load cases, the location of largest EAC movement can also deviate from this centerline as seen in Figure 3.18. These deviations mostly occur for cases with a 0^o global wave angle and reduce as the wave angle increases towards 45^o. These deviations are a result of the pile moving out of line with the wave direction due to a horizontal force component perpendicular to the incoming wave. This horizontal force component as displayed in Figure 3.19 is always present due to the inclined geometry of the jacket. The

self-weight of the jacket induces a compressive forces on the jacket leg. Due to the inclined orientation of the leg, a horizontal and vertical reaction force are needed to create equilibrium. For larger wave loads, this compressive member force increases inducing a larger horizontal resultant force. As a result, the jacket leg moves out of line with the wave direction as displayed in Table 3.6. For increased incoming wave angles (towards 45^o), the direction of the horizontal reaction force moves more in line with the main wave direction. As a result, the deviation of largest EAC movement with respect to the centerline decreases. The angle of largest EAC movement with respect to the circumference of the pile is an important parameter to investigate. It might lead to an optimal location for installing a potential simple mitigation measure such as a cylinder at the tip of the leg. These measures can be cost effective ways to reduce the EAC movement in a project.

Another observation that can be made is the directional difference between EAC movement for low and high period waves as displayed in Table 3.7. The largest mean EAC movements occur when the waves attack the structure perpendicular (0^o) and decrease for larger wave angles. This is a result of the local particle kinematics normal to the structure decreasing when the structure is attacked at an angle as visualised in Figure 3.21. Although the global projected area increases for waves at an angle, the effect of decreased particle kinematics is governing.

Furthermore, the largest mean EAC movements occur at high period waves as displayed in Table 3.7. In general, Morison loads decrease for larger period waves due to a decrease in particle velocity and acceleration. However, due to the orbital path these particles follow, two consecutive jacket legs can experience different forces dependent on the wave length. This effect can result in two force components counteracting as displayed in Figure 3.22. For larger waves (larger than 4 times the leg to leg distance), this effect disappears and the force components for two consecutive legs will reinforce each other. Since this reinforcement occurs earlier for large period waves, the mean EAC movement is higher. This effect is governing over the decrease in Morison loads for large period waves.

Sliding load cases

Sliding occurs for all load sets when observing Figure 3.14, Figure 3.15 and Figure 3.16 and is dependent on the wave angle, height and period. The magnitude of movement during sliding cannot be assessed correctly due to limitations in the contact algorithm. However, the threshold of 1 mm will be exceeded during sliding and does therefore need to be minimized. The occurrence of sliding is independent of contact area and mainly a result of limited normal force or a large tangential force. The occurrence of sliding decreases for waves at angle which is the effect of smaller Morison loads as explained in this section.

5.1.3. Phase 3 - Modified stopper analysis

The objective in *Phase 3* (chapter 4) is to analyse the behaviour of EAC movement for modified stoppers which have a more realistic design from a project perspective. Based on the design criteria of decreasing the fatigue life, being able to adjust for pile misalignment and reducing impact loads, the contact area of the flange is decreased and split into a number of brackets (subsection 4.1.1). This results in the introduction of three new stopper configurations as can be observed in Figure 4.3. These configurations, denoted as configuration 1,2 and 3 are designed with two ,three and four brackets respectively. Each configuration yields the same total contact surface. These configurations are tested for governing load cases based on the results from *phase 2*. The initial configurations show significantly larger EAC movements when compared to the reference stopper as displayed in Figure 4.5. In general, the EAC movement decreases when the number of brackets increase. This can be related to the stress distribution in the foundation pile. An increased number of brackets results in a more even stress distribution around the circumference of the pile therefore reducing excessive

element strain and pile deformation. The opposite is visible for configuration 1 (2 bracket stopper), showing large elastic deformation at the bracket-pile interface due to an un-even stress distribution as shown in Figure 4.6.

Area sensitivity

A sensitivity study is performed by increasing the total contact area of each configuration with similar steps as described in section 4.2. This results in increasing the angle of each stopper bracket. When observing the EAC movement per load case, configuration 1 shows different results compared to configuration 2 and 3 as visualised in the bottom right graph of Figure 4.9, Figure 4.12 and Figure 4.13. While the relative increase in EAC movement for consecutive load cases is linear for configuration 2 and 3, an exponential increase can be observed for configuration 1. This effect originates from a lack of support for the two bracket stopper in the direction perpendicular to the incoming wave. Similar as the horizontal force component induced by the inclination of the structure, a downward force component results in reaction moments which becomes significant for larger sea states. A moment around the axis of the incoming wave will result in a rotation perpendicular to the wave angle. Due to the lack of lateral support for configuration 1 (2 bracket stopper), this rotation can cause large EAC movement as visualised in Figure 4.10. This effect is not visible for the reference stopper since it is fully supported around the circumference of the pile. This effect, which will be denoted as moment induced rotations, results in an EAC movement at 90^o angle to the wave direction as visualised in Table 4.5. The effect of moment induced rotations on EAC movement is significantly larger when compared to EAC movement induced by force. It can be mitigated by increasing the angular reach of the brackets.

The effect of sliding for configuration 1,2 and 3 is similar as the reference stopper. Sliding occurs for a design wave of H_{max}=6 m and higher. Since this phenomenon is independent of area, limited difference can be observed for larger stopper configurations.

When observing the average EAC movement per contact area, as visualised in Figure 4.14, the mean movements converge towards an asympthote which is the EAC movement of the reference stopper. The mean movement of configuration 1 decreases rapidly since a larger contact surface and angular reach result in a decrease of moment induced rotation. Furthermore, configuration 3 (4 brackets) results in the best performance form an EAC point of view.

Friction sensitivity

Based on the area sensitivity, configuration 1,2 and 3 could be designed to limit the EAC movement below 1 mm for non sliding load cases. However, the occurrence of sliding is problematic at a design wave of H_{max}=6 m and larger. Since this phenomenon is independent of area, this cannot be solved by increasing the contact surface of the stopper. By using a frictional coating, the friction coefficient could be increased which would optimize the behaviour with respect to sliding. For this research, an increase in friction coefficient from 0.2 [-] to 0.4 [-] is adopted. Using this modification greatly improves the performance of the stoppers for larger design waves as explained in section 4.3. As a result, sliding does not occur and therefore EAC movements can be measured. All stopper configurations are therefore tested until the design criterion of decreasing EAC movement at H_{max}=6 m < 1 mm is met as seen in Figure 4.15. When describing the contact area needed in order to meet this criterion, in percentage of the reference stopper, configuration 1 yields 61%, configuration 2 yields 39% and configuration 3 yields 22%. The performance of the 4 brackets configuration has thus significantly improved by increasing the friction coefficient. The effect of increased friction on non-sliding load cases is negligible as visualised in Figure 4.16. This supports the statement that sliding and EAC are two different phenomena.

Directionality

All sensitivity studies so far have been tested for a 0^o wave angle. In order to check whether the observations also hold for different wave angles, 0^o, 30^o and 45^o wave simulations are run with a friction coefficient of 0.4 [-]. Furthermore, configuration 1 (2 bracket) is tested at 90^o which is not necessary for the other configurations due to symmetry. Similar results are found in comparison to the reference stopper yielding the largest movement at 0^o wave angle as displayed in Table 4.8. Only the 90^o case for configuration 1 resulted in larger loads compared to the 0^o case. This is in line with expectations since limited support is present in this direction for configuration 1. This states the importance of a multiple bracket configuration in order to limit the movement in all directions.

5.2. Recommendations

Based on the executed research, a number of recommendations can be made. These recommendations will be divided into two groups: 1) for further improvement of the current study and 2) as a proposal for extra research.

Some recommendations for improvement of the current study are mentioned in the discussion of each chapter. The most important will be summarized.

- A number of modifications in this research could improve the accuracy of the overall results. Some assumptions made in this study impose an uncertainty that is present in the individual results. Since small deformations are of interest, it is important to critically assess these uncertainties. Improving the accuracy will in most of these cases result in larger simulations. This is therefore recommended if sufficient computational power is available or if less simulations will be performed. Three main assumptions will be discussed.

    1. Based on computational efficiency, a modelling approach is adopted which divides the total problem into a global model and detailed model. The simplified global model does not account for any relative movement between the pile-leg interface and is modelled using beam elements. The detailed model does account for relative movement using a friction connection. Using the interface forces from the global model as an input for the detailed model does induce some uncertainty as visualised in Figure 2.20. However, this uncertainty is limited as long as small movements are investigated. Performing the simulations on a full structure, as visualised in Figure 1.13, would reduce this error. Furthermore, this would allow to simulate the system with a re-distribution of forces. As a result, concepts such as a one bracket stopper could be tested. These concepts would only be stably in the current detailed model by constraining them to prevent rotation around the bracket.
    2. Another uncertainty imposed by an assumption is the usage of an apparent fixity model to capture the soil-pile interaction. By analysing all load cases for the same apparent fixity length, part of the non-linearity of the soil is neglected. Varying the apparent fixity length for different load cases or ranges of load cases would be an improvement to this method as visualised in Figure 2.15. However, using an apparent fixity method would always result in a linearization of the soil. Capturing the non-linear behaviour would be possible by modelling soil-pile interaction using p-y curves. These could also be combined with t-z curves to more accurately map the axial movement. Comparing this approach with the current method requires the usage of an advanced non-linear solver which is not available for the current study. This would therefore be recommended for any further research.

3. The response of the global model is simulated using a design wave with a quasi-static analysis. This design wave is used to account for any extreme movement induced by a dynamically simulated model in an irregular sea state. A relatively conservative factor of twice the significant wave height is taken for this design wave in order to capture all effects of the irregular sea state. This factor is based on recommendation from the *DNVGL-ST-0126*. In general, the maximum wave in an irregular sea state is denoted as 1.86 times the significant wave height. Since limited dynamic response is expected due to the high first natural frequency, twice the significant wave height should result in a conservative estimate. A comparison study is performed between the design wave and irregular sea state (subsection 3.2.3) showing indeed a small over prediction of EAC movement for the design wave (Figure 3.12, Figure 3.13). Running the simulations for an irregular sea state would therefore result in more realistic values. This might lead to a more cost effective design.

- The load cases used in this study represent a one directional wind, wave or current situation. The behaviour of EAC under mixed loading conditions is an important factor to investigate. As mentioned in subsection 2.1.1, a combination of swell induced waves and wind induced waves can create a complex loading condition which could result in large EAC movement. For the Inch Cape site, the main swell induced wave direction ranges from north-east to south-east while the main wind induced wave direction is south-west. Furthermore, the current runs from north-northeast to south-southwest while the wind is predominantly south-west. As concluded in chapter 3, the magnitude of current and wind induced EAC movement can be significant. Testing a combination of load cases is therefore vital in order to fully asses the magnitude of EAC movement which could be present at the site.

The recommendations as a proposal for extra research are outlined in the next section:

- The current research has been performed for a fixed jacket geometry at a specific site. In order to normalize the research to make it more suitable for general usage, one could perform a large sensitivity study on a number of critical design parameters. From a geometrical point of view, one could start by varying the water depth at the location to asses the EAC movement for different sites. This could be combined with changing the soil properties. Furthermore, the influence of submerged weight due to the amount of flooded members will greatly influence the results. Changing the weight of the jacket will have a direct effect on the sliding behaviour of the stopper connection. However, it also influences the horizontal forces and moments due to the batter angle of the structure. Another important geometrical parameter is the number of legs. This will change the response of the jacket due to wave loading but also the stiffness at the bottom.

- An interesting small scale modification that can be investigated is to including extra horizontal bracing at the mudline. This would increase the stiffness in horizontal direction and might therefore positively improve the behaviour of moment induced rotations. Also, changing the thickness of the foundation pile at the top might result in better performance. A thicker pile top will result in less elastic deformation therefore decreasing the EAC movement. Furthermore, less deformation will improve the quality of the contact surface resulting in a more even stress distribution. Also, a fixed scope within this research are the global parameters of the grout connection. As discussed in section 3.2, these parameters are based on ULS and FLS cases according to *DNVGL-ST-0126*. However, within this design regulation, there is option to vary global parameters such as grout length or annulus thickness as discussed in section 4.5. Varying these parameters will influence the behaviour of the model. A sensitivity study on this might lead to the an optimal global grout connection from an EAC point of view.

- The current models are designed with ideal contact surfaces which have an initially perfect alignment. In reality, the possibility occurs that one of the stopper pads does not align well with the foundation pile. This should be avoided by conducting thorough surveys before jacket installation and shimming out possible misalignments. Furthermore, cylinders could be used to minimize this. However, assessing the consequences of this is important and could be done by for example modelling the foundation pile under an angle.
- A statistical study on the MetOcean conditions is interesting to investigate as this might change the current design criterion. According to *DNVGL-ST-0126*, the largest sea state within 24 hours after installation is governing for the assessment of EAC movement. Increased insight into the 24 hour statistics of MetOcean conditions might optimize this value. Furthermore, one could assess the statistics of changing wave direction within 24 hours. This could lead to a stopper design which allows for some rotational adjustment before installation. Therefore, the bracket could be optimally positioned for the incoming wave direction within 24 hours.

A

Time dependency of grout curing

The shear strength of grout is time dependant and therefore changes during the curing process. According to the *DNVGL-ST-0126* [17], grout can in general be compared to concrete as their compounds are similar but the relative proportions differ. This difference mostly results in grout being less viscous which increases the workability. Existing literature on concrete can therefore be used to support statements made about grout.

The material properties of grout are time dependant due to the hydration of the cement. Cement is the chemical compound that binds the material. Hydration is a process in which cement reacts with water, causing the grout to harden. During the hydration process of grout, the material properties change rapidly causing the grout to increase in strength. According to [43], this strength increase will continue to develop given that:

- There is still un-hydrated cement present in the grout.
- The humidity of the grout stays above approximately 80 % [63].
- The temperature of grout remains within tolerances (e.g. not below the minimum curing temperature stated by the manufacturer).
- There is enough space for the hydration to take place.

Given that all the above mentioned conditions are fulfilled, the grout can in reality cure for years and the strength development will continue. Figure A.1 shows the increase in concrete strength over the years provided that all of the above conditions are met. One can clearly see how the strength continues to develop. However, notice should be made that this is unlikely to occur. In the case of a grout connection, part of the grout will not be in contact with water due to the surrounding pile. The humidity will therefore drop below 80% which will stop the hydration process at an earlier age.

This effect is visualised using Figure A.2 which shows the influence of moisture on the strength increase of concrete. One can clearly state that strength stops developing as moisture is not available. Furthermore, the amount of strength development depends on the chemical composition of the grout or concrete [10].

As it is difficult to determine the maximum design strength of concrete, regulation provides a framework in order to quantifiable measure and compare different types of concrete. Therefore, the compressive strength is axially measured at an age of 28 days. This test age is set as industry believes

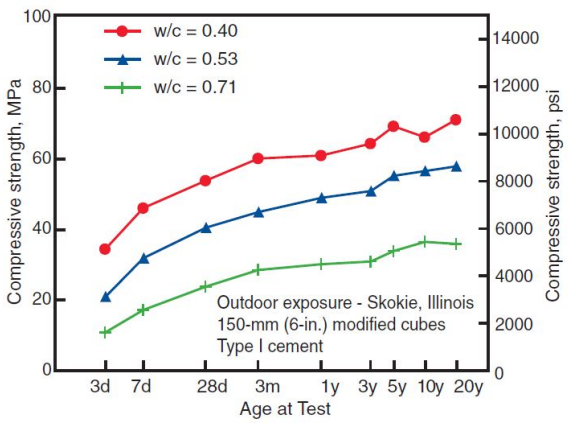

Figure A.1: Concrete strength gain versus time for concrete exposed to outdoor conditions. w/c denotes the water/cement ratio [23]

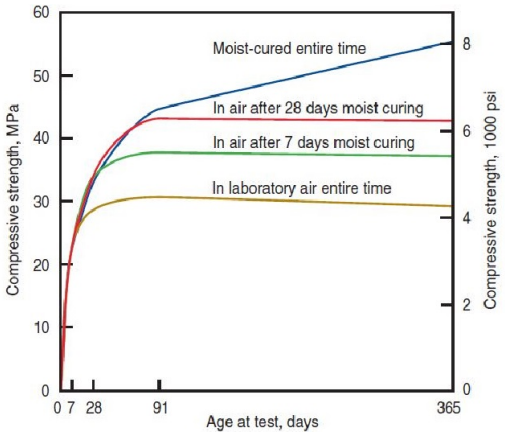

Figure A.2: Concrete strength increases with age as long as moisture and a favorable temperature are present for hydration of cement [76]

the material has gained most of it's strength by then. Furthermore, as a rule of thumb, one can state that the strength of concrete reaches 75% of the compressive strength at 7 days. More test ages can be used if necessary.

The strength development for concrete is also applicable for present day grout. Several high strength grouts (HSG) are available and used in the offshore wind industry. Research done by [46] investigates the strength development for a chemically optimised grout product and a commercially available grout product for the offshore wind industry as visualised in Figure A.3. One can clearly see that the compressive strength of grout more than doubles from day 1 till day 56.

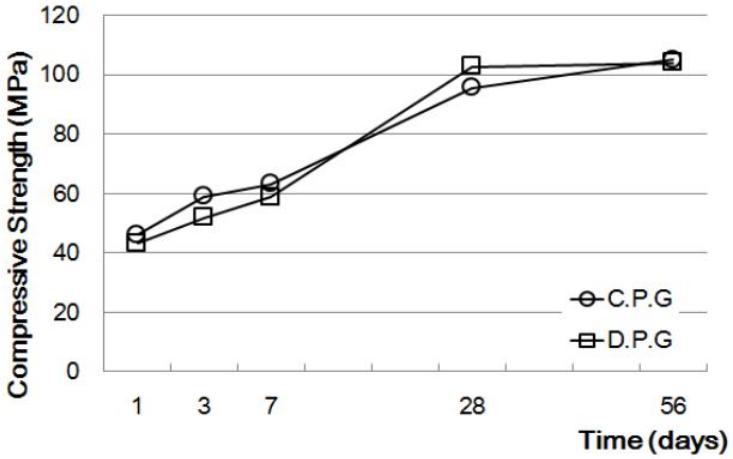

Figure A.3: Compressive strength test results (C.G.P: Commercial grout products; D.G.P: Development grout products) [46]

Most test data, including Figure A.3, describe the compressive strength behaviour of grout from 1 day after casting till maximum strength is reached. However, for the case of early age cycling, the first 24 hours are of interest. As grout properties are difficult to determine during these hours, manufacturers and design regulations only use material properties after this time. Gaining insight into the grout properties before this time is beneficial in order to understand the early age cycling problem.

A.0.1. Early-age properties

The period from the first hours till days after casting can be referred to as early-age within concrete literature as the definition is not strict. However, for this research, the first 24 hours will be referred to as early-age. According to [57], the fundamentals of early-age behaviour of concrete are not yet fully understood. They are interrelated with various factors and testing is complex.

The early-age of concrete or grout can be divided into two phases. The first phase is the setting of the grout which can be divided into a stiffening and final setting part. The second phase is the hardening of the grout.

Setting and Hardening
During setting, the fluid like grout becomes a solid as a result of the hydration taking place. The first period of setting can also be referred to as stiffening. According to [27], during stiffening the fluid starts losing plasticity and particles are temporary bonded by van der Waals bonds and electrostatic bonds. However, remixing at this stage is still possible resulting in the formation of new bonds. This is a critical phase during early age cycling as sedimentation and segregation can take place as investigated by Lohaus et al.[49]. The strength of grout in this phase can be modelled by a fluid with high viscosity which is enclosed in the grout annulus.

Gradually, grout starts to enter an accelerated hydration phase which is called setting. At this stage, the hydrated material increases rapidly and therefore the amount of liquid decreases. As hydration is a chemical process, this results in heat generation. Chemical bonds are now formed between the particles and therefore, breaking these bonds by remixing will result in permanent damage. External temperature and moisture effects are more critical in this stage of curing if compared to a more mature stage. These external effects have a direct influence on the mechanical properties due to the influence on the chemical bonds which are formed [57]. It it therefore difficult to make reliable strength estimations in this early stage of the curing process. Furthermore, according to [27] the process of setting depends on the water cement ratio and the added chemicals which can act as 'setting regulators'. During the setting process, the grout will crumble under a compressive force. After final setting, the grout is fully solid.

During the hardening process, the strength of the grout develops. Together with this, the modulus of elasticity increases.

Early-age strength determination
Measuring the strength of grout within the first 24 hours is difficult as the material, especially in the first stage of curing, cannot be tested accurately under a compressive strength test because it will crumble. In order to evaluate the early-age compressive strength, [78] performed measurements using an ultrasonic sensor which determines surface wave velocity through a material. These measurements were performed on four types of concrete which were enclosed in a box. Each type of concrete was cured at five different temperature levels; 5 °C, 15 °C, 20 °C, 30 °C and 35 °C. Figure A.4 shows the surface wave velocity versus curing time for two concrete mixtures with a design strength of 40 Mpa (left) and 80 Mpa (right). The surface wave velocity is given for the five mentioned temperature levels and can be related to the compressive strength. Furthermore, the initial (stiffening) and final setting times are shown which are determined by a penetration resistance test. One can see that for the first hours of curing, a lot of scatter is visible in the figure and no clear trend can be distinguished. Reason for this is the fact that the hydration phase has not yet stared as described by [27]. The concrete therefore still behaves as a viscous fluid. However, after a few hours, a sharp increase in surface wave velocity can be distinguished which represents the hydration of the concrete. The surface wave velocity levels out towards an asymptote which indicates that ultrasonic measurements are only suitable for monitoring very young concrete.

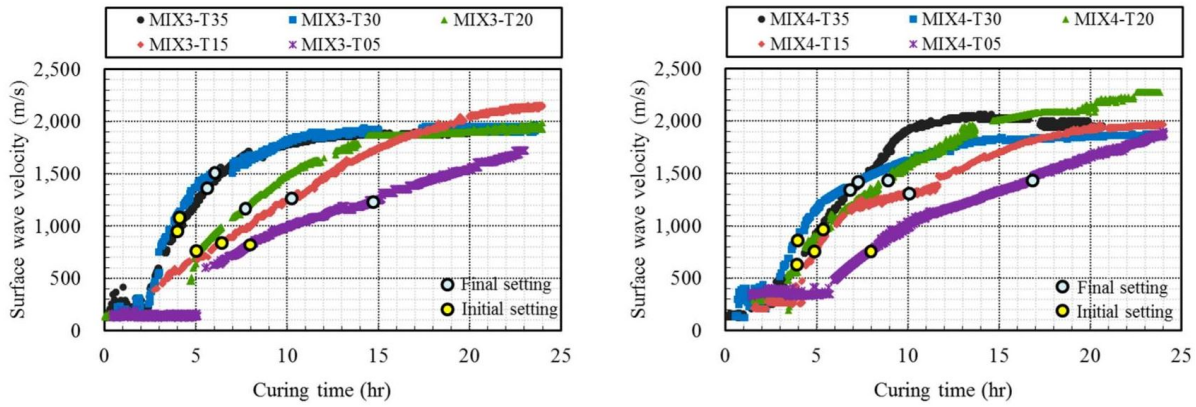

Figure A.4: Surface wave velocities with the initial and final setting times versus curing tie [46]. 40 Mpa design strength left figure and 80 Mpa design strength right figure.

The surface wave velocity is linked to the compressive strength using an empirical formulation. This formulation is dependant on curing temperature and validated using compressive strength test specimens at older age (20-24 hours) and existing literature [41],[60]. This relation is described in Equation A.1 where f_c is the compressive strength [N/mm^2], k is an empirical temperature coefficient [-] and V_R is the surface wave velocity [km/h].

$$f_c = 0.0098ke^{3.412V_R} \tag{A.1}$$

The concrete mixture with a design strength of 80 Mpa (Figure A.4 right) represents the grout which is used in a jacket annulus best. The surface wave velocity values of this grout are transformed to compressive strength using Equation A.1 and Figure A.4 (right). This results in the compressive strength for different curing times and temperatures as displayed in Table A.1. Note that values for 30 ° and 35 ° are left out as these are unlikely to occur in sea water.

Table A.1: Early age compressive strength [Mpa] for curing time and temperature. Design strength of concrete is 80 Mpa.

Curing temperature [°C]	**Compressive strength [Mpa]**					
	4 h	**8 h**	**12 h**	**16 h**	**20 h**	**24 h**
5	-	0.0619	0.2424	0.4797	1.335	2.642
15	0.0563	0.6135	1.214	4.752	6.685	9.403
20	0.1567	0.8630	3.378	9.403	13.22	26.17

From Table A.1, one can see that the compressive strength after one day (24 h) is significantly affected by the curing temperature. The difference in compressive strength between 5 °C and 20 °C is more than 23 Mpa. Low temperatures will decrease the heat generation during the hydration process and therefore slow down the strength development in the concrete [11]. The external heat can therefor be seen as a catalyst for the hydration reaction. The results from Table A.1 can be compared with the compressive strength as proposed by offshore grout manufacturers nowadays. Table A.2 shows the early age compressive strength for three offshore high strength grouts (HSG) at a curing temperature of 20 °C.

The values from Table A.2 are in line with the measured values from [78] as displayed in Table A.1.

As shown in Table A.1 and discussed above, low temperatures will influence the hydration process and therefore significantly decrease the compressive strength after 24 hours. However, aver-

Table A.2: Early age compressive strength [Mpa] for curing time at 20 °C and high strength grouts on the market.

Grout manufacturer	**Design strength [Mpa]**	**Compressive strength [Mpa]**	
		24 h (20 °C)	**3 day (20 °C)**
Subcon HSG	60	20	40
Five strar HSG	90	34.5	-
BASF Masterflow 9800 HSG	100	-	75

age North Sea temperatures can vary from approximately 3 °C to 23 °C depending on location and season [15]. According to DNVGL-ST-0126 [17], hardening test should be performed when water temperatures below 20 °C are measured. However, the combination of low temperatures and early age cycling is not mentioned. Due to low temperatures, the duration of early age cycling can easily exceed 24 hours as the grout compressive strength might not be sufficient enough to rigidly fix the connection. Therefore, the cyclic behaviour might continue for a longer period resulting in increased damage in the grout connection.

B

Global jacket model

Table B.1: Jacket dimension with respect to LAT in meters.

Hub height	Water depth	Top of pile	Top of deck	Tower bottom	Bottom of BL	Top of BL	Upper splash zone	Lower splash zone
123	-54.59	-50.64	17.53	27.96	-5.00	12.50	9.00	-2.70

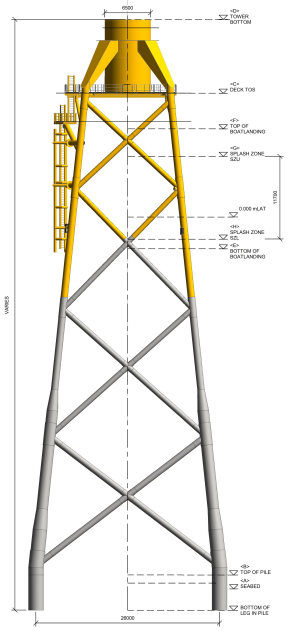

Figure B.1: General arrangement Inch Cape jacket structure.

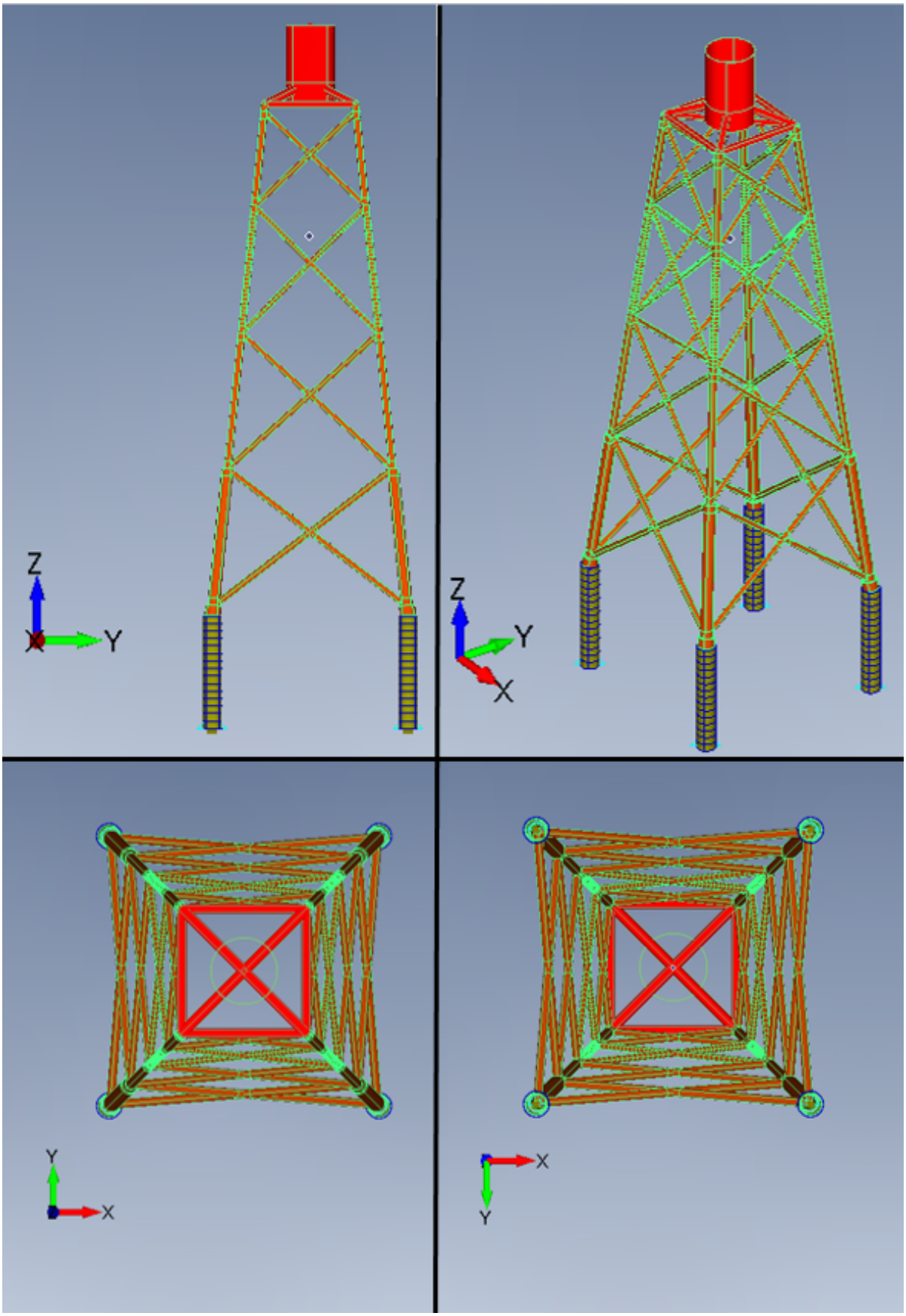

Figure B.2: FE model from left, dimetric, top and bottom view

C

Hydrodynamics

C.1. Wave theory

The particle kinematics used for the Morison equation are calculated using the applicable wave theory. The most basic theory of all is the linear or Airy wave theory which represents a regular sinusoidal wave. These waves, also described as small amplitude waves, are valid if the amplitude is much smaller than the wave length and water depth. Several finite amplitude wave theories have been created to elaborate on the linear wave theory. In a finite amplitude wave, the amplitude cannot be considered as small when compared to the wave length or the depth of the water column [73]. Because higher order terms are now taken into account, these waves become non-linear and therefore do not follow a sinusoidal shape. Finite amplitude waves tend to have peaked crests and broad troughs. There is not one finite amplitude wave applicable for a certain water depth which makes modelling more difficult.

Figure C.1 shows the shows the application of different wave theories as adopted in a book about water waves from LeMehaute [45]. The horizontal axis shows the shallowness while the vertical axis shows the steepness of the wave. Furthermore, Figure C.1 shows the regime of interest for the current research. This regime has been calculated by using the wave height and period as presented in the load cases. A water depth of 52 meter is used which represents the simulated jacket. One can conclude that at least a Stokes 3rd order wave is needed in order to realistically map the particle kinematics. This is verified using the reltion as adopted in the *DNVGL-RP-C205*[18] as shown in Figure C.2.

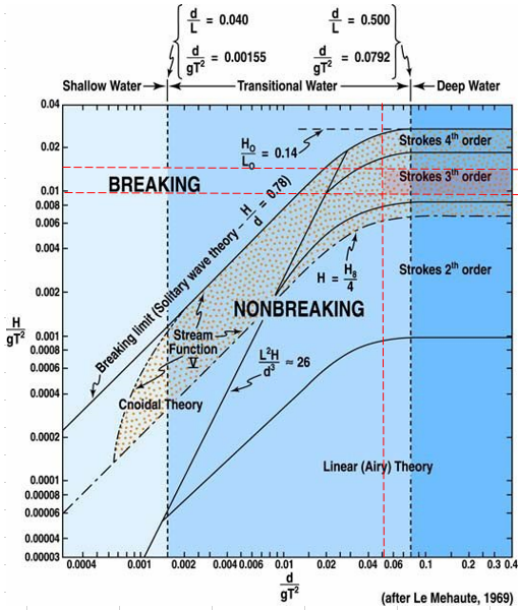

Figure C.1: Wave theories Le Mehaute [45]

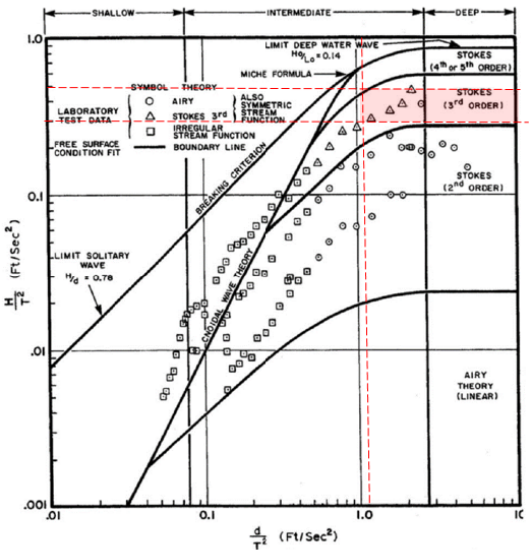

Figure C.2: Wave theories DNVGL-RP-C205 [18]

C.2. Drag coefficient

The dependence of the drag-coefficient on surface roughness for high Reynolds numbers ($Re > 0.6$) and large K_c numbers can be determined using Equation C.1 [18]. Here, $\Delta = \frac{k}{D}$ where D is the diameter of the section. k is the surface roughness which is taken as $5{\cdot}10^{-6}$, corresponding to painted steel. No marine growth will be present as only the first 24 hours are of interest.

$$C_{DS}(\Delta) = \begin{cases} 0.65; & \Delta < 10^{-4} \text{(smooth)} \\ (29 + 4 \cdot \log_{10}(\Delta))/20; & 10^{-4} < \Delta < 10^{-2} \\ 1.05; & \Delta > 10^{-2} \text{(rough)} \end{cases} \tag{C.1}$$

The drag coefficient is a function of the Keuligen-Carpenter number for super-critical Reynold numbers. this is accounted for by approximating C_D as in Equation C.2 [18].

$$C_D = C_{DS}(\Delta) \cdot \psi(K_C) \tag{C.2}$$

The wake amplification factor $\psi(K_C)$ is given by Equation C.3 [18]. This is applicable for low Keulegan-Carpenter numbers (K_C<12).

$$\psi(K_c) = \begin{cases} C_\pi + 0.10(K_C - 12); & 2 \leq K_C < 12 \\ C_\pi - 1.00; & 0.75 \leq K_C < 2 \\ C_\pi - 1.00 - 2.00(K_C - 0.75); & K_C \leq 0.75 \end{cases} \tag{C.3}$$

Where,
$C_\pi = 1.50 - 0.024 \cdot (12/C_{DS} - 10)$

For higher Keulegan-Carpenter numbers, the wake amplification can be found by interpolating between the curve for a smooth cylinder (C_{DS}=0.65) and rough cylinder (C_{DS}=1.05) as visualised in Figure C.3.

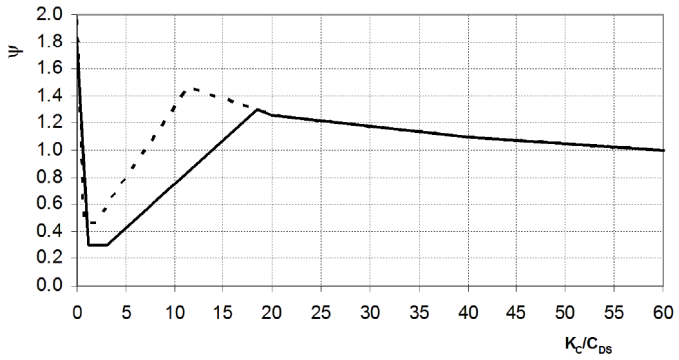

Figure C.3: Wake amplification factor ψ as a function of K_c-number for smooth (C_{DS}=0.65 - solid line) and rough (C_{DS} = 1.05 - dotted line).

C.3. Added mass coefficient

For a K_C>3, which will be the case for a jacket structure, the added mass coefficient can be calculated using Equation C.4 [18]. The value for C_{DS} is calculated in Equation C.1.

$$C_M = \max\left\{\begin{array}{c} 2.0 - 0.044(K_C - 3) \\ 1.6 - (C_{DS} - 0.65) \end{array}\right\} \tag{C.4}$$

This relation is visualised in Figure C.4 where the mass coefficient as function of Keuligen-Carpenter number is visualised.

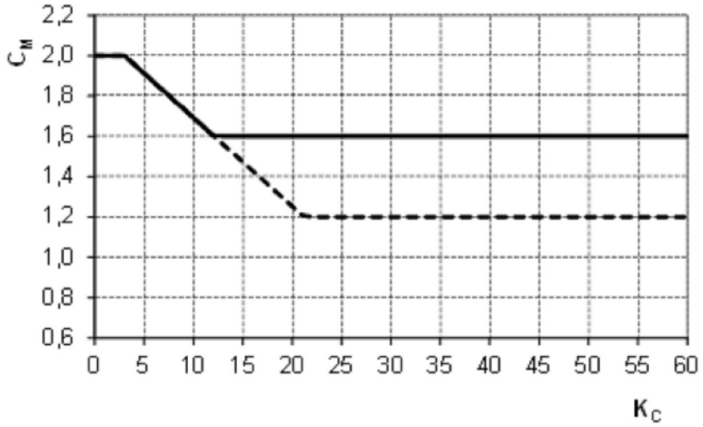

Figure C.4: Added mass coefficient C_M vs. K_C-number for a smooth (solid line) and rough (dotted line) cylinder.

D

Soil-pile interaction

D.1. P-y calculation

Analysing laterally loaded piles is most commonly done using p-y curves. When using this method, the foundation pile is modelled using beam element connected to a nonlinear spring at every node. Each nonlinear spring is characterised by a p-y curve specifying the lateral resistance per unit length (p) [N/m] for a lateral deflection y [m]. The ultimate lateral resistance during static lateral loading is denoted as p_u [N/m].

P-y curves are in general dependant on the depth below the soil surface, the diameter of the foundation pile and the soil characteristics at the specific depth. As a result, p-y curves are calculated different dependant on the type of soil layer. Different design regulations such as *API-RP-2A-WSD* [3] or *DNVGL-OS-J101* [16] recommend relatively similar relations to determine the p-y curves. For this project, relations from the *DNVGL-OS-J101* [16] since these are default at Boskalis.

The soil properties which are present at the site of interest are summarized in Table D.1. Here γ' is the submerged unit weight of soil [kN/m^3], ϕ is the internal angle of friction [Deg], s_u is the undrained shear strength [kPa], J is a dimensionless empirical constant ranging between 0.25 and 0.5 dependant on the type of clay [-] and ϵ_{50} is the strain at one-half the maximum stress in laboratory untrained compression tests [-]. The relation between these properties and the p-y curves for respectively sand and clay will be explained. All these relations are based on the *DNVGL-OS-J101* [16].

Table D.1: Soil properties at site.

Soil type	γ' [kN/m^3]	ϕ [Deg]	s_u [kPa]	J [-]	ϵ_{50} [-]
Sand	10	38.1	-	-	-
Soft clay	9	-	20	0.5	0.0201
Stiff clay	11	-	500	0.25	0.0025

Sand

The ultimate lateral resistance for a cohesionless soil, in this case sand, is calculated using Equation D.1. Coefficients C_1, C_2 and C_3 are determined using Figure D.1 using the internal angle of friction. X [m] is the depth below the soil surface and X_R [m] is the transition depth determining the relation that should be used. D [m] is the diameter of the foundation pile.

$$p_u = \begin{cases} (C_1 X + C_2 D)\gamma' X & \text{for } 0 < X \leq X_R \\ C_3 D \gamma' X & \text{for } X > X_R \end{cases} \tag{D.1}$$

The actual p-y curve is described using Equation D.2 where A is a factor to account for static or cyclic loading as described in Equation D.3. In this case, static loading is used. Furthermore, k is the initial subgrade reaction which is found using Figure D.2.

$$p = A p_u \tanh\left(\frac{kX}{A p_u} y\right) \tag{D.2}$$

$$A = \begin{cases} 0.9 & \text{for cyclic loading} \\ \left(3 - 0.8\frac{X}{D}\right) \geq 0.9 & \text{for static loading} \end{cases} \tag{D.3}$$

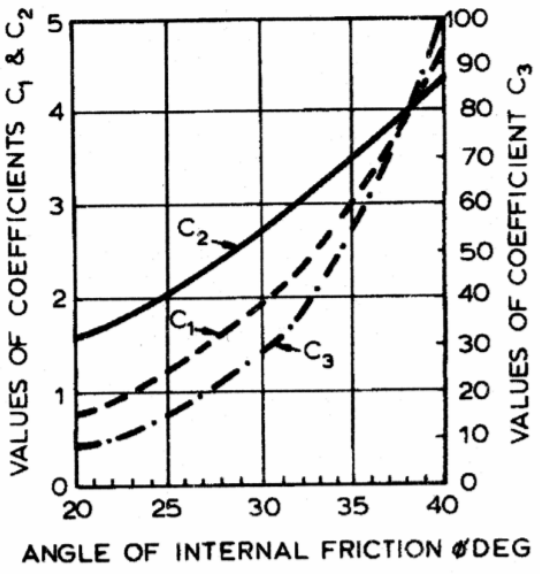

Figure D.1: Coefficients C_1, C_2 and C_3 vs. angle of friction [17]

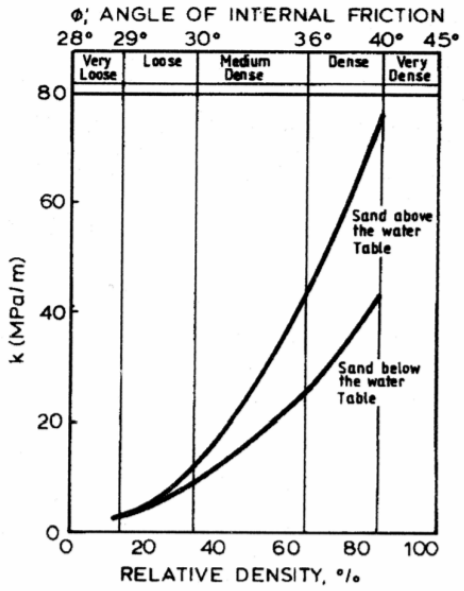

Figure D.2: Modulus of subgrade reaction k vs. fricton angle ϕ.

Clay

The ultimate lateral resistance for a cohesive soil, in this case the soft and stiff clay, can be determined using Equation D.4. X [m] is the depth below the soil surface and X_R [m] is the transition depth determining the relation that should be used. D is the diameter of the foundation pile [m].

$$p_u = \begin{cases} \left(3 s_u + \gamma' X\right) D + J s_u X & \text{for } 0 < X \leq X_R \\ 9 s_u D & \text{for } X > X_R \end{cases} \tag{D.4}$$

For static loading, Equation D.5 can be used to determine the p-y curve. Here, $y_c = 2.5\epsilon_{50} D$.

$$p = \begin{cases} \frac{p_u}{2}\left(\frac{y}{y_c}\right)^{1/3} & \text{for } y \leq 8 y_c \\ p_u & \text{for } y > 8 y_c \end{cases} \tag{D.5}$$

P-y curves

Using the parameters from Table D.1, the p-y curves at every meter are determined. The soil distribution per meter is displayed in Figure 2.11. These curves are then added as nonlinear spring stiffness to a pile model. Figure D.3 shows this model when subjected to a force. The colour scale indicate the nonlinear spring force. One can clearly distinguish the different soil layers with their different stiffness.

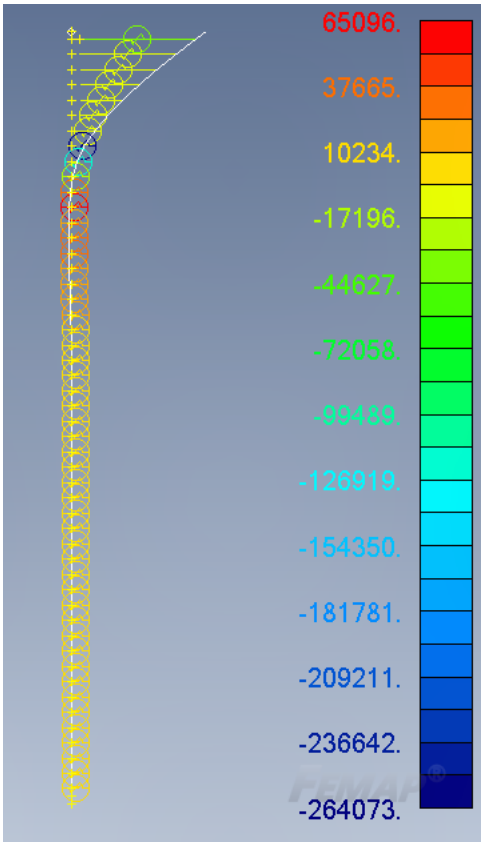

Figure D.3: P-y curves on beam elements.

E

Pile-leg dimensions

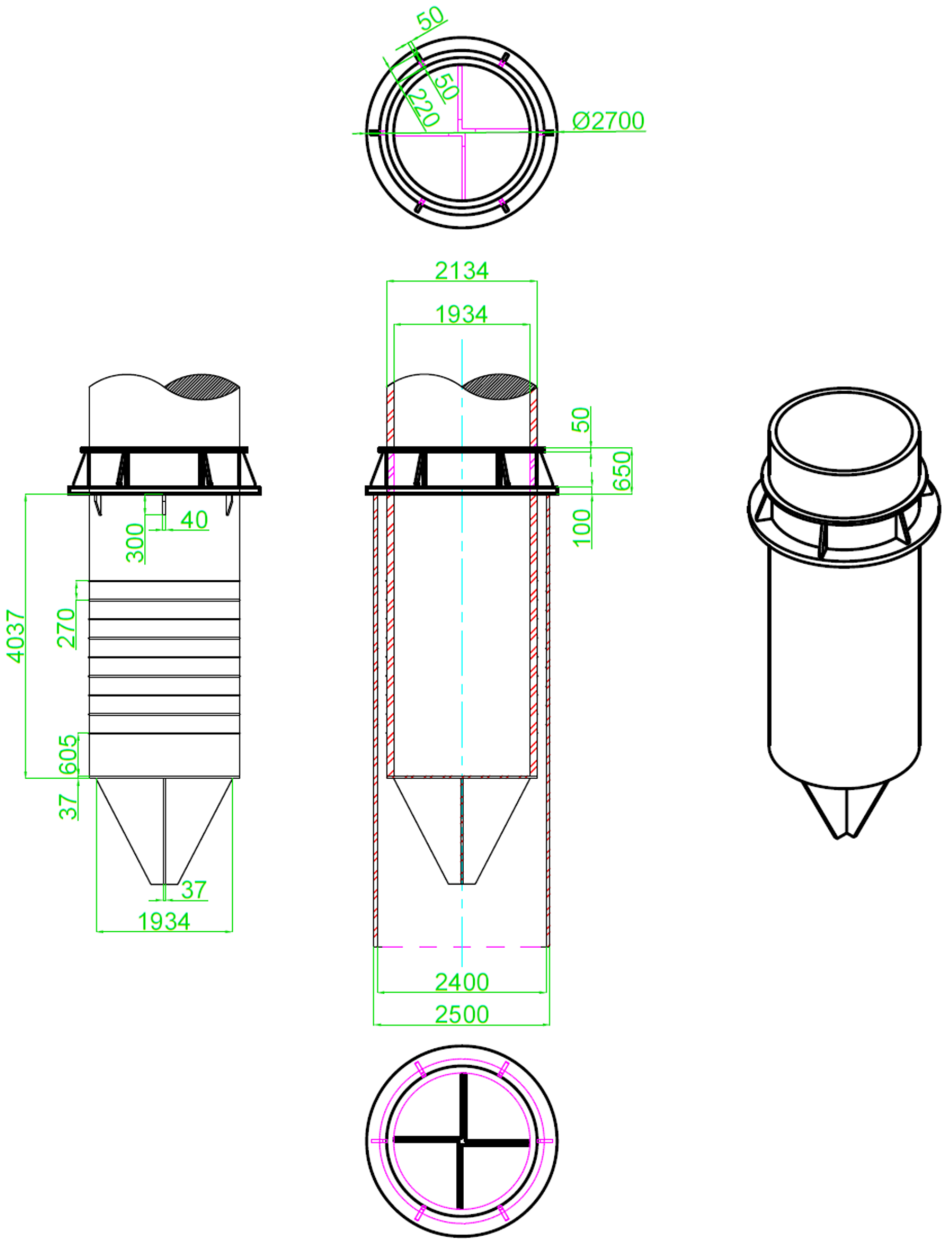

Figure E.1: Detailed drawing reference stopper

F

Contact analysis

F.1. NX Nastran contact algorithm

The NX Nastran SOL 101 - linear static module allows for "linear" contact modeling. This is in reality based on the full nonlinear contact algorithm from SOL 400. However, the material is assumed to behave linear with small strain, small displacement and small rotation. Since these are the regimes of interest for the simulations in this research, the contact algorithm from SOL 101 is sufficient.

The basic equations that are solve in this contact algorithm are equilibrium equations with boundary conditions and contact constrains. Kinematic equations describe the motions of the surfaces, needed for the contact constrains. These equations are then converted into FE matrix equations that are solved. This following information is based on the NX Nastran User Guide [66].

Kinematic equations

When setting up a friction connection in Femap, a source and target region should be assigned. As visualised in Figure F.1, surface B is the source region while surface A is the target region. At the reduced integration points (D) on the source region, the software creates a set of Cartesian basis vectors **e1,e1,e3**. While the unit vector of **e1** and **e2** are tangent to the source region, the unit vector of **e3** is normal to the source region. This unit vector will be denoted as **n**. When assuming the motion of a point along unit vector **n**, the impact point at the target region is point C. The penetration (p) of the reduced integration point (D) into the impact point at the target region can be described by Equation F.1. Here, p_0 is the initial penetration, defined by the geometry and manually adjustable. u_H is the motion of the reduced integration point at the source region and u_T the motion of the corresponding point at the target region. As described in section 3.2, the refinement of the mesh in the source region determines the amount of contact elements formed between the source and target region.

$$p = p_0 + (u_H - u_t) \cdot n \tag{F.1}$$

The contact algorithm uses a Coulomb friction force. Therefore, the relative tangential displacement increment should be computed as displayed in Equation F.5.

$$\Delta u_t = (\Delta u_H - \Delta u_T) - [n \cdot (\Delta u_H - \Delta u_T)] \cdot n \tag{F.2}$$

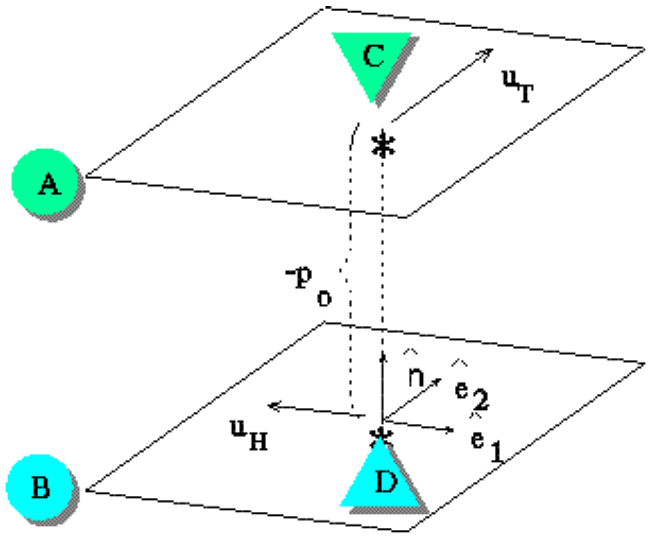

Figure F.1: Surface kinematics contact algorithm [66]

Normal contact constrains

The contact constrains between the source and target region are displayed in Equation F.3. Here p is the penetration of the source region into the target region. t_n is the normal contact pressure.

$$\begin{aligned} &p \leq 0 \\ &t_n = -n \cdot t \geq 0 \\ &t_n p = 0 \end{aligned} \tag{F.3}$$

From the constraints in Equation F.3, one can conclude that the penetration (p) cannot be greater than zero. Therefore, surfaces cannot penetrate each other. Furthermore, the normal contact pressure (t_n) cannot be smaller than 0. The last constraint states that $p = 0$ if $t_n \geq 0$ and $t_n = 0$ if $p \leq 0$. Therefore, the penetration must be 0 if there is normal contact pressure and the normal contact pressure must be zero is there is no penetration.

Coulomb friction constraints

Additional constraints are required between the surfaces which are displayed in Equation F.4. Here, ϕ describes whether two contact surfaces will "stick" or "slip". Whenever the tangential traction (t_t) is smaller than the friction (μ) times the contact pressure (t_n), resulting in $\phi < 0$, the surfaces will stick. If $\phi = 0$, the tangential traction equals the frictional resistance resulting in sliding of the surfaces.

$$\phi = |t_t| - \mu t_n \leq 0 \tag{F.4}$$

The second equation (Equation F.5) describes that the relative tangential displacement (Δu_t) will occur in the direction of the tangential traction ($\frac{t_t}{|t_t|}$). This is valid since the magnitude of the relative slip increment ($\Delta\xi$) must be a non negative value.

$$\Delta u_t = \Delta\xi \frac{t_t}{|t_t|} \tag{F.5}$$

Solution strategy

Within the Femap, the contact constraints are assigned to the selected points on the contact surfaces. In NX Nastran, contact elements are created defined by the kinematic equations, coefficient of friction and a pre-defined offset between surfaces.

Several contact algorithms can be used in order to establish a relationship between the target and contact area. Commonly used algorithm's are:

- Penalty method
- Augmented Lagrangian
- Lagrange multiplier on contact normal and penalty on tangent
- Pure Lagrange multiplier on contact normal and tangent
- Internal multipoint constraint

NX Nastran uses two methods, based on the augmented Lagrangian procedure. The augmented Lagrangian method is a combination of the penalty method and the pure Lagrange method. It tends to behave better compared to the penalty method and normal Lagrange method. According to [67], the augmented Lagrangian method results in a decrease in ill-conditioning of governing equations. It therefore decreases computational time. Furthermore, it is less sensitive to the contact stiffness coefficient which is a drawback from the penalty method [74]. However, augmented Lagrangian method in general requires more computational time.

F.2. Behaviour linear contact algorithm

In order to investigate the behaviour of the contact algorithm, a basic model consisting of a flange and plate is tested in Femap. This model, as visualised in Figure F.2, can be used to assess sensitivity of the friction connection. It consists of a bottom plate, modelled with CHEXA elements and a top flange modelled with CTETRA and CPYRAM elements. A contact region is assigned between the two contact surfaces and a varying friction coefficients will be used. A rigid spider elements is used to create a node from where a normal force of 1000 N and a varying force in y-direction will be applied. This will be done using a friction coefficient of respectively 0.2 [-],0.3 [-] and 0.4 [-].

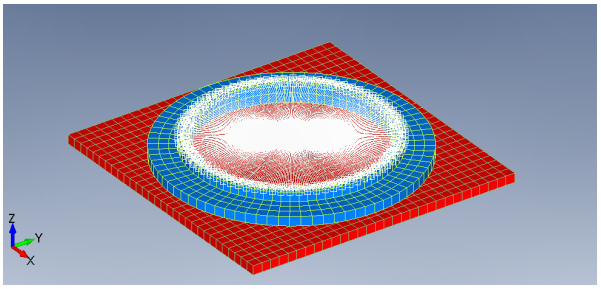

Figure F.2: Contact algorithm test model.

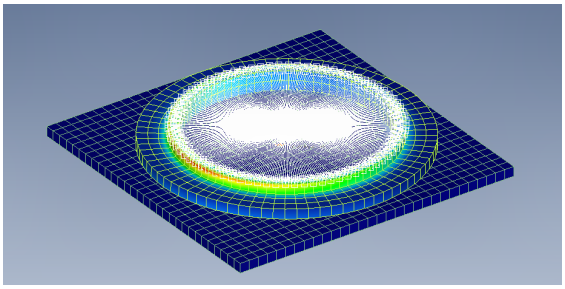

Figure F.3: Contact algorithm test model Von Mises stress.

Using a basic Coulomb friction law, as shown in Equation F.6, results in test parameters as visualised in Table F.1. In order to check the test model, a force range (Fy) from 170 N to 410 N with steps of 1 N is used.

$$F_t = \mu F_n \tag{F.6}$$

Table F.1: Coulomb friction test parameters

μ	F_n	F_t
0.2	1000	200
0.3	1000	300
0.4	1000	400

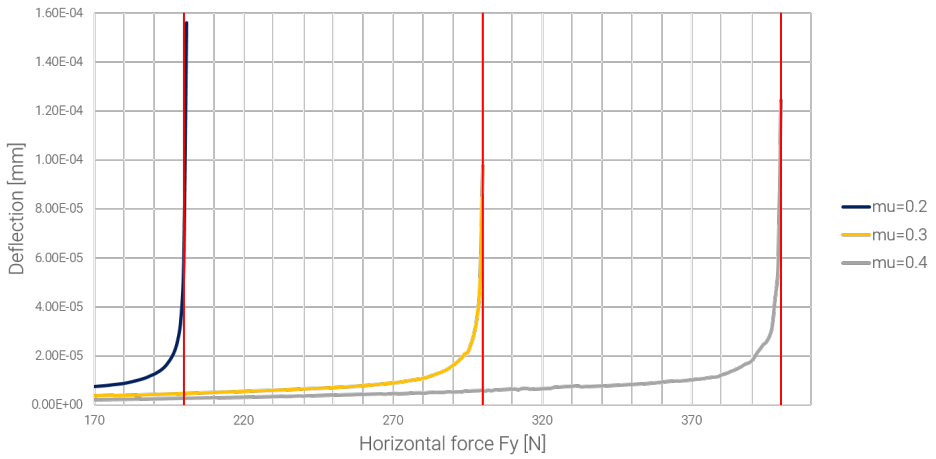

Figure F.4: Friction test results for flange model.

Figure F.4 shows the motion of the flange as measured from the spider node. The red lines denote the tangential forces as calculated using Equation F.6. As can be seen, the displacements before sliding are almost zero. Just before sliding occurs, the displacements increase. Whenever the flange starts sliding, the contact algorithm fails to converge. As discussed in section F.1, the solution is valid for small displacements and rotations. The test model behaves very well and gives accurate results when compared to the ideal solutions from Figure F.2.

The stress distribution during sliding can best be visualised when modelling two blocks with the same force distribution as the flange-plate model. As can be observed in Figure F.5, the stress distribution between the two blocks is smooth. When sliding appears, limited stress can be passed on through the top block.

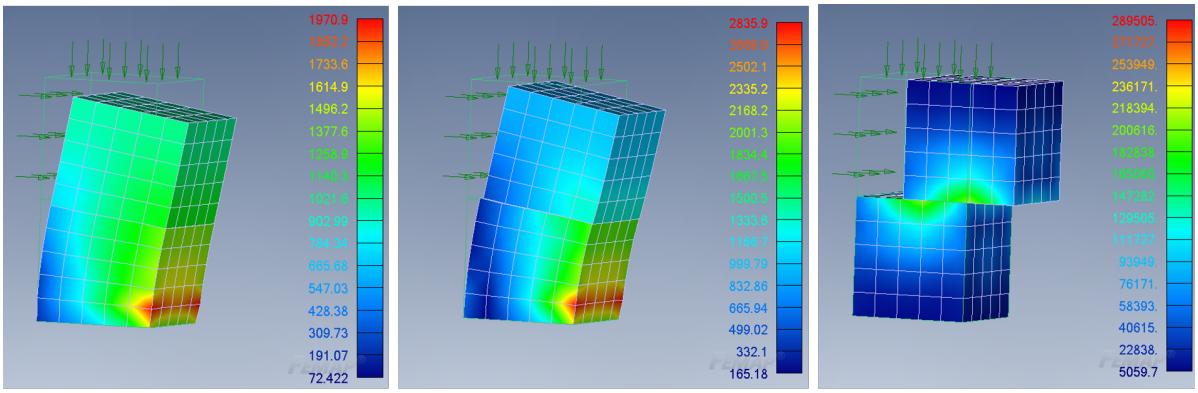

Figure F.5: Stress distribution two blocks during sliding.

G

Modified stopper models

Table G.1: Modified stopper area per configuration.

Configuration	Model	Angle bracket [^{o}]	Contact area [m^2]	% of reference
1	Reference	40	0.073	22%
1	Sensitivity 1	50	0.091	28%
1	Sensitivity 2	70	0.127	39%
1	Sensitivity 3	90	0.164	50%
1	Sensitivity 4	110	0.200	61%
2	Reference	26.7	0.073	22%
2	Sensitivity 1	33.3	0.091	28%
2	Sensitivity 2	46.7	0.127	39%
2	Sensitivity 3	60	0.164	50%
2	Sensitivity 4	73.3	0.200	61%
3	Reference	20	0.073	22%
3	Sensitivity 1	25	0.091	28%
3	Sensitivity 2	35	0.127	39%
3	Sensitivity 3	45	0.164	50%
3	Sensitivity 4	55	0.200	61%

G.1. Configuration 1

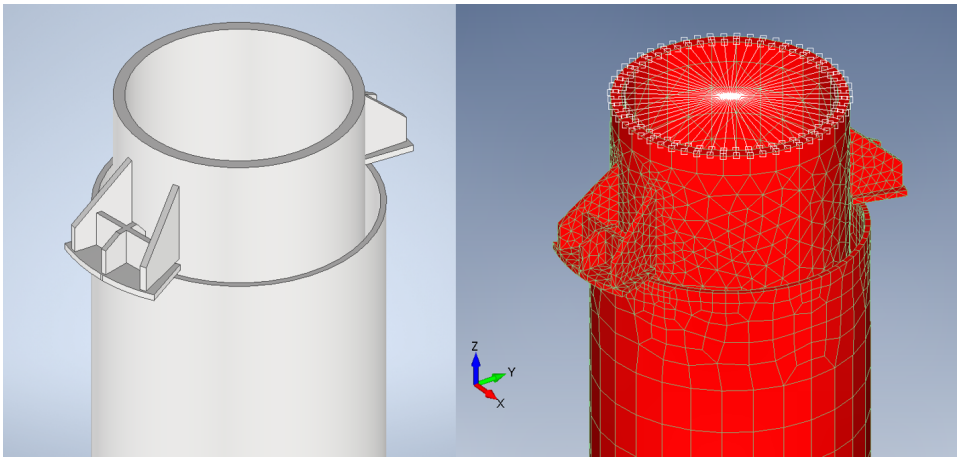

Figure G.1: Configuration 1 reference 3D and Femap model.

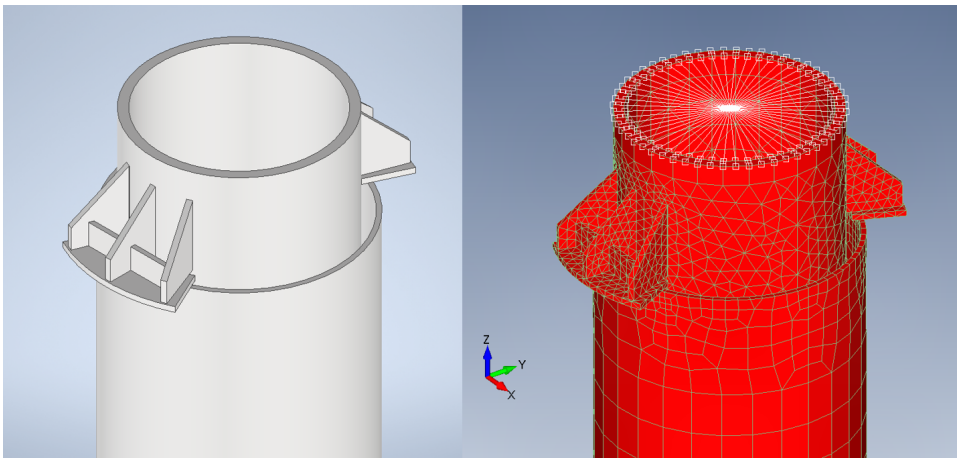

Figure G.2: Configuration 1 sensitivity 1 3D and Femap model.

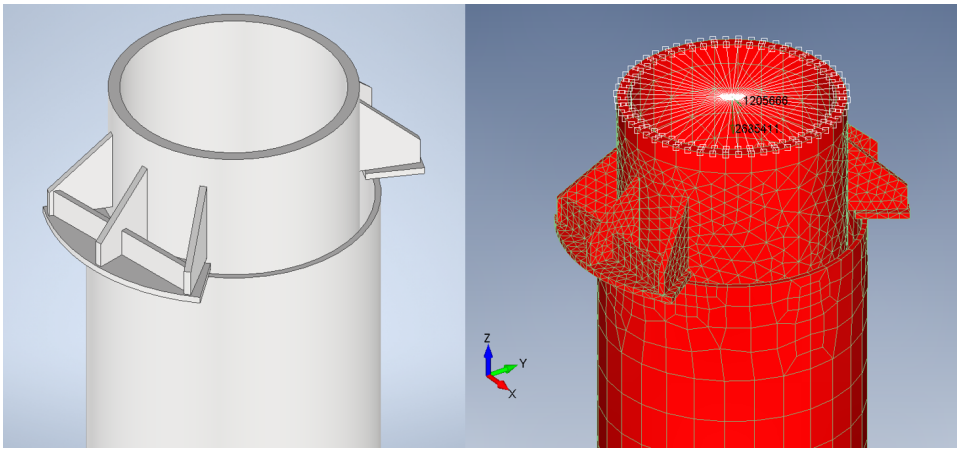

Figure G.3: Configuration 1 sensitivity 2 3D and Femap model.

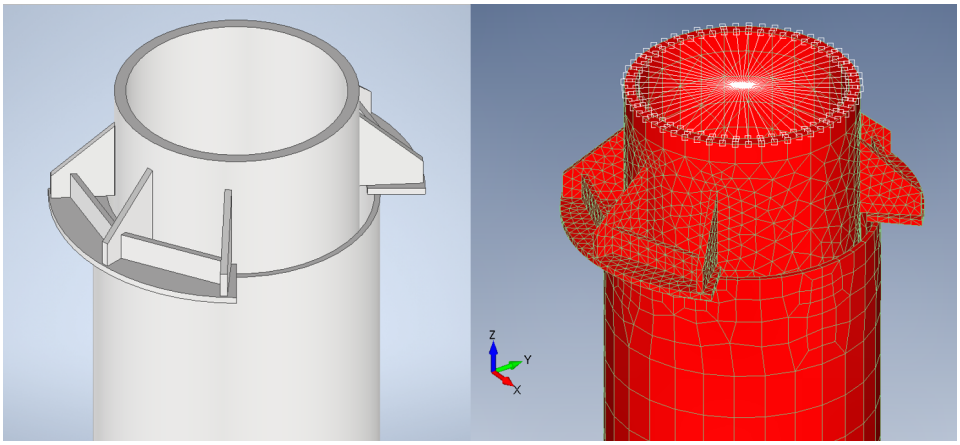

Figure G.4: Configuration 1 sensitivity 3 3D and Femap model.

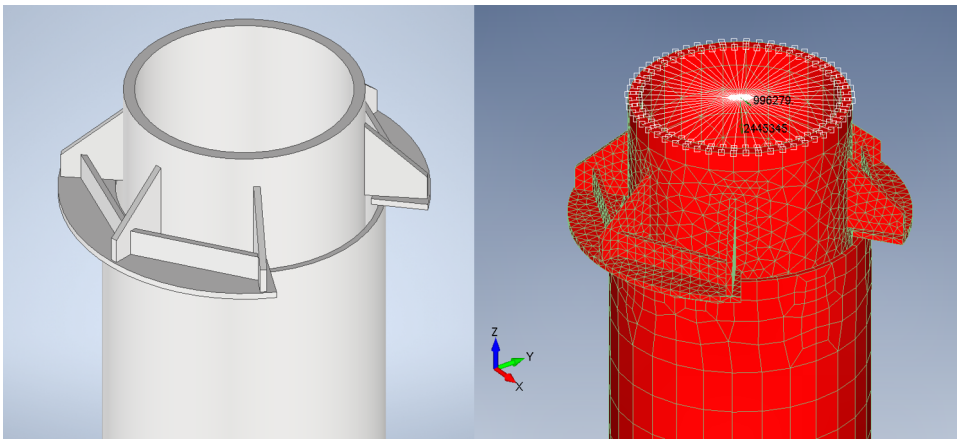

Figure G.5: Configuration 1 sensitivity 4 3D and Femap model.

G.2. Configuration 2

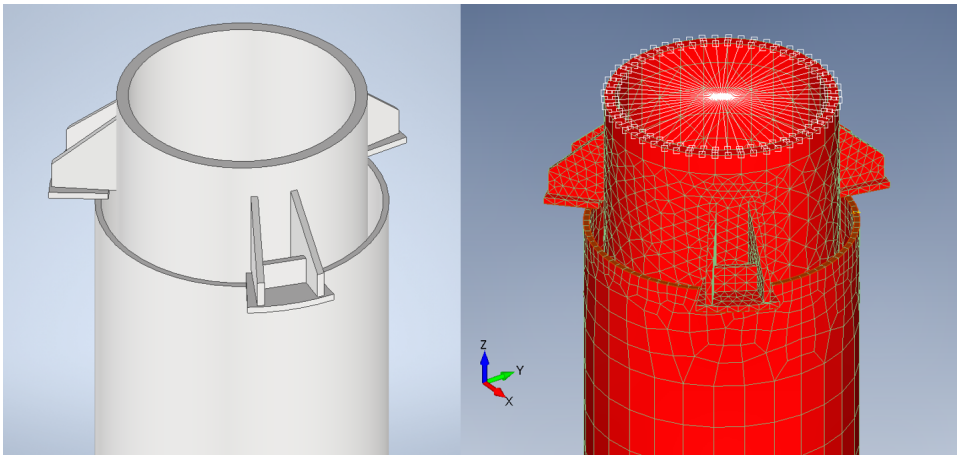

Figure G.6: Configuration 2 reference 3D and Femap model.

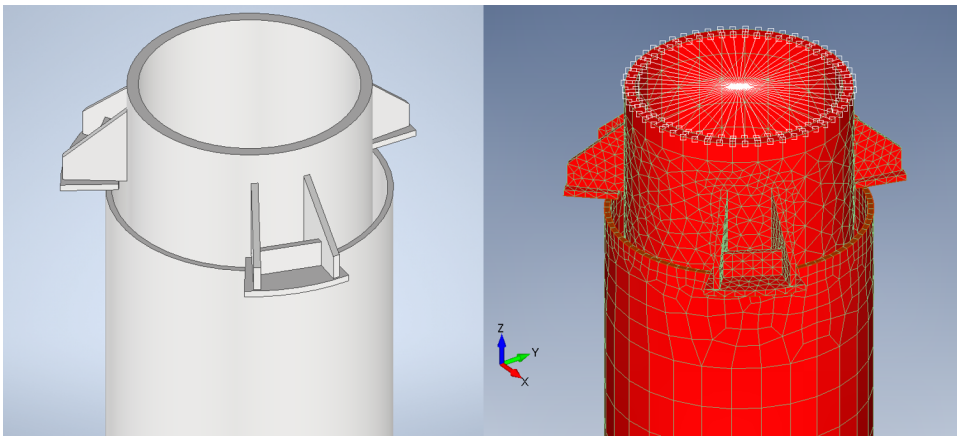

Figure G.7: Configuration 2 sensitivity 1 3D and Femap model.

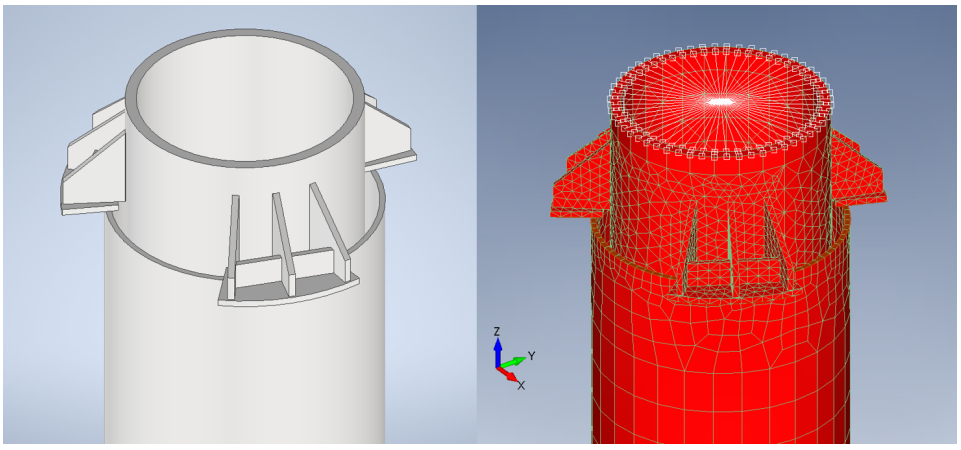

Figure G.8: Configuration 2 sensitivity 2 3D and Femap model.

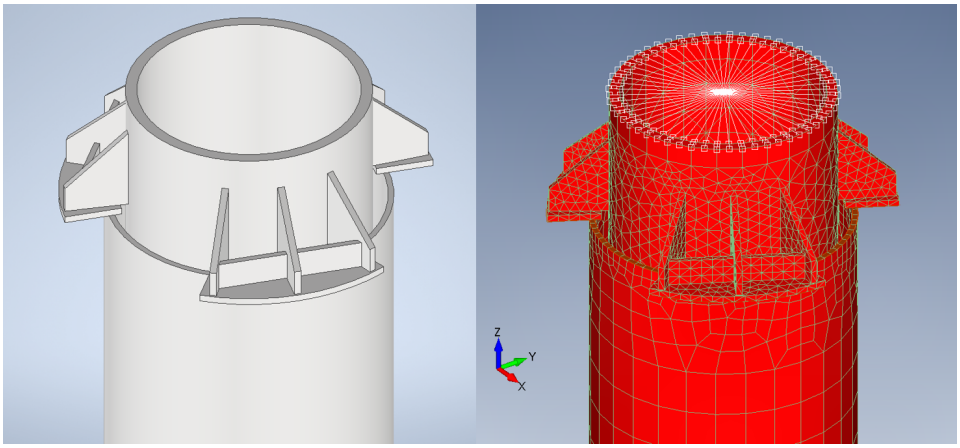

Figure G.9: Configuration 2 sensitivity 3 3D and Femap model.

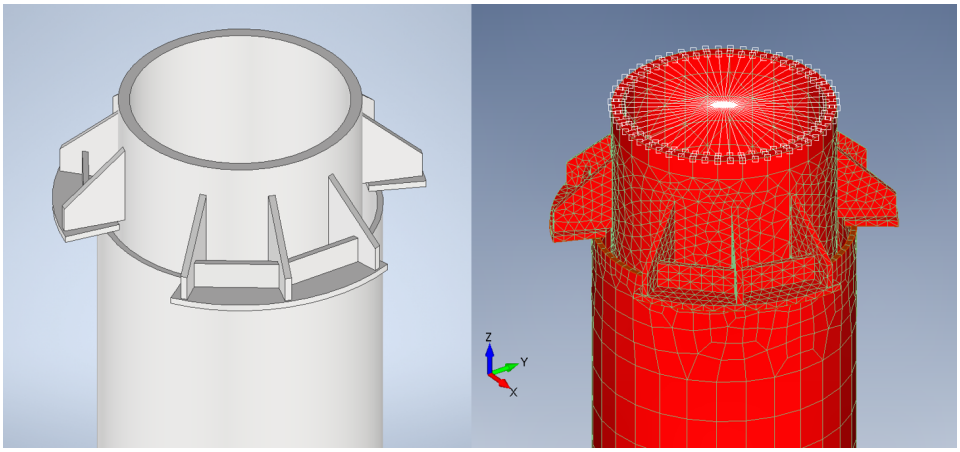

Figure G.10: Configuration 2 sensitivity 4 3D and Femap model.

G.3. Configuration 3

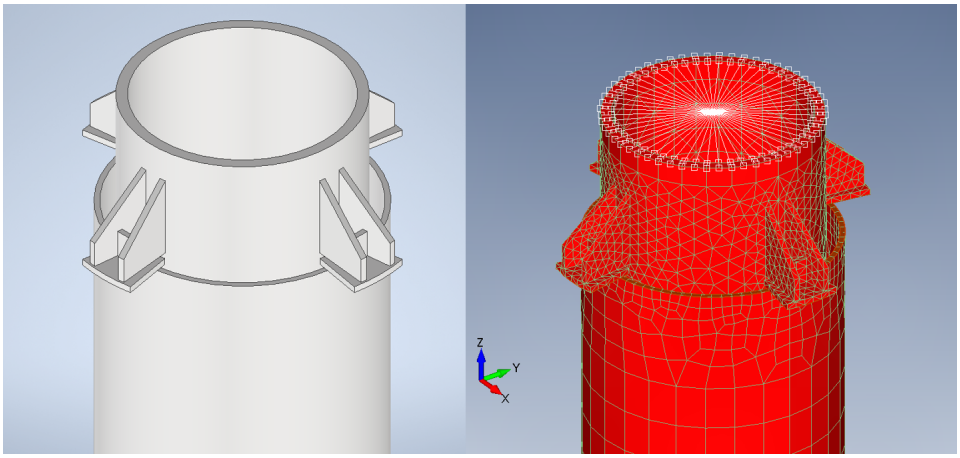

Figure G.11: Configuration 2 reference 3D and Femap model.

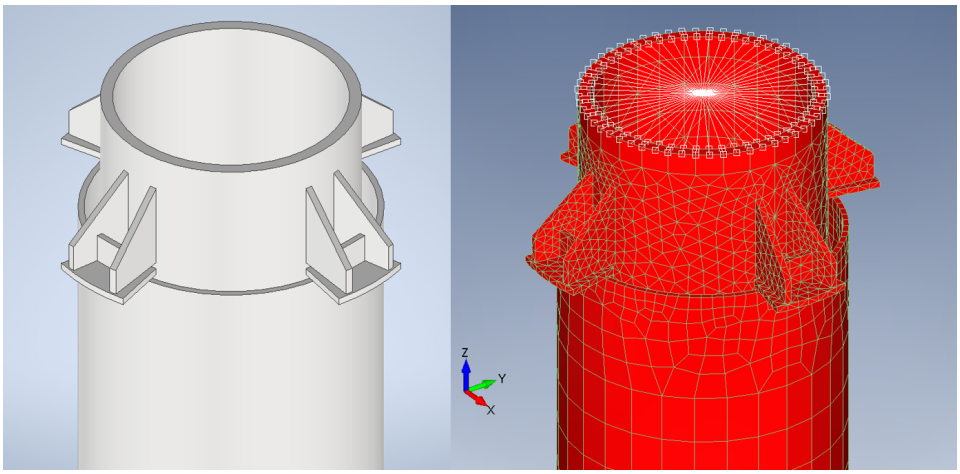

Figure G.12: Configuration 2 sensitivity 1 3D and Femap model.

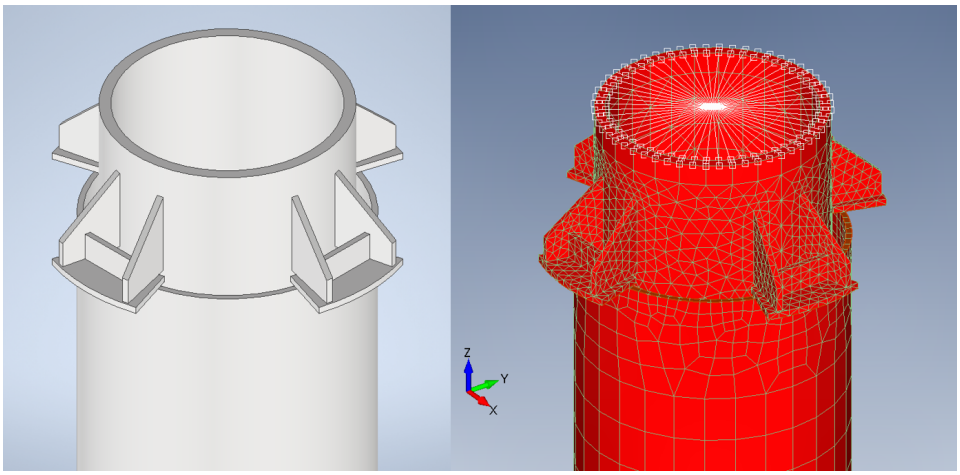

Figure G.13: Configuration 2 sensitivity 2 3D and Femap model.

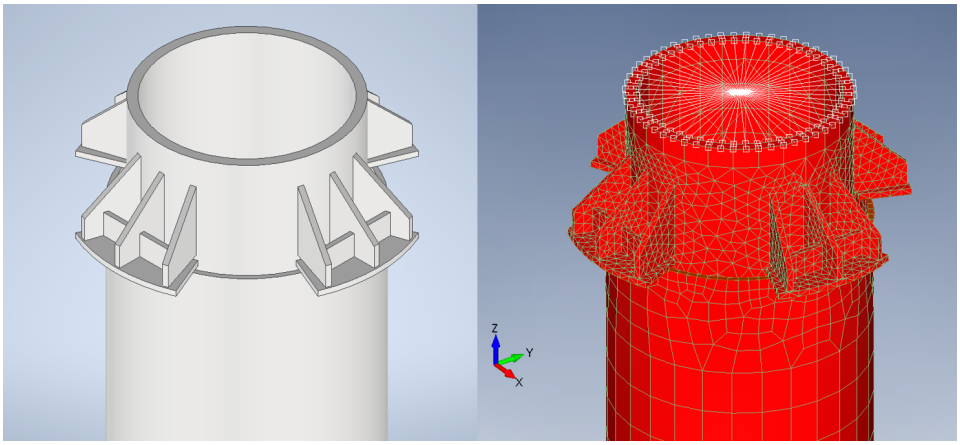

Figure G.14: Configuration 2 sensitivity 3 3D and Femap model.

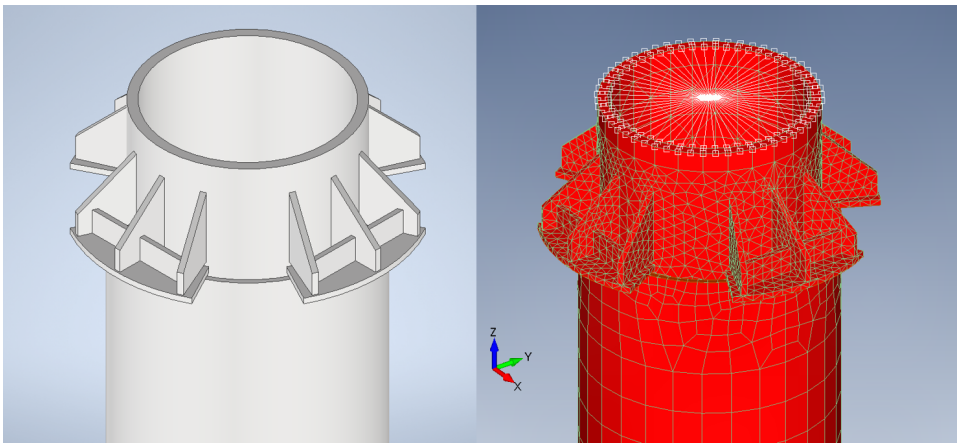

Figure G.15: Configuration 2 sensitivity 4 3D and Femap model.

Bibliography

[1] Boskalis internal document. Technical report, Hamburg (2019).

[2] Amdahl, J., Ehlers, S., and Leira Bernt, J. (2013), *Collision and Grounding of Ships and Offshore Structures - 1st Edition*. CRC Press.

[3] American Petroleum Institute. API-RP-2A-WSD Recommended Practice for Planning, Designing and Constructing Fixed Offshore Platforms Working - Working Stress Design. Technical report (2002).

[4] Benzley, S. E., Perry, E., Merkley, K., Clark, B., and Sjaardema, G. (1995). A Comparison of All-Hexahedral and All-Tetrahedral Finite Element Meshes for Elastic and Elasto-Plastic Analysis. *4th International Meshing Roundtable, Sandia National Laboratories*, (January):179–191.

[5] Bhattacharya, S. (2017). Soil-Structure Interactions for Offshore Wind Turbines. *The institution of Engineering and Technology*.

[6] Billington, C. J. (1980). Research into composite tubular construction for offshore jacket structures. *Topics in Catalysis*, 1(1):18–26.

[7] Billington, C. J. and Lewis, G. H. The strength of large diameter grouted connections. In *Proceedings of the Annual Offshore Technology Conference*, pages 291–297. Offshore Technology Conference (1978).

[8] Boskalis Offshore. Design Brief - Hydrodynamics. Technical report, Papendrecht (2020).

[9] Bush, E. and Manuel, L. Foundation Models for Offshore Wind Turbines. In *47th AIAA Aerospace Sciences Meeting Including The New Horizons Forum and Aerospace Exposition*, Orlande, Florida (2009).

[10] Carette, G. and Malhotra, V. (5 1983). Early-Age Strength Development of Concrete Incorporating Fly Ash and Condensed Silica Fume. *Special Publication*, 79:765–784.

[11] Cecconello, V. and Tutikian, B. (2 2012). The influence of low temperature on the evolution of concrete strength. *Revista IBRACON de Estruturas e Materiais*, 5(1):68–83.

[12] Chandrasekaran, S. Dynamic Analysis and Design of Offshore Structures. volume 5, pages 50–51. Springer India (2015).

[13] Dallyn, P., El-Hamalawi, A., Palmeri, A., and Knight, R. (8 2015). Experimental testing of grouted connections for offshore substructures: A critical review. *Structures*, 3:90–108.

[14] Damiani, R., Dykes, K., and Scott, G. A Comparison Study of Offshore Wind Support Structures with Monopiles and Jackets for U.S. Waters. Technical report, National Renewable Energy Laboratory, Munich, Germany (2016).

[15] Deutscher Wetterdienst. Sea Surface Temperature (2020). URL `www.dwd.de`.

[16] DNVGL (2014). DNVGL-OS-J101 Design of Offshore Wind Turbine Structures. (November): 1–142.

[17] DNVGL. DNVGL-ST-0126 Support structures for wind turbines. Technical report (2018).

[18] DNVGL. DNVGL-RP-C205 Environmental conditions and environmental loads. Technical report (2019).

[19] DNVGL. DNVGL-ST-N001 Marine operations and marine warranty. Technical Report January (2020).

[20] EnDuraSim. Contact Modelling in Femap with NX Nastran. Technical report (2018).

[21] Flotre, A. Year of the jacket (2020). URL `https://www.rystadenergy.com/newsevents/news/press-releases`.

[22] Fréne, J. and Cicone, T. Friction in Lubricated Contacts. In *Handbook of Materials Behavior Models*, pages 760–767. Elsevier (2001).

[23] Gonnerman, H. and Shuman, E. Flexure and Tension Tests of Plain Concrete. Technical report, Portland Cement Association (1928).

[24] Harold, A., Pablo, R., and Michael, T. Renewable power generation costs in 2018. Technical report, International Renewable Energy Agency (IRENA), Abu Dhabi (2019).

[25] Hasselmann, K., Barnett, T., Bouws, E., Carlson, H., Cartwright, D., Enke, K., Ewing, J., Gienapp, H., Hasselmann, D., and Kruseman, P. Measurements of wind-wave growth and swell decay during the Joint North Sea Wave Project (JONSWAP). Technical report, Deutches Hydrographisches Institut (1973).

[26] Health and Safety Executive. Environmental considerations. Technical report, Offshore Technology Report 2001/010 (2001).

[27] Hewlett, P. and Liska, M. (2019). Lea's Chemistry of Cement and Concrete. *Lea's Chemistry of Cement and Concrete*.

[28] Igwemezie, V., Mehmanparast, A., and Kolios, A. (9 2018). Materials selection for XL wind turbine support structures: A corrosion-fatigue perspective. *Marine Structures*, 61:381–397.

[29] IHC (2017). Seaway heavy lifting and IHC IQIP cooperate on Beatrice offshore wind farm. URL `https://www.ihciqip.com/en/news/`.

[30] IHC (1 2020). IHC IQIP to deliver 84 Jacket Pile Grippers. URL `https://www.ihciqip.com/en/news/`.

[31] Inch Cape Wind. Inch Cape Wind Farm - Non-technical summary. Technical report (2018). URL `www.inchcapewind.com`.

[32] International Energy Agency. Offshore Wind Outlook 2019: World Energy Outlook Special Report. Technical report, International Energy Agency (2019).

[33] ISO. ISO - 19902 Petroleum and natural gas industries - Fixed steel offshore structures. Technical report (2007).

[34] Iuga, D. Wind energy- the facts (2020). URL `https://www.wind-energy-the-facts.org/`.

[35] Ivkovic, B. (2000). The Influence of the Contact Surface Roughness on the Static Friction Coefficient. *Tribology in industry*, Volume22(3&4).

[36] Jensen, A. Linear Contact Analysis: Demystified. Technical report, FEA predective Engineering, Portland (2010).

[37] Jia, J. (2014). Essentials of Applied Dynamic Analysis. *Transportation Research Board*, (1215): 259.

[38] Johansen, A., Solland, G., Lervik, A., Strande, M., and Nybø, T. (2018). Testing of jacket pile sleeve grouted connections exposed to variable axial loads. *Marine Structures*, 58(November 2016):254–277.

[39] Jonkman, J., Butterfield, S., Passon, P., Larsen, T., Camp, T., Nichols, J., Azcona, J., and Martinez, A. Offshore Code Comparison Collaboration within IEA Wind Annex XXIII: Phase II Results Regarding Monopile Foundation Modeling. In *IEA European Offshore Wind Conference*, Berlin, Germany (2007).

[40] Kaimal, J. C. and Finnigan, J. J. J. J. (1994), *Atmospheric boundary layer flows : their structure and measurement*. Oxford University Press.

[41] Kheder, G. F. (7 1999). Two stage procedure for assessment of in situ concrete strength using combined non-destructive testing. *Materials and Structures/Materiaux et Constructions*, 32 (220):410–417.

[42] Knupp P M. Achieving finite element mesh quality via optimization of the jacobian matrix norm and associated quantities. Technical report, Parallel computing sciences department, Albuquerque (1999).

[43] Kosmatka, S., Kerkhoff, B., and Panarese, W. (2008), *Design and Control Design Concrete Mixtures*.

[44] Kristiansen, T. and Faltinsen, O. M. (2012). Modelling of current loads on aquaculture net cages. *Journal of Fluids and Structures*.

[45] Le Mehaute, B. (1976), *An introduction to hydrodynamics and water waves*. Springer, Berlin, Heidelberg.

[46] Lim, M. and Ha, S. (2017). Ultra-High-Strength Grout for Filling Steel Pipes in Offshore Wind Turbines. *International Journal of Applied Engineering Research*, 12(23):13064–13076.

[47] Lohaus, L., Cotardo, D., and Werner, M. (2014). A test system to simulate the influence of early age cycling on the properties of grout material. *Proceedings of the International Offshore and Polar Engineering Conference*, 3:234–239.

[48] Lohaus, L., Cotardo, D., Werner, M., Schaumann, P., and Kelma, S. (2015). Experimental and Numerical Investigations of Grouted Joints in Monopiles Subjected to Early-Age Cycling. 2(4): 193–201.

[49] Lohaus, L., Schaumann, P., Cotardo, D., Kelma, S., and Werner, M. Experimental and Numerical Investigations on Grouted Joints in Monopiles Subjected to Early-age Cycling to Evaluate the Influence of Different Wave Loadings. In *International Ocean and Polar Engineering Conference* (2015). ISBN 9781880653890. URL `www.isope.org`.

[50] Lotsberg, I. Fatigue Design of Marine Structures. In *Camebridge University Press*, pages 435–437 (2016).

[51] Lotsberg, I. and Solland, G. Assessment of capacity of grouted connections in piled jacket structures. In *Proceedings of the International Conference on Offshore Mechanics and Arctic Engineering - OMAE*, volume 2 B (2013).

[52] Lotsberg, I., Serednicki, A., Cramer, E., Bertnes, H., and Haahr, P. E. On the structural capacity of grouted connections in offshore structures. In *Proceedings of the International Conference on Offshore Mechanics and Arctic Engineering - OMAE*, volume 3, pages 667–677 (2011).

[53] Lotsberg, I., Serednicki, A., Oerlemans, R., and Lervik, A. (2013). Capacity of cylindrical shaped grouted connections with shear keys in offshore structures reported from a joint industry project. *Journal of Structural Engineering*, 91:42–28.

[54] Lyons, W. C. (2016). Drilling and Well Completions. *Standard Handbook of Petroleum and Natural Gas Engineering*, pages 1–584.

[55] Moan, T. (2003), *Finite element modelling and analysis of marine structures*, volume UK-03-98.

[56] Morison, J., Johnson, J., and Schaaf, S. (5 1950). The Force Exerted by Surface Waves on Piles. *Journal of Petroleum Technology*, 2(05):149–154.

[57] Nehdi, M. and Soliman, A. M. (4 2011). Early-age properties of concrete: Overview of fundamental concepts and state-of-the-art research. *Proceedings of Institution of Civil Engineers: Construction Materials*, 164(2):57–77.

[58] Paik, J. K. and Thayamballi, A. K. (1 2007), *Ship-shaped offshore installations: Design, building, and operation*. Cambridge University Press.

[59] Passon, P. Memorandum Derivation and Description of the Soil-Pile-Interaction Models. In *IEA-Annex XXIII Subtask 2*, Stuttgart, Germany (2006).

[60] Pessiki, S. and Carino, N. (1988). SettingTime and Strength of Concrete Using the Impact-Echo Method. *ACI Materials Journal*, 85(5).

[61] Pijpers R.J.M. and Slot H.M. Friction coefficients for steel to steel contact surfaces in air and seawater. Technical report, TNO, Delft (2020).

[62] Poudineh, R., Brown, C., and Foley, B. (2018). Global offshore wind market report 2018. *Economics of Offshore Wind Power*, pages 15–31.

[63] Powers, T. C. (1948). A discussion of cement hydration in relation to the curing of concrete. *Highway Research Board Proceedings*, 27.

[64] Siemens Industry Software. Element Library Reference . Technical report, Plano, USA (2014).

[65] Siemens Industry Software. NX Nastran User's Guide Contents. Technical report, Plano, USA (2016).

[66] Siemens Industry Software. NX Nastran User Guide. Technical report, Piano (USA) (2016).

[67] Simo, J. C. and Laursen, T. A. (1992). An augmented lagrangian treatment of contact problems involving friction. *Computers and Structures*, 42(1):97–116. ISSN 00457949.

[68] Soares, C. G. Developments in the Collision and Grounding of Ships and Offshore Structures. In *Conference on Collision and Grounding of Ships and Offshore Structures (ICCGS 2019)*, pages 214–215, Lisbon (2019). CRC Press.

[69] Sündermann, J. (2003). The changing North Sea: knowledge, speculation and new challenges. *Oceanologia*, 45:247-259.

[70] Sündermann, J. and Pohlmann, T. (9 2011). A brief analysis of North Sea physics. *Oceanologia*, 53(3):663–689.

[71] UNFCC. Paris Agreement. Technical report, Paris (2015).

[72] US Energy Information Administration. International Energy Outlook 2019. Technical report, Washington (USA) (2019).

[73] Varma, K. (2014). Finite Amplitude Ocean Waves - Waves with Peaked Crests and Broad Troughs. *Resonance*, 19:1047 – 1057.

[74] Wang, E. ANSYS contact. Technical report (2004).

[75] Wang, M., Zhao, Y., Du, W., He, Y., and Jiang, R. Derivation and Validation of Soil-Pile-Interaction Models for Offshore Wind Turbines. In *The Twenty-third International Offshore and Polar Engineering Conference*, Anchorage, Alaska (6 2013). International Society of Offshore and Polar Engineers.

[76] Wood, S. (1992). Evaluation of the Long-Term Properties of Concrete. *ACI Materials Journal*, 88(6).

[77] Woodward Joe. Mid-side nodes – PADT, Inc. (2 2011). URL `https://www.padtinc.com/`.

[78] Yoon, H., Kim, Y., Kim, H. S., Kang, J. W., and Koh, H. M. (8 2017). Evaluation of early-age concrete compressive strength with ultrasonic sensors. *Sensors (Switzerland)*, 17(8). ISSN 14248220. doi: 10.3390/s17081817.